Magnetic resonance of ferrimagnetic insulators

Hannes Maier-Flaig

Bayerische Akademie der Wissenschaften

Walther Meißner Institut

TECHNISCHE UNIVERSITÄT MÜNCHEN

Lehrstuhl E23 für Technische Physik

Walther-Meißner-Institut für Tieftemperaturforschung
der Bayerischen Akademie der Wissenschaften

Magnetic resonance of ferrimagnetic insulators

Hannes Benjamin Maier-Flaig

Vollständiger Abdruck der von der Fakultät für Physik der Technischen Universität München zur Erlangung des akademischen Grades eines

Doktors der Naturwissenschaften

genehmigten Dissertation.

Vorsitzender:		Prof. Dr. Wilhelm Zwerger
Prüfer der Dissertation:	1.	Prof. Dr. Sebastian T. B. Goennenwein
	2.	Prof. Dr. Martin Stutzmann

Die Dissertation wurde am 10.10.2017 bei der Technischen Universität München eingereicht und durch die Fakultät für Physik am 17.10.2018 angenommen.

ABSTRACT

In this thesis, we investigate the two ferrimagnetic iron garnet materials *gadolinium iron garnet (GdIG)* and *yttrium iron garnet (YIG)* using ferromagnetic resonance. YIG is the ferrimagnetic insulator that exhibits the lowest damping of magnonic excitations reported in the literature to date. It is therefore of particular research interest and is used in many high frequency devices. GdIG is a compensating ferrimagnet which features a so-called compensation temperature at which the net remanent magnetic moment of the magnetically ordered system vanishes. Although iron garnet materials have been studied since decades, many of their properties still remain to be understood. In this thesis, we use various different ferromagnetic magnetic resonance techniques to quantify the magnetization damping, the magnetic anisotropy, the coupling to cavity photons, and the generation of spin currents in iron garnets.

In the first part of the thesis, we present detailed broadband ferromagnetic resonance studies of these two materials as a function of temperature from which we extract key magnetic properties such as the magnitude of the magnetization M and the magnetic anisotropy. For this, we design, build and characterize a broadband ferromagnetic resonance setup that operates up to 43.5 GHz and at temperatures between 4.2 and 300 K. To analyze the data, we develop an open source python library that contains conventional and novel background correction methods, semi-automated fit models and a graphical interface to quickly evaluate the (typically large) broadband FMR measurement data. For GdIG thin films, we find that the typical easy-plane anisotropy caused by the demagnetization field of the thin film is dominant only for low temperatures. Close to the compensation point, a perpendicular anisotropy, i.e. an anisotropy with its easy axis along the film normal, is observed instead. We are able to quantify the anisotropy

components using the broadband FMR data and confirm the findings using SQUID magnetometry. The temperature tunable perpendicular magnetic anisotropy found in GdIG is of considerable interest as it potentially allows to efficiently switch the magnetization optically or electrically via spin torques. Furthermore, we extract the ferromagnetic resonance linewidth of GdIG as a function of temperature and separate inhomogeneous broadening from a Gilbert-like damping in this material for the first time. The damping in compensating ferrimagnets gives insight into the interplay of ferromagnetic and antiferromagnetic magnons, a topic of great interest for example in the context of pure spin current transport. For YIG, the focus of the broadband ferromagnetic resonance study is the frequency and temperature evolution of the damping parameters. We find that for temperatures larger than 100 K, the linewidth increases linearly with frequency and that the slope (the Gilbert damping parameter α) decreases linearly with decreasing temperature. At lower temperatures, the linewidth exhibits a characteristic peak-like maximum at around 50 K. In contrast to the studies available in the literature, our temperature-dependent broadband FMR study provides a detailed frequency dependence of the linewidth. Using the frequency dependence of the linewidth maximum, we are able to determine slowly relaxing rare earth impurities as the most likely cause of this relaxation. The magnetic properties of YIG and GdIG determined in this part allow to assess their potential for applications as well as for continued fundamental research at low temperatures. In particular, the magnetization damping currently faces renewed interest as it is highly relevant for the use of materials with a magnetic ordered state in the scope of hybrid quantum memory systems. Using the temperature dependence of the resonance linewidths, we are able to shed light on the microscopic damping mechanisms at play in these materials.

In the second part of the thesis, we investigate the coupling of one YIG and one GdIG sample with the cavity mode of a microwave cavity resonator. In the first experiment, we use the temperature dependence of the net magnetization of GdIG to tune the coupling strength between the magnonic GdIG and the photonic cavity system in situ. We describe several approximative models that are used in the literature to evaluate the magnon-photon coupling and discuss their limitations in detail. In order to analyze the data in the intermediately strong coupled case quantitatively, we implement a new background correction method and perform fits of the complete, complex-valued transmission spectrum. Thereby, we successfully show the theoretically expected $\sqrt{M}$ dependence of the coupling rate experimentally.

In the second experiment, we strongly couple a YIG|Pt thin film bilayer to the microwave cavity and measure spin pumping electrically. In spin pumping, angular momentum is transfered from the YIG layer to the platinum layer where it is converted to a charge current via the inverse Hall effect which is detected electrically. We show that in the strong coupling regime, the spin pumping effect is still functional. Furthermore, we analyze the coupling of various standing spin wave modes of the YIG film and discuss the behavior when the coupling is tuned from weak to strong coupling. The results allow to observe the theoretically predicted signature of spin pumping in the strong coupling regime and allow to seamlessly link its experimental signature in the strong coupling regime to the well known characteristics in the weak coupling regime. Our findings represent a first step towards using spintronic effects in such strongly coupled systems. This field is developing rapidly and considerable progress has recently been made in coupling multiple magnetic moments via a cavity and in remote manipulation of spin currents by utilizing spin pumping.

ZUSAMMENFASSUNG

In der vorliegenden Doktorarbeit werden die zwei ferrimagnetischen Isolatoren *Gadolinium-Eisengranat* und *Yttrium-Eisengranat (YIG)* mittels ferromagnetischer Resonanzspektroskopie (FMR) untersucht. YIG weist die geringste Linienbreite aller magnetisch geordneten Substanzen auf. Es ist daher seit Langem von besonderem Interesse in der Forschung und wird zudem in vielen Hochfrequenzbauteilen verwendet. GdIG ist ein Ferrimagnet, der eine sogenannte Kompensationstemperatur aufweist, an welcher das remanente magnetische Moment des geordneten magnetischen Systems verschwindet. Obwohl Eisengranate schon seit Jahrzehnten untersucht werden sind doch noch viel der magnetischen Eigenschaften nicht hinreichend verstanden. Das Ziel dieser Doktorarbeit ist, das Verständnis der magnetischen Eigenschaften, der Dynamik und der Kopplung von magnetischen Anregungen mit Hohlraumresonatoren am Beispiel von Eisengranaten zu verbessern.

Im ersten Teil der Arbeit werden Breitband-FMR-Studien dieser beiden Materialien als Funktion der Temperatur diskutiert. Aus diesen Daten können wichtige magnetische Eigenschaften wie die Magnetisierung M oder die magnetische Anisotropie extrahiert werden. Zu diesem Zwecke entwickeln und charakterisieren wir einen Breitband-FMR Messaufbau, der es erlaubt, Messungen bis zu einer Frequenz von 43.5 GHz bei Temperaturen zwischen 5 und 300 K durchzuführen. Um die typischerweise sehr großen Messdaten zu analysieren entwickeln wir eine Softwarebibliotehek in Python, die konventionelle und neue Methoden zum Abzug des Untergrundsignals sowie Modelle zur halbautomatisierten Datenanalyse enthält. Diese Bibliothek ist als open-source Software frei zugänglich. Im Falle von GdIG stellt sich heraus, dass die für Dünnfilme typische *easy plane* Anisotropie nur für tiefe Temperaturen dominant ist und dass nahe der Kom-

pensationstemperatur stattdessen eine senkrechte magnetische Anisotropie beobachtet wird. Diese senkrechte magnetische Anisotropie in GdIG ist von großem Interesse, da es solch eine Anisotropie gegebenenfalls gestattet die Magnetisierung optisch oder elektrisch über Spinströme umzukehren. Wir verifizieren das Auftreten der senkrechten magnetischen Anisotropie durch unabhänige Magnetometrie-Messungen und quantifizieren die einzelnen Anisotropiebeiträge mittels Breitband-FMR. Darüberhinaus messen wir die frequenzabhängige Linienbreite der magnetischen Anregungen als Funktion der Temperatur und können damit zum ersten Mal den Beitrag einer inhomogenen Verbreiterung und einer Gilbert-ähnlichen Dämpfung trennen. Die Dämpfung in kompensierenden Ferrimagneten gibt einen Einblick in das Wechselspiel von ferromagnetischen und antiferromagnetischen Magnonen. Dies ist zum Beispiel im Kontext des Transports reiner Spinströme von erheblicher Wichtigkeit und wird derzeit an GdIG Einkristallen weiter untersucht. Im Falle der YIG-Breitband-FMR-Studie liegt der Fokus auf der Frequenz- und Temperaturabhängigkeit der Linienbreite. Für Temperaturen über 100 K zeigt sich ein linearer Anstieg der Linienbreite mit der Frequenz, dessen Steigung mit sinkender Temperatur abnimmt. Bei tieferen Temperaturen finden wird einen nichtlinearen Zusammenhang und ein charakteristisches Linienbreitenmaximum bei etwa 50 K welches von der Kopplung der Magnetisierung an Verunreinigungen herrührt. Über die Frequenzabhängigkeit des Maximums können wir feststellen, dass in dem untersuchten YIG vermutlich langsam relaxierende Seltenerdverunreinigungen die Ursache dieses Maximums sind. Die ermittelten Eigenschaften von YIG und GdIG erlauben es, ihr Potential für die Verwendung in Geräten und für die weitere Forschung bei tiefen Temperaturen abzuschätzen. Insbesondere die magnetische Dämpfung ist derzeit Gegenstand von großem Interesse, da Materialien mit magnetischer Ordnung für den Einsatz in hybriden Quanteninformationsspeichern in Betracht gezogen werden, wofür eine geringe Dämpfung eine Grundvoraussetzung ist.

Im zweiten Teil der Arbeit untersuchen wird die Magnon-Photon-Kopplung zwischen Anregungen eines Mikrowellenholraumresonators und Anregungen jeweils einer YIG- und einer GdIG-Probe. Im ersten Experiment benutzen wir die Temperaturabhängigkeit der GdIG-Magnetisierung um die Kopplungsrate zu steuern. Wir beschreiben typische approximative Modelle, die in der Literatur für die Analyse der Magnon-Photon-Kopplung verwendet werden und diskutieren deren Einschränkungen. Um die Kopplungsrate im Übergangsbereich zwischen starker und schwacher Kopplung quantitativ zu bestimmen entwickeln wir eine neue Methode des Unter-

grundabzugs und führen eine Modellanpassung an das komplette, komplexwertige Transmissionsspektrum durch. Mit diesen Daten gelingt es uns das theoretisch vorhergesagte $\sqrt{M}$-Verhalten der Kopplungsrate zwischen Resonator und GdIG Magnetisierungsanregung experimentell zu zeigen. In einem zweiten Experiment erreichen wir die starke Kopplung zwischen einem YIG|Pt Dünnfilmschichtsystem und dem Resonator und weisen nach, dass der Effekt des Spinpumpens auch im Bereich der starken Kopplung vorhanden ist. Im Spinpumpen wird Drehimpuls von der YIG-Schicht über einen Spinstrom in die anliegende Platin-Schicht übertragen, wo er mittels des inversen Spin-Hall-Effekts in einen Ladungsstrom umgewandelt wird, den wir elektrisch detektieren. Des Weiteren untersuchen wir die Kopplung von mehreren stehenden Spinwellen und diskutieren den kontrollierten Übergang des Systems von der starken in die schwache Kopplung. Die Ergebnisse erlauben es, die theoretisch erwartete Signatur des Spinpumpens im Bereich der starken Kopplung zu beobachten und direkt mit dem bekannten charakteristischem Verhalten im Bereich der schwachen Kopplung zu vergleichen. Unsere Ergebnisse sind ein erster Schritt für die Nutzung von spintronischen Effekten in stark gekoppelten Systemen. Dieses Arbeitsgebiet entwickelt sich derzeit rasant und es wurden bereits weitere wichtige Fortschritte in diesem Bereich erzielt. Kürzlich ist es beispielsweise gelungen, mehrere magnetische Momente über einen Hohlraumresonator zu koppeln und Spinströme aus der Ferne zu beeinflussen.

Table of contents

CHAPTER 1

INTRODUCTION

1.1 Background and Motivation

It is fair to say that our daily lives have been revolutionized by the tremendous progress in information technology (IT) during the last decades. In the early 1990's a computer in every home was a far fetched vision. Today, a computer in every pocket, on the wrist and in many every day devices is reality. The social implications of this revolution are an intriguing topic by itself but are of course not covered in this physics dissertation. In the following, we rather focus on the recent technical development and the role of magnetic materials in electronic devices. We will focus in particular on the understanding of the physical principles and properties of magnetic materials.

When the development of IT hardware is discussed, often only the electronic part is covered. The first bipolar transistor, the foundation of modern computers, was developed in 1948 as a point-contact transistor [8]. Since then, with the implementation of junction-based transistors [9] and the following technical developments, the reliability and the production costs have substantially improved. Today, the structure sizes of industrial fabrication processes of silicon-based integrated circuits have been miniaturized to the point where there are statistically only few tens of electrons in a transistor gate [10]. At the same time, the processing rates of these circuits reached several gigahertz. Together with the improvements of short term volatile memory (in particular random access memory, RAM), this

made the current processing power of electronics possible. During all this development, however, magnetic materials have been a corner stone of IT hardware.

The most notable application of ordered magnetic materials like ferromagnets or ferrimagnets is storage technology. Encoding information in the magnetization direction of segments of magnetic bands or disks has lead to very reliable long term data storage devices with staggering information densities around 1 Tb/in^2 [11]. The high reliability and the typical long retention times of magnetic storage media have been achieved by carefully tailoring the magnetic properties of the used materials. One key aspect is the magnetic anisotropy that influences the energy that is needed to flip the magnetization of a segment. It is carefully adjusted to a value at which the segment is unlikely to be flipped by thermal excitation. At the same time, the energy barrier needs to be small enough so that the segment can be flipped (i.e. the bit written) with a magnetic field that is sufficiently small and localized. This ensures that surrounding segments are unlikely to be affected. A milestone development that enabled the high storage capacity of current hard disk drives is the spintronic readout: By using the spin dependent transport of electrical currents in the giant magnetoresistance effect (GMR) [12, 13], the stray field of the magnetized segments can be read out very locally and sensitively. Another field in which magnetic materials are heavily used are radio frequency (rf) communication devices and components. The use of magnetic materials in rf communication circuits dates back more a century when a permalloy shield was employed in the first transatlantic telegraph cable. The permalloy shield served as inductive compensation which significantly reduced distortions of the signal and thereby allowed for higher data rates [14]. Since then, magnetic materials have become indispensable in rf components such as isolators, circulators and filters that are used for both wireless and also wired communication [15].

Looking at these well established examples one might get the impression that magnetic materials have already been used for decades and therefore, there is little room for innovation or basic research. However, recent discoveries show that the exact opposite is the case. Until now, applications of spintronic effects like the aforementioned GMR effect only employ the spin polarization of a charge current. However, the flow of angular momentum (a spin current), does not necessarily require the (lossy) transport of charge carriers but can also be achieved purely by magnetic excitations. The generation, transport properties and the detection of these so-called pure spin currents are interesting problems which give insight into the dynamics

of magnetic and nonmagnetic materials alike. A number of effects have recently been discovered that are effective with pure spin currents. These effects include the spin Hall magnetoresistance (SMR) [16, 17], spin pumping (Ref. [18] and Chap. 7) and its inverse effect (spin transfer torque) [19] and the spin Seebeck effect (SSE) [20, 21]. Even logic operations with pure spin currents or spin waves (magnon logic) are conceivable [22] which is another incentive to investigate spin currents. Using pure spin currents as carrier of information promises to overcome the biggest challenge in the design of integrated circuits today: The miniaturization of the circuits and the high switching rates leads to a large thermal power density on the chip that needs to be dissipated. One vision is to move the (inevitable) generation of heat to the off-chip area while on the chip, pure spin currents are used which do not generate Joule heat [23]. The viability of this approach is, however, debated since pure spin currents also show dissipation [24].

Nevertheless, there are many other possible uses of spintronic effects in devices which drive research apart from fundamental physical interest. One example which is particularly close to application already are spin torque oscillators (STOs) [25] which are based on magnetic nanostructures and are considered as novel ultra broadband frequency sources. The electronic rf oscillator circuit, that is the basis of all wireless communication, radar applications and audio devices has not changed in its principle since 1969 [26]. The limitation of these rf oscillators is typically the small bandwidth due to the necessary lumped element components such as capacitors and inductors which can not easily be built as integrated circuits. Therefore, typically many separate oscillator units are build into one device to cover different frequency bands and standards. Given the high bandwidth and tunability of STOs, they may allow to combine the oscillator units in the device into a single unit, allowing for smaller package sizes and lower power consumption than the current electronic oscillator circuits.

For the development of such components, a deep and quantitative understanding of magnetism and means to characterize magnetic materials is required. The high frequency properties are of particular interest when data processing and transmission is concerned. Especially dynamics in the gigahertz regime are of importance as this processing speed is finally what devices based on spintronic effects need to deliver in order to be competitive with conventional electronics. Magnetic materials are typically characterized into three categories: (i) diamagnets which contain no permanent magnetic moments but exhibit a finite magnetization due to induced magnetic moments when an external magnetic field is applied; (ii) para-

magnets which contain permanent magnetic moments that can be aligned along an external magnetic field; and (iii) materials in which the permanent magnetic moments of the material can show a spontaneous order even in the absence of an applied magnetic field. The two simplest cases of this spontaneous magnetic order are ferromagnetism and antiferromagnetism in which neighboring magnetic moments are aligned parallel and antiparallel, respectively. A wide variation of other ordered states is observed in nature such as a triangular arrangement [27], spiral ordering [28] or Skyrimons [29]. The most common order, however, is probably the case in which the magnetic moments are arranged as in an antiferromagnet but have a different magnetic moment and hence, a macroscopic magnetization results. This type of magnetic order is called ferrimagnetism and is the focus of this thesis. In particular, we will only deal with electrically insulating ferrimagnets. In contrast to conducting magnetic materials, no parasitic currents can be induced into insulating ferromagnets. This simplifies the description of the dynamics of the materials and is advantageous for their use in high frequency applications.

Garnet materials

Among the insulating ferrimagnets, garnet materials have been of interest to science for the last seven decades [30, 31] and are commonly used in high frequency applications such as filters or as passive components in circuits [32, 33]. The growth of single crystal garnets and the deposition of garnet thin films using sputtering, pulsed laser deposition or liquid phase epitaxy is therefore very advanced. The interest in garnets originates from the exceptionally low ferromagnetic resonance linewidth of the parent compound of magnetic iron garnets, yttrium iron garnet ($Y_3Fe_5O_{12}$, YIG). With a linewidth of only about 1 MHz at an excitation frequency of 10 GHz (the lowest linewidth of all ordered magnetic materials reported in the literature) it presents a high quality ($Q = 10000$) filter that selectively absorbs microwaves of a particular frequency. Furthermore, the ferromagnetic resonance frequency (the filter frequency) and the ferromagnetic resonance linewidth (the filter quality) can be tuned in a wide range by doping the garnet with rare-earth materials and by applying a static magnetic field. Due to its exceptionally low damping and its magneto-optical properties [MF1, 34, 35], YIG is also considered an ideal candidate for spintronic applications as well as spin-based quantum information storage and processing [36–39]. In particular, considerable progress has recently been made in im-

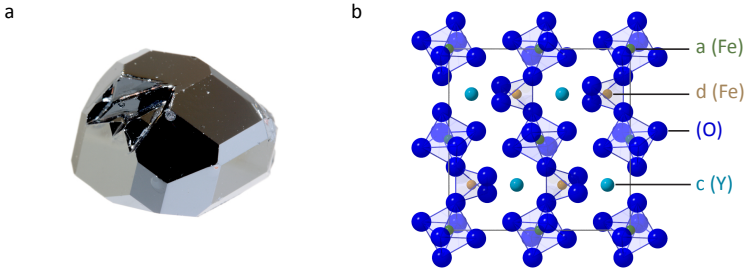

Figure 1.1: (a) Photograph of a yttrium iron garnet single crystal (from Ref. [42]). **(b)** Schematic cut through the middle of the YIG crystal unit cell (courtesy of Stephan Geprägs). The octahedral coordinated *a* lattice site, the dodecahedral *c* lattice site, and the tetrahedral coordinated *d* lattice site are indicated.

plementing schemes such as coupling the magnetic moments of multiple YIG spheres [37, 40] or interfacing superconducting quantum bits with the magnetic moment of a YIG sphere [38, 41].[1]

A YIG single crystal is shown in Fig. 1.1 (a). Note that despite being a large band gap (2.85 eV) insulator, YIG is typically not transparent due to oxygen defects [43, 44]. The conventional YIG crystal unit cell has a cubic symmetry and contains eight primitive unit cells. In Fig. 1.1 (b), a part of this large conventional unit cell is shown schematically. In this visualization, the three lattice sites that can be occupied by magnetic cations are visible: Fe^{3+} ions are situated on octahedral coordinated (*a*) and tetrahedral coordinated (*d*) lattice sites. These Fe^{3+} ions are coupled strongly[2] by indirect (superexchange) coupling via oxygen atoms and hence their magnetic moments align antiparallel. Due to the strong exchange coupling, the Curie temperature at which the magnetic order is lost due to thermal fluctuations is $T_{\mathrm{Curie}} = 560\,\mathrm{K}$ [45]. The non-vanishing net saturation magnetization of YIG ($M_{\mathrm{s}} \approx 180\,\mathrm{kA\,m^{-1}}$ at room temperature) arises because the crystal lattice hosts three Fe ions on the *d* lattice sites per formula unit and only two on the *a* lattice sites [46, 47]. The non-magnetic yttrium ions on the dodecahedral *c* lattice site can be substituted by other rare-earth ions which carry a magnetic moment. These ions couple comparatively weakly to the

[1] The preceding two sentences are adapted from Ref. [MF2].

[2] The ions on the *a* and *d* lattice site are coupled with an exchange energy $J_{ad} = 60\,\mathrm{meV}$, the ions on the same site are coupled with $J_{aa} = 6\,\mathrm{meV}$ and $J_{dd} = 20\,\mathrm{meV}$ [45].

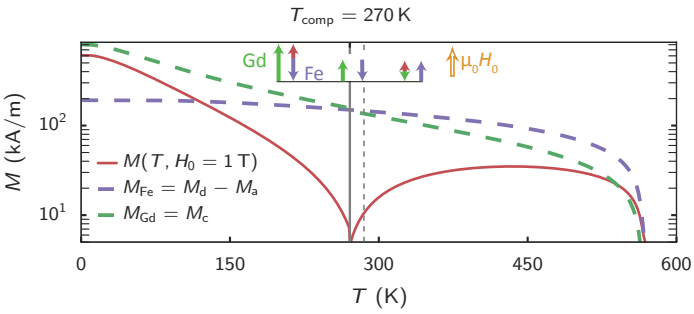

Figure 1.2: Calculated GdIG $M(T)$ for $H_0 = 1\,T$ (red line) and the magnetization of the effective Gd and Fe sublattices (dashed lines) according to Eq. (1.1) to (1.4). The gray lines mark the thin film (solid) and the bulk (dashed) compensation temperature at which the net remanent magnetization vanishes. The length of the arrows schematically represent the net Fe and the Gd sublattice magnetizations and the total net magnetization M. Below T_{comp}, the Gd sublattice magnetization dominates the net magnetization and is therefore aligned with H_0. Above T_{comp}, the net Fe magnetization dominates and hence all sublattice magnetizations flip in order to keep the net magnetization (red) aligned with the external field.

Fe ions on the *a* and *d* sites and are aligned antiparallel to the Fe ions on the *d* site.

A prototypical example of an iron garnet with a magnetic ion on the lattice *c* site is gadolinium iron garnet ($Gd_3Fe_5O_{12}$, GdIG or GIG). Due to the comparably weak coupling of the Gd magnetic moments amongst each other and with the iron ions, the magnetic sublattice formed by the gadolinium moments shows a paramagnetic-like behavior, i.e. its magnetization increases towards low temperatures following a Brillouin-like function. At room temperature, the net magnetization of GdIG is dominated by the magnetization of the iron sublattices and therefore, the net magnetization points along the larger Fe sublattice magnetization. However, as the magnetization of the Gd sublattice strongly increases with decreasing temperature, the net remanent magnetization decreases and vanishes at T_{comp}, where the sublattice magnetizations just compensate each other. Below T_{comp} the net magnetization increases again due to the increasing thermal polarization of the Gd sublattice and points along the Gd sublattice magnetization. At 5 K the net magnetization reaches a value of approximately $595\,kA\,m^{-1}$ [48].

Due to the existence of a compensation temperature, GdIG is called a compensating (or compensated) ferrimagnet.[3] It is instructive to model the GdIG magnetization by a Neel-theory approach which we outline in the remainder of this section, closely following the calculations of Ref. [31]. The individual magnetizations $M_{\mathrm{a,c,d}}$ of the three sublattices corresponding to the elements Fe, Gd and Fe, respectively, sum up to the total magnetization as

$$M = M_{\mathrm{a}} + M_{\mathrm{c}} - M_{\mathrm{d}}. \tag{1.1}$$

The field and temperature dependence of every sublattice is modeled by its Brillouin function $B(H_0, x_i)$

$$M_i^{\mathrm{mol}}(T, H_0) = M_i^{\mathrm{mol}}(0)\, B_{\mathrm{S}_i}(H_0, x_i) \tag{1.2}$$

with the external static magnetic field H_0 and

$$\begin{aligned} x_{\mathrm{d}} &= (S_{\mathrm{d}} g \mu_{\mathrm{B}}/k_{\mathrm{B}}T)(N_{\mathrm{dd}}M_{\mathrm{d}} + N_{\mathrm{aa}}M_{\mathrm{a}} + N_{\mathrm{dc}}M_{\mathrm{c}} \pm H_0) \\ x_{\mathrm{a}} &= (S_{\mathrm{a}} g \mu_{\mathrm{B}}/k_{\mathrm{B}}T)(N_{\mathrm{ad}}M_{\mathrm{d}} + N_{\mathrm{aa}}M_{\mathrm{a}} + N_{\mathrm{ac}}M_{\mathrm{c}} \mp H_0) \\ x_{\mathrm{c}} &= (S_{\mathrm{c}} g \mu_{\mathrm{B}}/k_{\mathrm{B}}T)(N_{\mathrm{cd}}M_{\mathrm{d}} + N_{\mathrm{ca}}M_{\mathrm{a}} + N_{\mathrm{cc}}M_{\mathrm{c}} \mp H_0), \end{aligned} \tag{1.3}$$

where the upper signs hold above and the lower signs below T_{comp}.

Here, N_{ij} are the dimensionless molecular field coefficients between the sublattice i and j ($N_{ij} = N_{ji}$), and the electron spin S_i of the ion on the respective lattice site. The coupled equation system Eq. (1.2) hence describes the magnetization arising from the spin polarization of each sublattice taking into account the molecular field of all other sublattices. The magnetic moments per formula unit at $T = 0\,\mathrm{K}$ are given by

$$\begin{aligned} M_{\mathrm{d}}^{\mathrm{mol}}(0) &= 3 g_{\mathrm{d}} S_{\mathrm{d}} \mu_{\mathrm{B}} N_{\mathrm{A}} \\ M_{\mathrm{a}}^{\mathrm{mol}}(0) &= 2 g_{\mathrm{a}} S_{\mathrm{a}} \mu_{\mathrm{B}} N_{\mathrm{A}} \\ M_{\mathrm{c}}^{\mathrm{mol}}(0) &= 3 g_{\mathrm{c}} S_{\mathrm{c}} \mu_{\mathrm{B}} N_{\mathrm{A}} \end{aligned} \tag{1.4}$$

where N_{A} is Avogadro's number. For GdIG, $S_{\mathrm{d,a}} = \frac{5}{2}$, $S_{\mathrm{c}} = \frac{7}{2}$ and $g_i = 2$. Note that taking the g-factor of all sublattices to be identical is sufficient for the calculation of the GdIG magnetization. For the calculation of the FMR modes of GdIG, however, slightly different g-factors for the Gd and Fe sublattices need to be taken into account as we will see in Chap. 4. We finally note that in order to convert the magnetization per

[3] The preceding lines of this paragraph are adapted from Ref. [MF3].

formula unit M_i^{mol} to a volume normalized magnetization M we simply use the density of GdIG ($\rho = 6.45\,\mathrm{g\,cm^{-3}}$ [49]) and the molar masses of the constituent elements. The model is calculated by taking the values for N_{ij} to $N_{\mathrm{dd}} = -30.4, N_{\mathrm{aa}} := -65, N_{\mathrm{ad}} := 97, N_{\mathrm{dc}} := 6.0$, and $N_{\mathrm{cc}} := 0$ as determined for GdIG by Dionne [31] and $N_{\mathrm{ac}} := -3.57$ to account for the slightly different compensation temperature in the thin films that are investigated in this thesis. The compensation temperature $T_{\mathrm{comp}} = 270\,\mathrm{K}$ of the thin films is lower than the bulk value of 285 K [48] (dashed line in Fig. 1.2). This is in agreement with the literature suggesting that T_{comp} is slightly reduced in thin films [50, 51].

The resulting net magnetization M, the net Fe sublattice magnetization M_{Fe} and the Gd sublattice magnetization M_{Gd} are shown in Fig. 1.2 as a function of temperature. Due to the weak coupling of the Gd and the Fe sublattices, the summed effective Fe sublattice magnetization M_{Fe} is essentially identical to the temperature evolution of the YIG magnetization.

1.2 Magnetization dynamics in a nutshell

In the following chapters, the magneto-dynamics of ferrimagnets are investigated and discussed in detail. While the two experimental techniques that we use to investigate the magneto-dynamics (see below) are distinctly different tools and the description of the arising signal is therefore also different, the common ground is the damped precessional motion of the exchange-coupled magnetic moments. In this section, a brief introduction to the theoretical description of these magneto-dynamics is given. We limit the discussion to the parts of the theory relevant for the following chapters and aim to rather give the physical key facts than an in-depth derivation. For a detailed treatment, we refer the reader to the seminal works of Vonsovskii [52], and Gurevich and Melkov [53].

When the externally applied magnetic fields and the excitations energies used to drive magnetic resonance are much smaller than the exchange coupling energy of the magnetic moments in the material, the magneto-dynamics can be described by treating the ferrimagnet as a single macrospin. The classical equation of motion of the magnetization $\mathbf{M}$ of the material is then given by the Landau-Lifshitz-Gilbert equation (LLG) [54, 55]

$$\frac{\mathrm{d}\mathbf{M}}{\mathrm{d}t} = -|\gamma|\left[\mathbf{M}\times\mu_0\mathbf{H}_{\mathrm{eff}}\right] + \frac{\alpha}{|\mathbf{M}|}\left[\mathbf{M}\times\frac{\mathrm{d}\mathbf{M}}{\mathrm{d}t}\right]. \tag{1.5}$$

Here, γ is the gyromagnetic ratio and α is the Gilbert damping parameter. The effective field $\mathbf{H}_{\text{eff}} = \mathbf{H} + \mathbf{H}_{\text{ani}}$ is given by the superposition of an externally applied magnetic field $\mathbf{H}$ and the anisotropy fields $\mathbf{H}_{\text{ani}}$ of the ferromagnet. For a static $\mathbf{H}$, the orientation of $\mathbf{H}_{\text{eff}}$ hence is the equilibrium orientation of $\mathbf{M}$.

Neglecting the last term, Eq. (1.5) describes the precessing movement of $\mathbf{M}$ around $\mathbf{H}_{\text{eff}}$. The gryomagnetic ratio γ can be related to the g-factor by $\gamma = g\mu/\hbar$ where $\hbar$ is the reduced Planck constant and $\mu = q\hbar/(2\tilde{m})$ is the magneton of the particles with mass $\tilde{m}$ and charge q giving rise to the magnetic moment. Magnetism in ferromagnets is typically caused by the spin of electrons and hence $g \approx 2$. The deviation from the free electron g-factor $g = 2.0023$ gives insight into the spin-orbit coupling in a ferromagnet [53]. Note that the magnetization precesses around the effective field in a right handed fashion which is implicit in the signs of the above, conventional, definition of the LLG. A left-handed precession can be taken into account by explicitly considering the sign of γ. As we do not investigate resonances with a left handed precession of the magnetization in the following, we retain the simple definition of the LLG which disregards this aspect. The absolute value of γ and $H_{\text{eff}} = |\mathbf{H}_{\text{eff}}|$ give the precession frequency, $\omega_{\text{res}} = \gamma\mu_0 H_{\text{eff}}$. With a typical gyromagnetic ratio of $\gamma/(2\pi) = 28\,\text{GHz}\,\text{T}^{-1}$ ($g = 2$) this gives a resonance frequency in the gigahertz (microwave) regime for typical magnetic fields of a few tesla. Ferromagnetic resonance can also be described in a quantum mechanical particle picture, where the excitation of the magnetization is quantized and the corresponding bosonic quasiparticles are called magnons. A magnon carries an angular momentum of $\hbar$ corresponding to a single spin in the coupled magnetic system that is flipped. Picturing a magnon in the classical word can be done by describing the flipped spin as distributed tilt of all magnetic moments. In the following, we will retain the classical picture.

Upon displacing $\mathbf{M}$ from its equilibrium direction, it moves back to equilibrium in a spiraling trajectory due to the relaxation by scattering with phonons or magnons, or the emission of photons. The last term in Eq. (1.5) phenomenologically describes this damping of the magnetization precession. The time scale of this relaxation is given by α. In detail, the relaxation rate κ_{s} and hence the resonance linewidth $\Delta\omega$ for a Gilbert-type damping term as in Eq. (1.5) depends on the precession frequency ω_{res} as follows [56]:

$$\frac{1}{2\kappa_{\text{s}}} = \Delta\omega = 2\alpha\omega_{\text{res}} + \Delta\omega_0 \tag{1.6}$$

Here, the inhomogeneous broadening $\Delta\omega_0$ phenomenologically accounts for contributions to the relaxation that do not depend on the precession frequency such as relaxation via magnetic inhomogeneities or surface scattering. Note that $\Delta\omega$ is the full width at half maximum (FWHM) resonance linewidth as shown in Fig. 1.3 which is commonly used in FMR experiments as in Part I. Part II, however, we use the inverse of the half width at half maximum (HWHM) resonance linewidth for the relaxation rate κ_s, which is the more common notation when the coupling of two resonant systems is concerned.

To obtain solutions for Eq. (1.5), we first neglect all anisotropy fields ($\mathbf{H}_{\text{ani}} = 0$) and consider an external static magnetic field H_0 applied parallel to the z-direction $\mathbf{H}_0 = (0,0,H_0)$. The axis of precession and the equilibrium direction of $\mathbf{M}$ are therefore also aligned along $\mathbf{z}$. We take a dynamic externally applied magnetic field into account and separate the dynamic parts of $\mathbf{H}$ and $\mathbf{M}$ in a static and a dynamic part

$$\mathbf{H} = \mathbf{H}_0 + \mathbf{h}_{\text{MW}}(t) \tag{1.7}$$

$$\mathbf{M} = \mathbf{M}_0 + \mathbf{m}(t). \tag{1.8}$$

Due to the typical precession frequencies in the microwave range, $\mathbf{h}_{\text{MW}}$ is also-called the microwave magnetic field. For a small microwave magnetic field $\mathbf{h}_{\text{MW}}$ perpendicular to H_0, the precessing magnetization can be approximated as $\mathbf{M} = (m_x(t), m_y(t), M_0)$ where M_0 is the absolute value of the static magnetization and $\mathbf{m}$ is the vector of the dynamic transversal components of $\mathbf{M}$. The solution of the linearized LLG [53] for an harmonic time dependence is then given by $\mathbf{m} = \overleftrightarrow{\chi}\mathbf{h}_{\text{MW}}$ with the microwave magnetic field $\mathbf{h}_{\text{MW}} = (h_x(t), h_y(t), 0)$ and the high frequency magnetic susceptibility tensor (Polder tensor)

$$\overleftrightarrow{\chi} = \begin{pmatrix} \chi_{11} & i\chi_{12} \\ -i\chi_{12} & \chi_{22} \end{pmatrix}. \tag{1.9}$$

The diagonal elements ($\chi = \chi_{11} = \chi_{22}$ neglecting anisotropies) of the Polder tensor, typically called the Polder susceptibility, determine the response of the magnetic system to a linear excitation field $\mathbf{h}_{\text{MW}}$ and are thus of particular interest. Neglecting terms $\mathscr{O}\left(\alpha^2\right)$, χ is given by

$$\chi(\omega, H_0) = \frac{\omega_{\text{M}}\left[\gamma\mu_0 H_0 - i\Delta\omega\right]}{\left[\omega_{\text{res}}(H_0)\right]^2 - \omega^2 - i\omega\Delta\omega}, \tag{1.10}$$

with the resonance frequency ω_{res} and $\omega_{\text{M}} = \gamma\mu_0 M_0$ [57, 58]. In Fig. 1.3, χ is shown as a function of ω around ω_{res}. Summarizing, the above

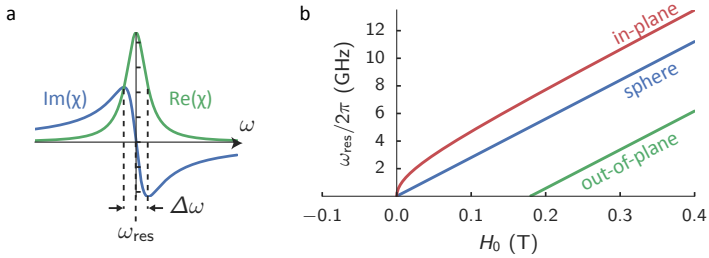

Figure 1.3: (a) The Polder susceptibility χ at fixed external magnetic field strength H_0 as a function of ω close to the ferromagnetic resonance frequency ω_{res}. Also indicated is the FWHM linewidth $\Delta\omega$. **(b)** ω_{res} as a function of H_0 taking into account the shape anisotropy for a sphere, an out-of-plane magnetized thin film and an in-plane magnetized thin film, respectively.

derivation describes the linear response of a ferromagnet to an external static magnetic field $\mathbf{H}_0$ in combination with a dynamic magnetic field $\mathbf{h}_{\text{MW}}$, $\mathbf{H} = (h_x, h_y, H_0)$ in the absence of magnetic anisotropies.

Typical magnetic anisotropy fields in ferromagnets are on the order of several millitesla and therefore influence the FMR dispersion at low magnetic fields sensitively. Considering only shape anisotropy ω_{res} can easily be derived following the works of Kittel [59]. For this, one considers an small ellipsoid for which the demagnetization field can be expressed using the spatially independent demagnetization tensor $\overleftrightarrow{\mathbf{N}}$ as

$$\mathbf{H} = \mathbf{H_0} + \mathbf{H}_{\text{demag}} + \mathbf{h}_{\text{MW}} = \mathbf{H_0} - \overleftrightarrow{\mathbf{N}}\mathbf{M} + \mathbf{h}_{\text{MW}} \tag{1.11}$$

with the demagnetization field $\mathbf{H}_{\text{demag}}$. The demagnetization tensor is symmetric and becomes diagonal in the axis frame of the ellipsoid. The diagonal elements $N_{x,y,z}$ are called the demagnetization factors which depend sensitively on the sample geometry. In this framework, the equation for the resonance frequency, called the Kittel equation, reads [59]

$$\omega_{\text{res}} = \gamma\mu_0 \sqrt{(H_0 + (N_y - N_z)M_0)\,(H_0 + (N_x - N_z)M_0)}. \tag{1.12}$$

In the following, we will consider three sample geometries: (i) A sphere, (ii) a thin film magnetized in plane, and (iii) a thin film magnetized out of plane (along the film normal). The resonance frequency in these cases are given by:

(i) Sphere ($N_x = N_y = N_z = 1/3$):

$$\omega_{\text{res}} = \gamma\mu_0 H_0 \tag{1.13}$$

(ii) Thin film magnetized in-plane, film normal along $\hat{\mathbf{y}}$ ($N_x = N_z = 0, N_y = 1$):

$$\omega_{\text{res}} = \gamma\mu_0 \sqrt{H_0 \left(H_0 + M_0\right)} \tag{1.14}$$

(iii) Thin film magnetized out-of-plane, film normal along $\hat{\mathbf{z}}$ ($N_x = N_y = 0, N_z = 1$):

$$\omega_{\text{res}} = \gamma\mu_0 \left(H_0 - M_0\right) \tag{1.15}$$

Typically only small magnetic fields strengths H_0 are required to saturate a ferromagnet and hence, the absolute value of magnetization M_0 can be taken to be equal to the saturation magnetization M_s when only shape anisotropy is relevant. When other anisotropies enter, it is customary to replace M_0 with the so-called effective magnetization M_eff which is essentially identical to the anisotropy field along the applied magnetic field axis. When M_s is known, M_eff can be separated into shape and additional anisotropy contributions (Chap. 4). The characteristic dispersion relations $\omega_\text{res}(H_0)$ for the three cases are shown in Fig. 1.3 (b). Note that for a sphere, the effect of the sample shape vanishes because no demagnetization field forms in the sample due to the high symmetry. For fundamental studies of the intrinsic properties and microscopic processes, spheres (as used in Chap. 3) are therefore particularly suited. The demagnetization factors for the thin films given above strictly hold for infinite thin films only. However, for the ratios of lateral dimensions and thickness of the samples investigated in this thesis, the approximations of infinite thin films are accurate to 5×10^{-3}.[4] For non-ellipsoid shapes such as the investigated films, the demagnetization factors become spatially dependent, reflecting the change in demagnetization field towards the corners of the sample [61]. This effect too, is for the shapes of the investigated samples negligible as it concerns only a small volume of the sample.

Taking the magnetic anisotropies of a material into account can also be done by a free enthalpy (Gibbs energy) approach [62–64] for any combination of anisotropy contributions such as magnetocrystalline, strain induced and shape anisotropy. Also the Polder susceptibility tensor can be derived

[4] The demagnetization factors of a 3 µm thin disc with a 3 mm diameter on its center axis are $N_{x,y,z} = (0.0016, 0.0016, 0.997)$ [60].

using this approach by considering that the gradient of the free enthalpy density G of the magnet with respect to the components of $\mathbf{M}$ gives the effective field of the precession, $\mu_0 \mathbf{H}_{\text{eff}} = \nabla_{\mathbf{m}} G$. Magnetic anisotropies do not only modify the dispersion relation but can also give rise to an elliptic precession of the magnetic moments which leads to $\chi_{11} \neq \chi_{22}$. In detail, the amplitude and the lineshape of χ_{11} and χ_{22} will be slightly modified. For thin films magnetized in plane, in which case shape anisotropy typically plays the dominant role, and for small H_0, this effect is particularly pronounced. In the following, we will discuss FMR of out-of-plane magnetized films. In this case, the shape anisotropy does not induce an elliptic precession as the magnetization precesses in the film plane which does not contain any distinguished direction and therefore $\chi_{11} = \chi_{22}$. The susceptibility as a function of the magnetic field in this case is [65]:[5]

$$\chi(\omega, H_0) \approx \frac{M_0 \left(H - M_{\text{eff}}\right)}{\left(H - M_{\text{eff}}\right)^2 - \left(\frac{\omega}{\gamma \mu_0}\right)^2 + i\Delta H \left(H - M_{\text{eff}}\right)}. \tag{1.16}$$

Here, ΔH is the FWHM linewidth in field space and H_{res} is introduced via the effective magnetization by substituting the M_{eff} according to the dispersion relation (Eq. (1.15)) by $M_{\text{eff}} = H_{\text{res}} - \frac{\omega}{\gamma \mu_0}$. This form of the susceptibility can also be derived by taking the demagnetization field into account by using Eq. (1.11) in the LLG (Eq. (1.5)) and the above outlined derivation.

We will use this form which includes the anisotropy explicitly in Chap. 4 in order to facilitate comparison with existing literature. Note, however, that the lineshape is always given by a complex Lorentzian as shown in Fig. 1.3 (a). Furthermore, we intentionally perform our broadband FMR experiments in the high field limit, in which case the effects of the magnetic anisotropy on the lineshape are negligibly small.

Technical realization of FMR

In a ferromagnetic resonance experiment, the precession of the magnetization is excited via the oscillating microwave magnetic field $\mathbf{h}_{\text{MW}}$. This magnetization precession is then detected inductively, typically using the same circuit. As discussed before, FMR is usually described in linear response, taking $\mathbf{m} = \overleftrightarrow{\chi} \mathbf{h}_{\text{MW}}$ with $\mathbf{m}$, the vector of the dynamic precessing

[5] Mind that Eq. (5) of Ref. [65], contains are two misprints which are corrected in the form which we give here.

components of the magnetization $\mathbf{M}$, and $\overleftrightarrow{\chi}$, the Polder susceptibility tensor. Technically, to measure this response, the absorption and the induced phase shift of high frequency (microwave) radiation in a magnetic sample needs to be recorded as a function of the externally applied field $\mathbf{H}_0$ and/or the microwave frequency ω. There are two main approaches to implement FMR that vary in the way $\mathbf{h}_{\mathrm{MW}}$ is created and detected: Cavity FMR (Part II) and broadband FMR (Part I).

In cavity FMR, a fixed frequency stimulus is applied to a microwave cavity resonator loaded with the sample under investigation and the reflected (or transmitted) power is detected. The FMR is excited by the microwave magnetic field h_{MW} of the standing waves that form in the cavity resonator. In this case, the excitation frequency is fixed to the cavity frequency and hence, H_0 is the only free parameter. The coupling of the cavity and the magnetic sample are discussed in detail in Part II. In broadband FMR on the contrary, a microwave stimulus of variable frequency is applied to a waveguide where propagating microwaves pass by the sample and excite the FMR precession with their magnetic field. The microwaves in broadband FMR are often excited and detected heterodyne using a vector network analyzer. In both cases, frequencies up to around 80 GHz can be generated experimentally using commercially available frequency sources or vector network analyzers. However, designing the microwave network such that variable frequencies can be transmitted in such a broad frequency range is non-trivial. Technical details to achieve a good microwave performance up to 43.5 GHz and to achieve reliable broadband FMR measurements are given in Chap. 2.

For both techniques, an external magnetic field H_0 needs to be generated. Electromagnets are a convenient way of sweeping and stabilizing arbitrary values of H_0 in a certain range. In small scale facilities, water-cooled electromagnets and superconducting magnets are common. The difference between the two approaches is the field range, the homogeneity, the stability and the speed at which the magnetic field can be varied. Superconducting magnets allow to generate fields up to 20 T which can be stabilized fluctuation free when a persistent ring current is flowing in the coils. They, however, suffer from a very slow ramp rate (around $2\,\mathrm{T\,min^{-1}}$). Water-cooled electromagnets on the other hand can typically generate no more than 2.5 T but allow to reach these fields in a few seconds if necessary. Additionally, the magnetic field is confined between the pole shoes of the water-cooled electromagnet which leads to a high homogeneity of the magnetic field. For superconducting magnets, the field homogeneity varies

with the specific technical realization of the magnet coils and can be on par with water cooled electromagnets.

Water cooled electromagnets are typically used in room temperature setups due to their fast ramp rate, their high field homogeneity and the versatility of mounting the sample in between the pole shoes. Superconducting electromagnets are typically used, in variable temperature setups that already provide the liquid helium temperature environment needed for the operation of the magnet. They offer high fields and high long time stability.

1.3 Outline

In this thesis, we aim to improve the understanding of the magnetic properties and the high frequency dynamics of magnetic garnet materials (in both thin film and bulk crystal form) and investigate their interplay with microwave photon states and spintronic effects. The thesis is structured as follows:

- In Part I, we approach the two garnet materials yttrium iron garnet and gadolinium iron garnet from a fundamental point of view and investigate their static and dynamic properties as a function of temperature using broadband ferromagnetic resonance. With the extracted temperature dependence of the resonance linewidth, we are able to shed light on the microscopic damping mechanisms at play in these materials. Furthermore, we find that the uniaxial magnetic anisotropy axis of GdIG can be tuned by temperature. In GdIG thin films, this allows tuning the magnetic axis from parallel to the film plane (easy plane) to perpendicular to the film plane (perpendicular magnetic anisotropy, PMA). This presents a very intriguing property that holds a big potential for further research.

- In Part II, we investigate the coupling of the magnetic excitations (magnons) in the same two materials with the photons in a microwave cavity. This approach holds the promise to controllably convert magnonic into photonic excitations and vice versa, which both hold their particular advantages such as the easy manipulation of the magnonic state using microwaves and the easy transmission of photons over long-distances. We demonstrate that in magnetic

materials with long range order, the same scaling behavior of the coupling rate of magnons and photons as in paramagnets holds, where the coupling rate increases with the square root of the number of polarized spins. Thereby, we experimentally confirm a fundamental theoretical conjecture. We furthermore show that in such coupled systems, spin pumping is still effective and can be used to read out the magnonic state.

- Finally, in Chap 9 we connect the main results from the previous chapters and give an outlook into further research that is enabled by the work presented in this thesis.

- In the appendix, the architecture of the data analysis library developed during the thesis is briefly described (Sec. A.1) and a more in-depth description of the cryogenic dip-stick used to perform the broadband ferromagnetic resonance experiments is given (Sec. A.2).

PART I

BROADBAND FMR

Table of Contents

INTRODUCTION

Before any of the devices mentioned in Chap. 1 can be realized, a first important step is to characterize the magnetic properties of the materials under consideration. Only when the underlying magnetism is well understood and the characteristics of the magnetic materials are well known, (spintronics) effects in hybrid structures involving these materials can be exploited. Finally, this knowledge of the basic magnetic properties then allows to predict and optimize a potential device's performance.

Many techniques have been developed to measure magnetic properties such as the (saturation) magnetization or the Curie temperature of ferromagnets. Well known are SQUID (superconducting quantum interference device) and vibrating sample magnetometry which measure the static (DC) susceptibility allowing to infer magnetic properties. In magnetic resonance measurements, which will mainly be used in this thesis, the high frequency susceptibility is recorded which also allows to determine these fundamental properties. Magnetic resonance is, however, a more versatile tool that excels in particular in measuring the magneto-dynamics of a material.

In the following, we will use *ferromagnetic* resonance (FMR) which accesses the exchange-coupled magnetic moments of the electron system. A brief theoretical description of FMR has been given in the previous chapter where anisotropies have mostly been neglected. For many materials, however, the magnetic anisotropy energies and the Zeeman energy, the dipolar interaction energy between the ferromagnet's magnetization and the externally applied magnetic field, are of a similar magnitude. Magnetic anisotropies can substantially alter the equilibrium orientation of the magnetization $\mathbf{M}$ and can be expressed as a contribution to an effective magnetic field $\mathbf{H}_{\text{eff}}$. As apparent from the description in Sec. 1.2, the magnetic anisotropy therefore has a large impact on the $\omega_{\text{res}}(H_0)$ dependence, that

is, on the measured resonance frequency or the field of resonance. Hence, the anisotropy parameters can be extracted by changing the direction of the applied magnetic field. One experimental method is to perform FMR measurements at a fixed stimulus frequency for several directions of the applied field while sweeping the applied magnetic field strength H_0. This type of angle-dependent studies is the conventional approach of performing anisotropy studies with FMR. When this approach is not feasible (e.g. due to a complex sample geometry or due to restrictions of the experimental setup), disentangling anisotropy contributions and the Zeeman energy requires measurements at multiple frequencies. Broadband FMR (bbFMR) is designed for this type of measurement. It allows to record the response of the magnetic system not only as a function of the H_0 but also as a function of the microwave frequency ω. From this data, the FMR dispersion relation is extracted that allows access to the gyromagnetic ratio γ and reflects the magnetic anisotropy.

Apart from the resonance frequency, also the linewidth $\Delta\omega$ is obtained in an FMR experiment. The linewidth is a measure for the relaxation time of a magnetic excitation of a specific frequency. Several different relaxation processes have been reported in the literature and are typically characterized into intrinsic and extrinsic relaxation processes. The intrinsic relaxation mechanisms of a material are described on the basis of the scattering of magnons with other magnons or phonons (cf. Chap. 3). The extrinsic contributions to the linewidth are, in contrast to the intrinsic contributions, not inherent to the defect free bulk material. They are for example be caused by defect or surface scattering [MF4] and can be of a similar magnitude or even surpass the intrinsic linewidth by orders of magnitude [52]. Another interesting example of an external contribution is the transfer of angular momentum from the ferromagnet to adjacent materials [66]. The ferromagnetic linewidth therefore is a measure for spin currents flowing in or out of the ferromagnet. Typically, the frequency and temperature dependences of the various relaxation mechanisms are distinctly different. Hence, in order to disentangle the relaxation mechanisms, the linewidth needs to be recorded as a function of the stimulus frequency and temperature. Broadband FMR is the method of choice for these studies. A setup to investigate the temperature, field and frequency-dependent magnetic resonance spectra was designed in the course of this doctorate.

This part is structured as follows: We first give a brief introduction to the detection of ferromagnetic resonance using planar microwave structures (Chap. 2). After a description of the experimental setup, we focus

on a novel method for a quantitative analysis of the FMR signal in the frequency domain and compare different analysis methods at the example of a permalloy thin film (Sec. 2.2). In Chap. 3, we investigate the temperature dependence of the magnetic properties and in particular the damping of the magnetostatic modes of an yttrium iron garnet sphere. Here, we employ the model of a slow relaxing impurity ion in combination with a Gilbert-like damping model to describe the temperature evolution of the FMR linewidth. In Chap. 4, we analyze the temperature-dependent magnetic anisotropy and damping of a [111]-oriented gadolinium iron garnet thin film. Using SQUID magnetometry and FMR measurements, we find that the magnetic anisotropy changes smoothly from an in-plane anisotropy to a perpendicular anisotropy. We trace this behavior back to the compensation of the magnetic moment of the gadolinium and iron sublattices of the material at the compensation temperature. Chapter 5 summarizes the findings of both studies.

CHAPTER 2

TECHNICAL ASPECTS & SETUP

In a ferromagnetic resonance experiment, the precession of the magnetization is excited via an oscillating microwave magnetic field $\mathbf{h}_{\mathrm{MW}}$ and detected inductively by the change of the microwave transmission or reflection. In a bbFMR measurement, this dynamic magnetic response is measured as a function of the stimulus frequency and the static magnetic field. Typically, waveguides are employed to create $\mathbf{h}_{\mathrm{MW}}$ and detect the inductive response.

In order to achieve reliable bbFMR measurements, several technical challenges must be faced that lead to design goals for an optimal experimental setup:

(i) *Detecting FMR in a frequency band as broad as possible* is desirable. Typical metallic ferromagnets exhibit a saturation magnetization $\mu_0 M_s$ of 1-2 T and $g \approx 2$. As an example, the theoretically expected FMR dispersion of a permalloy ($Ni_{80}Fe_{20}$, Py) film is shown in Fig. 2.1. For $\mu_0 H_0 = 2\,\mathrm{T}$, applied perpendicular to the film plane, $\omega_{\mathrm{res}}/2\pi \approx 41\,\mathrm{GHz}$ while for the same value of H_0 applied in the film plane, the ω_{res} is as high as 83 GHz. It is immediately obvious that detecting FMR in a frequency band that spans several tens of gigahertz is required to reliably extract the magnetic properties in different configurations. A wide frequency range is particularly important when the magnetic damping is studied. The often employed

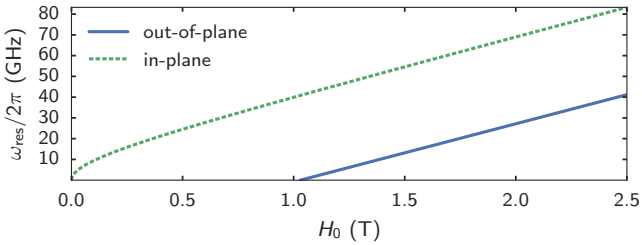

Figure 2.1: Calculated dispersion relation (Eqs. (1.14) and (1.15)) of a permalloy film (M_s= 1.03 T, $g = 2.052$ [MF5]) with the magnetic field applied in the film plane (dashed line) and perpendicular to the film plane (solid line).

phenomenological Gilbert-like damping (cf. Sec. 1.2) implies that the linewidth increases linearly with frequency. Data analysis in a too narrow frequency band can easily lead to an ambiguity of the extracted parameters (cf. Chap. 3).

(ii) *Exciting only a single electro-magnetic mode of the microwave* in the waveguide over the whole band is essential. This way, the density of states of the photons varies in a predictable manner and hence, damping via the radiant emission of photons can be controlled. Furthermore, by exciting only a single waveguide mode, effects of the coupling between the microwave mode and the magnonic excitations as investigated in detail in Part II are avoided.

(iii) *Concentrating h_{MW} at the sample location* and hence achieving a large inductive coupling of waveguide and magnetic sample is beneficial for a high sensitivity. Care has to be taken, however, that this large coupling does produce a dominant relaxation channel for the magnonic excitations.

(iv) *Reducing the frequency and magnetic field-dependent background signal* is important in order to efficiently recover the signal of interest.

(v) *Control over the sample temperature* is often necessary in order to gain insight into the microscopic origin of damping and anisotropies.

2.1 Experimental setup

Many of these criteria can be fulfilled by using planar microwave transmission lines as the waveguide. In these 2D structures, the microwave magnetic field required for FMR is the Oersted field of the microwave current that flows in a metalized strip on a dielectric substrate. For an FMR measurement, the sample under investigation is placed directly on top of the structure as shown in Fig. 2.2. A particularly suited variation of such a planar transmission line are coplanar waveguides (CPWs) as displayed in a photograph and as a schematic side view in Fig. 2.2 (a-c). Here, a microwave current flows in the center conductor of width w that is separated by two gaps of width g from the ground planes that are kept on zero potential. Also the back side of the dielectric substrate is metalized and kept on zero potential. In this particular design, the electric field is mainly confined between the back and the front ground plane. Thereby, the effect of metal parts of the setup in the vicinity of the CPW that are on a floating potential on the transmission is reduced.

Any discontinuities in the characteristic impedance Z_0 in a microwave network give rise to reflections [15]. Therefore, impedance discontinuities need to be avoided in order to achieve a broadband single mode microwave transmission (i and ii). As typical microwave equipment, i.e. the connectors, cables and devices, are designed for $Z_0 = 50\,\Omega$, the characteristic impedance of the CPW is designed to have the same value. This can be achieved by adjusting w, g, the substrate thickness t and its dielectric constant ε_r. For the optimization, analytic [67] and finite-element [68, 69] models can be used. The nominal designs that we use are listed in Tab. 2.1. In addition to these optimizations, the ends of the CPW center conductor are tapered to account for the pin of the end-launch connector which is used to connect the CPW and the standard microwave cable and to keep the impedance at this position at $50\,\Omega$. Finally, vias, metalized holes that connect the top and bottom ground planes (cf. Fig. 2.2 (a) and (b)), are used to avoid standing microwave modes in the ground planes. During this doctorate, these optimizations have been performed and several different designs are compared in detail in the master thesis of Philip Louis [64], whom I advised in the lab during his thesis work.

In the following, we use two different CPW designs (Tab. 2.1) created by Mathias Weiler that vary in the center conductor width w.[1] This parameter is of particular importance as it directly determines the profile of the microwave magnetic field [70]. As a rule of thumb, at a distance of w above the CPW, the microwave magnetic field component parallel to the CPW plane falls to half of the value that it reaches at the surface of the center conductor (Fig. 2.5 (b)). Hence, for thin magnetic films a narrow center conductor is favorable in order to concentrate h_{MW} at the sample position, thereby generating a large inductive coupling of sample and center conductor (iii). In the scope of cavity FMR, a similar concept applies and the concentration of the magnetic field at the sample location is expressed as the cavity "filling factor" (Chap. 6).

Table 2.1: Nominal CPW design parameters. The metalization (17.5 µm Cu plated with 5.5 µm Ag) and the overall dimensions (12.7 mm x 25.4 mm) are common in both designs.

Substrate	ε_{r}	t (µm)	w (µm)	g (µm)
RO 3006[2]	3.38 ± 0.05	127 (5 mil)	75	120
RO 4003[3]	6.15 ± 0.15	203 (8 mil)	340	135

Typically, nickel is used as an interlayer between the copper conductor material and the corrosion-resistant layer (typically gold). This interlayer is required to block the diffusion of copper atoms into the gold plating and helps to increase the wear resistance of the gold plating. However, magnetic interlayers should be avoided in general in an FMR setup in order to reduce the magnetic field-dependent background signal (iv). This is particularly important in the CPW design, because the CPW, onto which the sample is mounted, needs to be placed in the magnetic field. If the CPW includes magnetic platings such as nickel near the center conductor, all measurements will therefore be obscured by the unwanted FMR signal of the nickel interlayer. In order to circumvent this issue, we used custom-

[1] Due to the small feature sizes, w of the fabricated structures deviates by up to 25 µm from the nominal design. For the experiments, we therefore visually inspect and select waveguides based on the production quality.

[2] Rogers Corp., Rogers, Connecticut, USA. Data sheet retrieved 2017-06-01 from https://www.rogerscorp.com/acs/products/39/RO3006-and-RO3010-Laminates.aspx

[3] Rogers Corp., Rogers, Connecticut, USA. Data sheet retrieved 2017-06-01 from http://www.rogerscorp.com/acs/products/54/ro4003c-laminates.aspx

made silver plated CPWs for which the issue of interdiffusion and wear are less critical and an interlayer can hence be omitted. The microwave cables were chosen by the same criteria and contain no magnetic materials (cf. Sec. A.2). The final non-magnetic microwave parts in the presented setup are the microwave connectors. Here, the use of V type connectors may be advised as for these types of connectors, the center conductor is used as the center pin in the connector and hence, no additional (potentially magnetic) parts need to be introduced. A change of the connector standard from SMK (2.92 mm) as in the current setup to V type (1.85 mm) additionally allows to extend the frequency range of the setup up to 65 GHz.

In Fig. 2.2 (d) the experimentally measured transmission parameter S_{21} of a CPW connected with two *Southwest Microwave SMK end launch connectors (1092-02A-5)* is displayed. The data show that the design goals of the microwave assembly are successfully achieved: The transmission (green line) is flat, i.e. it does not show any pronounced resonant features until 43.5 GHz; the total attenuation of the signal at 30 GHz is 3.3 dB. A conducting ferromagnetic sample (a 30 nm thick Py layer on P-silicon-on-insulator substrate) is placed directly on the CPW and S_{21} is measured again (orange line in Fig. 2.2 (d)). An increase in attenuation (11.5 dB at 30 GHz) and the appearance of sharp resonant features above 32 GHz are immediately obvious. Note that these inevitable loading effects are due to the change of Z_0 at the sample position. The resulting reflections reduce the total transmitted signal and cause standing waves in the transmission line. For non-conducting samples, the effects are typically less pronounced. They can be further reduced at the expense of the inductive coupling strength and thus also at the expense of the signal-to-noise ratio by placing a spacer in between sample and CPW. In an FMR experiment, two cables leading to the CPW also contribute to the attenuation. The complete transmission of the CPW with the permalloy sample, end launch and the two connecting cables at a magnetic field of 2 T is shown for reference in Fig. 2.5 (c). We use two 2 m long *Teledyne Storm Microwave PhaseMaster 160 cables* that are specified to nominally introduce 2.4 dB of attenuation per meter at 40 GHz. This type of cables was chosen as they feature a very high phase-stability against temperature changes and against mechanical movement which reduces a major source of noise in the setup [64].

For a temperature-dependent study of the ferromagnetic resonance spectra, the sample temperature needs to be controlled and stabilized for the course of the measurement. To achieve this temperature control, we place the sample with the CPW in the variable temperature inset of a helium

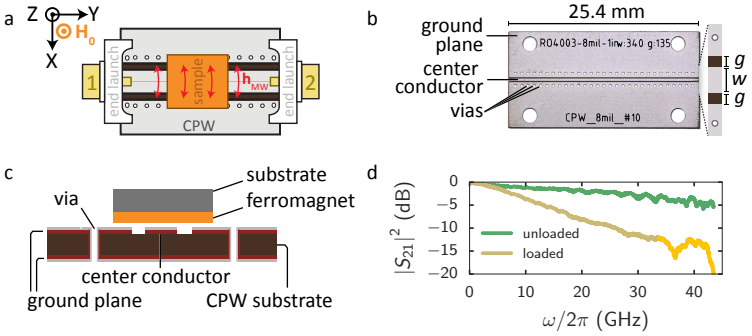

Figure 2.2: (a, c) Schematic top (a) and side (c) view of the CPW loaded with a 30 nm thick permalloy film (cf. Sec. 2.2). The static magnetic field H_0 is shown perpendicular to the plane. **(b)** Photograph of the coplanar waveguide (CPW) used in the setup (original size). The schematic zoom shows the w wide center conductor that is separated by two gaps of width g from the ground plane. **(d)** Microwave transmission characteristics of a 5 mil CPW without (blue) and loaded (orange) with a Py(30 nm)|P-silicon-on-insulator sample (cf. Sec. 2.2.4).

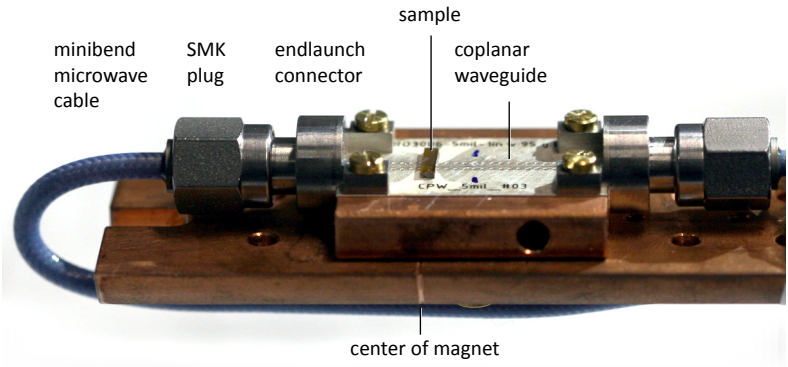

Figure 2.3: A typical sample (GdIG thin film, cf. Chap. 4) mounted on a CPW on a cooper holder. Two end launch connectors are mounted to the CPW that are in turn connected to minibend microwave cables. The assembly is shown mounted on the cooper lower part of a cryogenic dip stick which contains a temperature sensor and a resistive heater.

flow cryostat that is equipped with a superconducting magnet. The usual technical challenges of low-temperature physics using helium cryostats (vacuum tightness, reduction of heat conduction, thermal expansion) require a long (1.3 m) cryostat dip stick that supports the CPW in the center of the superconducting magnet. The bottom part of the dip stick with the mounted CPW and sample is shown in Fig. 2.3. Accurate placement in the center of magnet is crucial as typically, the exact knowledge of the magnetic field at the sample position directly limits the absolute accuracy of the measured g-factor (cf. 1 ppm lines in Fig. 2.4). In Chap. 3, we therefore use the room temperature value of the YIG g-factor for a self-consistent field calibration. During the doctorate two dip sticks for high frequency FMR were designed and extensively characterized in collaboration with a bachelor and a master student. In his bachelor's thesis [71], Felix Hartz assembled and characterized a versatile 4-port dip stick suitable for frequencies up to 26.5 GHz. With the gained practical experiences from this first setup, a dedicated bbFMR dip stick for the use up to around 40 GHz was designed and constructed. The detailed documentation of this later dip stick including the CPW holders, and DC and microwave cabling is presented in the appendix (Sec. A.2).

As mentioned in the introduction already, to measure the FMR response of the magnetic system, the loaded S_{21} needs to be measured as a function of the stimulus frequency ω and the static magnetic field H_0. Experimentally, there are two approaches to measuring these field-frequency maps of the complex-valued S_{21}: S_{21} can either be recorded as a function of ω at several fixed magnetic field strengths H_0 or as a function of H_0 for several fixed microwave frequencies ω. Limitations of the setup, such as a superconducting magnet which ramps comparatively slowly, and the materials FMR dispersion determines if the former or the later measurement method is used. In our variable temperature setup (Fig. 2.4), the static magnetic field is generated by a superconducting magnet while in our room temperature setup, a water-cooled electromagnet is employed. In both cases, the microwave magnetic field is excited using a vector network analyzer (VNA), which applies a microwave stimulus is applied to port 1 of the CPW assembly. When the resonance condition is fulfilled, the magnetization is excited to precess coherently and the magnetization is driven into a steady state resonant precession where excitation and damping balance each other. The induction voltage from the precessing magnetization in combination with the purely transmitted microwave signal is then measured phase sensitively as the complex scattering parameter $S_{21}^{\mathrm{raw}}(\omega)$ at port 2 of the VNA.

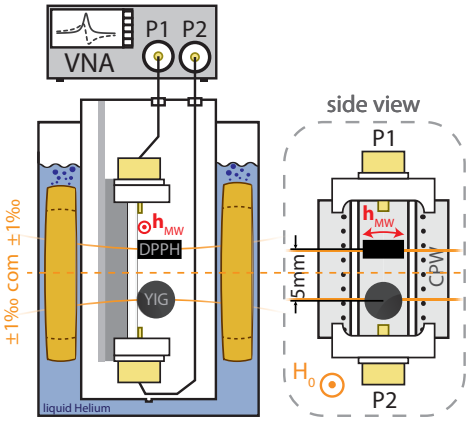

Figure 2.4: Schematic depiction of the dip stick with the CPW assembly (cf. Fig. 2.3) inserted into a helium flow cryostat. The CPW is connected via hermetic feedthroughs to a VNA. A magnetic bias field can be applied by (multiple) superconducting coils with a specified homogeneity as shown by the 1 ppm lines. The sample is ideally placed in the center of magnet (com). The CPW is loaded with a YIG sphere and a DPPH marker as a field reference. Figure adapted from Ref. [MF6].

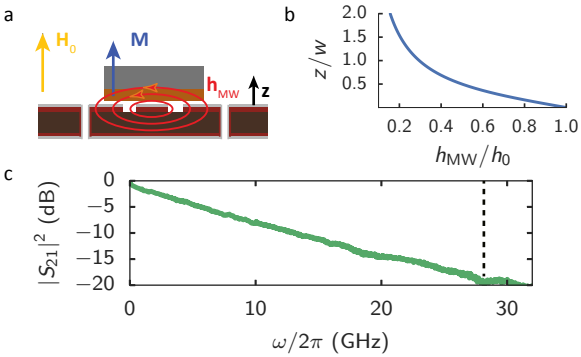

Figure 2.5: (a) Schematic side view of the CPW loaded with a thin film sample, magnetization $\mathbf{M}$, static magnetic field H_0 and microwave magnetic field $\mathbf{h}_{\mathrm{MW}}$. **(b)** Calculated $h_{\mathrm{MW}} = |\mathbf{h}_{\mathrm{MW}}|$ as a function of the distance z to the CPW in the middle of the center conductor of width w based on Ref. [72]. **(c)** Microwave transmission of the CPW assembly including cables and connectors and the permalloy sample from Sec. 2.2 at $\mu_0 H_0 = 2\,\mathrm{T}$. The FMR signal is expected at the indicated position (dashed line) of $\omega_{\mathrm{res}}/2\pi \approx 28\,\mathrm{GHz}$. The strong frequency-dependent background, however, masks the signal almost completely.

We use two VNAs in the following, a Keysight (Agilent) N5242A PNA-X which covers the frequency band from 10 MHz to 26.5 GHz and a Keysight N5244A PNA which reaches frequencies of 43.5 GHz. The later VNA was kindly provided by Martin S. Brandt from the Walter Schottky Institut of the Technical University of Munich. In order to separate the FMR response of the magnetic sample from the background signal and to model the FMR response, various methods can be employed. In the following section the background separation methods and the modeling of the FMR signal are described in more detail.

2.2 Background removal and data analysis

In this section, we discuss the analysis of the field and frequency-dependent microwave transmission parameter S_{21} that contains the inductive signal of the FMR excitation. We first outline how the signal S_{21} that is recorded at the VNA can be parametrized and how the FMR signal can be modeled as a function of H_0 and ω. We then briefly outline and compare two conventional methods for separating background and FMR signal that are used in the following chapters. We demonstrate the methods using post-processing on the same full field-frequency map of an FMR measurement of a permalloy film. The permalloy thin film that we use was deposited to a thickness of $t = 30\,\mathrm{nm}$ using electron-beam deposition on a phosphorus-doped silicon on insulator substrate by Ryo Ohshima/Masashi Shiraishi from the Department of Electronic Science and Engineering of the Kyoto University, Japan. It's lateral dimensions are $10\,\mathrm{mm} \times 10\,\mathrm{mm}$. We then focus on a novel background removal method based on the derivative of the scattering parameter [MF5] that allows to analyze bbFMR data as a function of ω instead of H_0. Finally, we perform the quantitative analysis of bbFMR spectroscopy data of the permalloy and a YIG thin film and critically compare the results of the field and the frequency space model.

2.2.1 Modeling the FMR response

Typically, FMR is not evaluated by modeling the complete field-frequency map of S_{21} but instead, only a narrow region of interest (ROI) is fitted with the high frequency susceptibility as a function of either H_0 or ω. The VNA records S_{21} of the setup as $S_{21} = (V_\mathrm{o}/V_\mathrm{i}) \cdot e^{i\phi}$ with the input voltage V_i at port 1, the measured voltage V_o at port 2 and a phase factor ϕ, the so-called electrical length of the setup.

In a CPW based bbFMR experiment, the precessing magnetization induces a voltage in the center conductor of the CPW that is proportional to the high-frequency susceptibility χ [64, 70]:

$$\begin{aligned} V_\mathrm{inductive} &= -i\omega\tilde{A}e^{i\phi}V_\mathrm{o}\chi(\omega, H_0) \\ &= -i\omega A e^{i\phi}V_\mathrm{o}\tilde{\chi}(\omega, H_0) \end{aligned} \tag{2.1}$$

Here, $\tilde{A}$ is a real-valued scaling parameters that is proportional to the strength of the inductive coupling between the sample and the CPW which

is given by geometric factors. In the second line, we eliminate the magnetization M_0 from χ (cf. Eq. (1.10) and Eq. (1.16)) and absorb it into A instead, giving the magnetization normalized susceptibility $\tilde{\chi} = \chi/M_0$. The amplitude A of the FMR signal that we extract in the later fits is hence proportional to the magnetization M_0 of the sample. The dependence of $V_{\text{inductive}}$ on V_o can be understood qualitatively as V_o is proportional to the microwave magnetic field which results in a larger precession cone angle and hence a larger induced voltage. The proportionality to the frequency stems from the fact that the precession frequency of the magnetization directly determines the time derivative of the flux and hence the induced voltage. A detailed derivation of the relationship of $V_{\text{inductive}}$ with the geometric parameters and the properties of the system can be found in Ref. [64]. A quantitative analysis of the frequency dependence of the amplitude A reveals the magnetization of the sample under investigation and has for example also been used to quantify the spin orbit torque in ferromagnet-normal metal bilayers [73]. When the whole setup is taken into account, $V_{\text{inductive}}$ is obscured by a real frequency-dependent background $V_\text{o}^{\text{BG}}(\omega)$ that depends on losses and the phase shift $\phi(\omega)$ due to the electrical length of the microwave leads and the CPW itself. S_{21} is then given by the linear superposition of the $V_{\text{inductive}}$ and $V_\text{o}^{\text{BG}}(\omega)$:

$$S_{21} = \frac{-i\omega A V_\text{o} \tilde{\chi}(\omega, H_0) + V_\text{o}^{\text{BG}}(\omega)}{V_\text{i}} e^{i\phi}. \tag{2.2}$$

The raw S_{21} data of the complete CPW assembly with sample is shown in Fig. 2.5 (c) for $\mu_0 H_0 = 2\,\text{T}$. At this value of H_0, the FMR signal of the permalloy thin film is expected around 28 GHz (dashed line). Without employing a suitable background removal method, however, the FMR signal is not visible clearly due to the frequency dependence of S_{21} of the CPW assembly alone.

Evaluation of $S_{21}(H_0)\,|_{\omega=\text{const}}$

To circumvent this issue, S_{21} can be recorded at fixed ω as a function of H_0. The complex-valued field-dependent background signal $V_\text{o}^{\text{BG}}(H_0)$ is then taken into account in the field-space analysis model. In a sufficiently small ROI, $V_\text{o}^{\text{BG}}(H_0)$ can be approximated as a linear function of H_0, parametrized by the complex fit parameters B and C. The absolute phase ϕ of $V_{\text{inductive}}$ is, however, still undetermined and needs to be included as an additional

free fit parameter. Therefore, the full fit model for FMR in the field domain is given by [65]:

$$S_{21}(H_0)\,|_{\omega} = -i\omega A e^{i\phi}\tilde{\chi}(\omega, H_0) + B + C \cdot H_0. \tag{2.3}$$

Furthermore, especially for low fields, the equilibrium magnetization direction may change with the external magnetic field magnitude and hence, a different lineshape results. In the high field case, when the H_0 is larger than the anisotropy fields in the sample, the effects can be neglected. If this is not given, the theoretical description of the magnetization dynamics is more complicated as the orientation of **M** first needs to be calculated by determining the minimum and the derivatives of the free energy need to be recalculated for each magnetic field step. Finally, when the setup involves a superconducting magnet, the slow ramp-rate of the magnet current is a major technical obstacle for field-swept bbFMR measurements.

Evaluation of $S_{21}(\omega)\,|_{H_0=\text{const}}$

If an analysis in field-space is not practical due to the issues mentioned above, an analysis in frequency space must be performed. In this case, the frequency-dependent background V_{BG} needs to be removed from S_{21} by another approach. In principle, a microwave calibration can efficiently eliminate V_{BG} and furthermore allows to provide well determined fixed microwave power at the sample location. A calibration that includes the complete microwave network up to the sample position, covering in particular the connectors at the CPW, is, however, technically very challenging. Furthermore, such a calibration is typically not sufficient as the background is typically field and temperature-dependent. Hence, a background contribution typically remains which needs to be taken into account in the modeling analogous to the fixed frequency case, giving the full fit model in the frequency domain:

$$S_{21}(\omega)\,|_{H_0} = -i\omega A e^{i\phi}\tilde{\chi}(\omega, H_0) + B + C \cdot \omega \tag{2.4}$$

Again, B and C describe a linearly frequency-dependent background and A is the real-valued scaling parameter. An additional technical obstacle of a microwave calibration is that it requires manually disconnecting and reconnecting the CPW assembly which makes the procedure time consuming and reduces the reproducibility between measurements. Calibrating the microwave network is therefore usually avoided and a method for separating

the signal of interest from the background as described below is employed instead.

Extraction of magnetic properties (γ, M_s)

The fitting methods at constant field (or frequency) described above are overdetermined because the fit parameters γ (gyromagnetic ratio) and $M_0 = M_s$ (saturation magnetization for ferromagnets) are completely correlated with $\tilde{A}$. Only by analyzing multiple cuts at different fields (frequencies), this ambiguity is lifted. Nembach et al. [65] showed that taking γ constant with an arbitrary value does not interfere with the fit of cuts at constant field (frequency). M_s is eliminated as free fit parameter and absorbed in A instead by fitting the magnetization normalized susceptibility $\tilde{\chi}$. Therefore, the only free parameters of a fit at constant field (frequency) are the resonance frequency ω_{res}, the full width at half maximum (FWHM) linewidth $\Delta\omega$, and the complex-valued amplitude parameter A. The magnetic properties γ and M_s of the material are determined in a second step, in which ω_{res} is fitted to the appropriate dispersion relation. The alternative to this approach is a simultaneous 2D fit of the field-frequency map which is very challenging as it requires an excellent initial parameter guess and an appropriate model for the contribution of the setup in order to succeed. We will therefore not use a 2D fit but the former procedure according to Nembach et al. [65] in the following chapters.

2.2.2 Fixed field reference

As mentioned before, the raw transmission parameter $S_{21}^{raw}(H_0, \omega)$, contains the inevitable frequency dependence S_{21}^{BG} of the setup that typically obscures the comparably small signal of interest from magnetic resonance and needs to be removed. The most simple method is to divide $S_{21}^{raw}(H_0, \omega)$ at each fixed H_0 by a slice $S_{21}^{BG} = S_{21}^{raw}(H_0 = H_{BG}, \omega)$. This removes all effects originating from the frequency-dependent absolute value of the transmission of the setup, and removes the strong linear phase dependence of S_{21}^{raw} with the microwave frequency stemming from the electrical length. H_{BG} is ideally chosen so that S_{21}^{BG} does not contain any FMR signal of interest or the inverse of the signal will be imprinted on all other slices. This background subtraction method is shown for reference in Fig. 2.6 for the field-frequency map of S_{21} of the 30 nm thick permalloy film using $S_{21}^{BG} = S_{21}^{raw}(H_0 = 1.8\,T, \omega)$ as the background reference. The magnetic

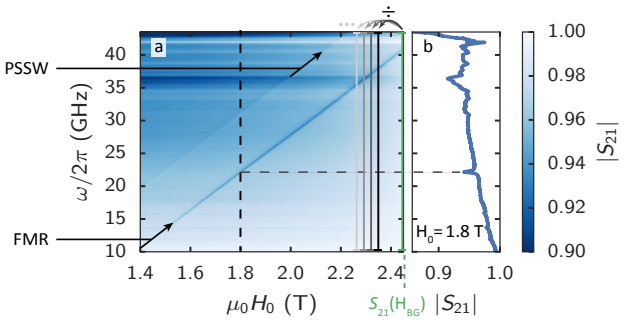

Figure 2.6: Fixed reference background removal. The raw data $S_{21}^{\mathrm{raw}}(H_0,\omega)$ at each $H_0 = H_0^{\mathrm{eval}}$ (illustrated by the black and gray lines) is divided by $S_{21}^{\mathrm{raw}}(H_0 = H_{\mathrm{BG}},\omega)$ with $H_{\mathrm{BG}} \gg H_0^{\mathrm{eval}}$ (green) to yield $S_{21} = S_{21}^{\mathrm{raw}}(H_0,\omega)/S_{21}^{\mathrm{BG}}$. **(b)** $|S_{21}|$ at $\mu_0 H_0 = 1.8\,\mathrm{T}$. Note the faintly visible higher order PSSW at higher frequency than the FMR.

absorption spectrum of the permalloy film is faithfully reproduced and both, the fundamental FMR mode and a higher order perpendicular standing spin wave (PSSW) mode can be clearly identified. For the rather thick permalloy sample used here as an example, the signal-to-noise ratio is sufficient to allow a quantitative analysis. However, the main drawback of the method already shows in Fig. 2.6: The magnetic field-dependent background is not removed effectively. Especially, when the observed frequency range is broad (1 GHz to 43 GHz in the example), H_{BG} needs to be large and therefore, a magnetic field-dependent background shows in the measurement and complicates the identification of modes. The FMR is therefore, if possible, often analyzed in field space at constant microwave frequency as described above. We will perform this conventional quantitative analysis of FMR for the permalloy sample below (cf. Sec. 2.2.5). The here described method is, however, still useful to gain an overview of the resonance modes of the material and their dispersion relation.

2.2.3 Moving field reference method

In the case of a significant magnetic field-dependent background signal and when the dispersion relation of a magnetic resonance mode is well known, a different background removal method is preferable. In this method, the frequency-dependent background is eliminated as follows: The expected

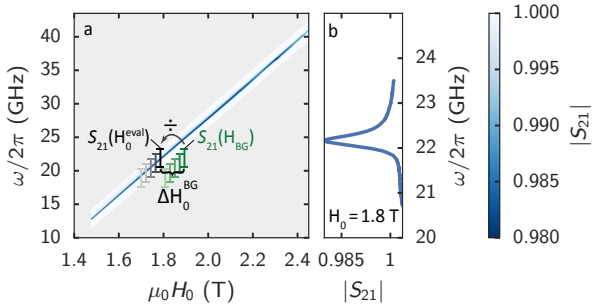

Figure 2.7: Moving reference background removal. The raw data $S_{21}^{\text{raw}}(H_0, \omega)$ at each $H_0 = H_0^{\text{eval}}$ (illustrated as black and gray lines) is divided by $S_{21}(H_0 = H_{\text{BG}}(\omega), \omega)$ (green) with $H_{\text{BG}}(\omega) = H_0^{\text{eval}} + \Delta H_0^{\text{BG}}$ to yield S_{21}. **(b)** $|S_{21}|$ at $H_0 = 1.8\,\text{T}$. Note that to avoid artifacts from the background removal, only a 2.5 GHz frequency window is shown and hence, the higher order PSSW is not visible.

resonance frequency for a given field H_0^{eval} is calculated according to the dispersion relation. The frequency range is set to a narrow band that just includes the signal of interest. A static external magnetic field $H_{\text{BG}} = H_0^{\text{eval}} + \Delta H_0^{\text{BG}}$ sufficiently large so that no resonances are expected in this microwave frequency band is applied and the transmission at this field is recorded as the background reference $S_{21}^{\text{BG}} = S_{21}(H_0 = H_{\text{BG}}(\omega), \omega)$. Then, H_0 is set to H_0^{eval}, the field at which we expect resonances of the magnetic material in the given frequency band, and the transmission $S_{21}^{\text{raw}}(H_{\text{eval}}, \omega)$ is recorded. We finally calculate

$$S_{21} = S_{21}^{\text{raw}} / S_{21}^{\text{BG}}.$$

This procedure is repeated for each $H_0 = H_0^{\text{eval}}$ for which resonance frequency and lineshape is to be extracted.

For illustration purposes, the method is applied to the same raw data set of the permalloy film as used for the fixed field reference background removal and displayed in Fig. 2.7. In a real experiment, only the data shown in Fig. 2.7 need to be recorded which reduces the size of the acquired raw data in comparison to recording the complete H_0 vs. ω map of S_{21} and therefore allows for a much quicker measurement. As before, the frequency-dependent transmission of the setup is corrected effectively. Furthermore, the magnetic field-dependent background has a smaller effect as compared to the fixed field reference background removal method

because the background signal is recorded at a magnetic field very close to H_0. This can be seen from the fact that the off-resonant transmission is reliably corrected to a value very close to 1 for all values of H_0.[4,5] The method is very well suited for the characterization of materials for which all magnetic phases and resonance modes are known. It is, however, not applicable when the dispersion of any resonance mode is unknown. Note that for the data of the permalloy thin film shown in Fig. 2.7, it is not possible to analyze the higher order PSSW at the same time due to their large frequency difference of 10 GHz. Modeling the data is performed with Eq. (2.4). Typically, the quality of the background removal is sufficient, so that no background needs to be taken into account in the model, i.e. $B = C = 0$. We use this method in Chap. 3 for the temperature-dependent damping study of an yttrium iron garnet single crystalline sphere.

2.2.4 Background removal using a difference quotient

The background removal method which we now discuss has been developed as a part of this thesis in collaboration with Mathias Weiler and is published as Ref. [MF5]. The text of this subsection is, in part, adapted from this reference. The method, which we name *derivative divide* or $\mathrm{d_D}$, is based on computing the numerical derivative of the broadband spectroscopy data with respect to the magnetic field and enables direct access to the high frequency magnetic susceptibility as a function of frequency. It furthermore does not require prior knowledge of the dispersion relation of the FMR modes and allows to efficiently suppress the background signal over the whole frequency and field range.

In the experiment, traces of $S_{21}(\omega)|_{H_0}$ (Eq. (2.2)) are measured for a series of fixed magnetic field magnitudes H_0. The traces need to be recorded at the same values of ω for the proposed background removal method. The

[4] In the bbfmr python package (cf. Sec. A.1), this method of background subtraction is transparently implemented as the `Measurement` class `VNAReferencedMeasurement` and can be applied to full maps of $S_{21}(H_0, f)$ using the post-processing operation `referenced_fmr()`.

[5] The text of the preceding two paragraphs is adapted from H. Maier-Flaig et al., "Temperature-dependent magnetic damping of yttrium iron garnet spheres", Physical Review B **95**, 214423 (2017).

central differences of S_{21} with respect to H_0 using a finite step width $\Delta_{\mathrm{mod}}H$ can then be calculated and the result is divided by the central value of S_{21}:

$$\begin{aligned} \mathrm{d_D}S_{21} &= \frac{S_{21}(\omega, H_0+\Delta_{\mathrm{mod}}H) - S_{21}(\omega, H_0-\Delta_{\mathrm{mod}}H)}{S_{21}(\omega, H_0)\,\Delta_{\mathrm{mod}}H} \\ &= -i\omega A \frac{\tilde{\chi}(\omega, H_0+\Delta_{\mathrm{mod}}H) - \tilde{\chi}(\omega, H_0-\Delta_{\mathrm{mod}}H)}{\Delta_{\mathrm{mod}}H} + \mathscr{O}\left(A^2\right) \\ &\approx -i\omega A \frac{\mathrm{d}\tilde{\chi}}{\mathrm{d}H_0} = -i\omega A \frac{\mathrm{d}\tilde{\chi}}{\mathrm{d}\omega}\frac{\partial\omega}{\partial H_0} = -i\omega A' \frac{\mathrm{d}\tilde{\chi}}{\mathrm{d}\omega} \end{aligned} \tag{2.5}$$

To second order in the signal amplitude A, $\mathrm{d_D}S_{21}$ is proportional to the derivative of the susceptibility with respect to the external field. For small field steps, $\frac{\mathrm{d}\chi}{\mathrm{d}H}$ is proportional to the frequency derivative $\frac{\mathrm{d}\tilde{\chi}}{\mathrm{d}\omega}$ as χ varies smoothly with field and frequency. The partial derivative $\frac{\partial\omega}{\partial H}$ therefore contributes a real-valued factor only which can be absorbed in $A \to A'$.

Note most importantly that $V_{\mathrm{o}}^{\mathrm{BG}}$ and ϕ drop out in Eq. (2.5). Hence, $\mathrm{d_D}$ corrects for the losses and the electrical length of the setup, without the need for any calibration. For a finite magnetic field step width $\Delta_{\mathrm{mod}}H$, features in the data that vary much faster or slower with H_0 than $\Delta_{\mathrm{mod}}H$ get suppressed. This is a further major advantage of *derivative divide* as it allows to efficiently suppress a background signal that varies much faster or slower than the expected FMR linewidth. In this respect, *derivative divide* mimics a field modulation technique as commonly employed in fixed frequency FMR without requiring any additions to the setup. However, one therefore also needs to take into account that the FMR lineshape is distorted when $\Delta_{\mathrm{mod}}H$ is on the order of or larger than the FMR linewidth. This can be accounted for by numerically calculating and fitting the central difference quotient instead of $\frac{\mathrm{d}\tilde{\chi}}{\mathrm{d}\omega}$ in Eq. (2.5):

$$\mathrm{d_D}S_{21} = -i\omega A' \frac{\tilde{\chi}(\omega+\Delta_{\mathrm{mod}}\omega) - \tilde{\chi}(\omega-\Delta_{\mathrm{mod}}\omega)}{2\Delta_{\mathrm{mod}}\omega}. \tag{2.6}$$

This fit formula then contains the known modulation amplitude $\Delta_{\mathrm{mod}}\omega = \Delta_{\mathrm{mod}}H\frac{\partial\omega}{\partial H_0} \approx \Delta_{\mathrm{mod}}H\gamma\mu_0$. Note that *derivative divide* is a post-processing technique of field-frequency maps of S_{21}. In contrast to an experimental modulation technique, the modulation amplitude can therefore be chosen freely to an integer multiple of the experimental field step width. This allows to highlight features of a certain linewidth in post-processing. Furthermore, if the signal-to-noise ratio is the major obstacle, the data processed with different modulation amplitudes (e.g. 1 mT, 2 mT and 3 mT) can be averaged.

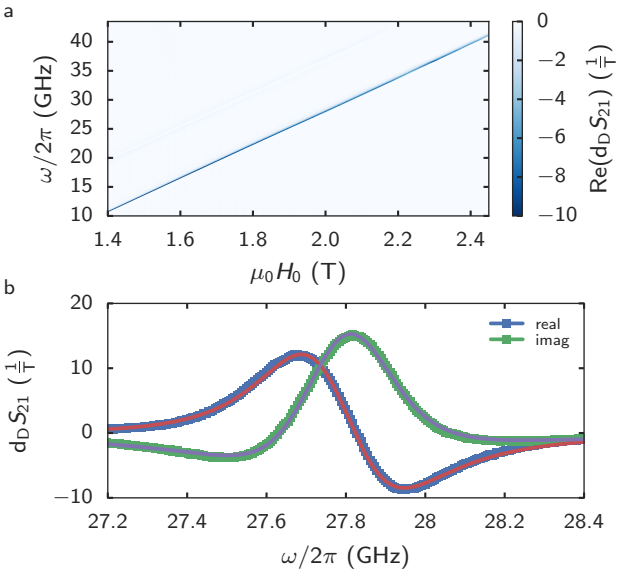

Figure 2.8: *Derivative divide.* $\mathrm{d_D}S_{21}(H_0)_\omega$ at each $H_0 = H_0^{\mathrm{eval}}$ is given by the difference of $S_{21}(H_{\mathrm{BG}})|_\omega$ with $H_{\mathrm{BG}} = H_0^{\mathrm{eval}} \pm \Delta_{\mathrm{mod}}H$ divided by $\Delta_{\mathrm{mod}}H$ and $S_{21}\left(H_0^{\mathrm{eval}}\right)|_\omega$. **(a)** $\mathrm{d_D}S_{21}$ with $\mu_0\Delta_{\mathrm{mod}}H = 2.4\,\mathrm{mT}$ as function of field and frequency. **(b)** Cut at $\mu_0 H_0 = 2\,\mathrm{T}$. The solid lines are a fit to $\mathrm{d_D}S_{21}\cdot e^{i\phi}$ with $\mathrm{d_D}S_{21}$ from Eq. (2.6) and fixed $\mu_0\Delta_{\mathrm{mod}}H = 2.4\,\mathrm{mT}$.

This type of averaging visually cleans up the typical colorplots (Fig. 2.8 (a)) that can be used for a qualitative analysis of the spectrum. The averaging can also be taken into account easily in the fit model.[6]

2.2.5 Quantiative analysis in field- and frequency-space – Permalloy sample

The following analysis is published as Ref. [MF5] and the text and figures of this section are adapted from this reference. We now apply *derivative divide*

[6] In the bbfmr python package (cf. Sec. A.1), this method of background subtraction is implemented as post-processing operation `derivative_divdie` and fitting models for the analysis of FMR spectra using the derivative and the difference quotient of $\tilde{\chi}$ are available.

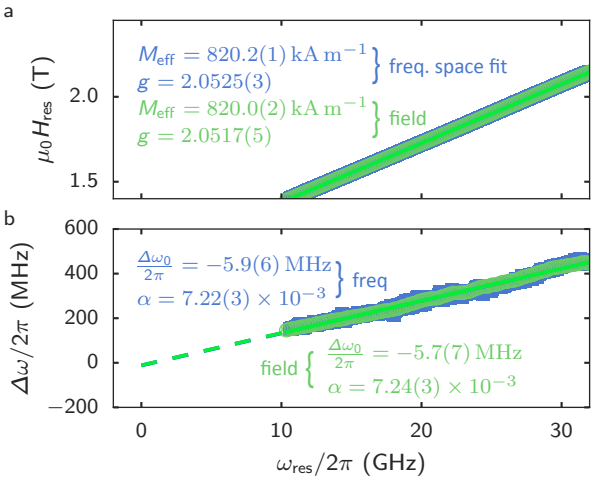

Figure 2.9: Results of fits of $\mathrm{d_D}S_{21}$ keeping H_0 constant [cf. Fig. 2.8 (b), blue] and of a fit of S_{21} to Eq. (2.3) keeping ω constant [cf. Fig. 2.10, green]. **(a)** Field and frequency of resonance for the two methods (data points). Model using Eq. (1.15) (solid lines). **(b)** Frequency FWHM linewidth $\Delta\omega$ extracted from both methods. For the green data points, the field linewidth ΔH is converted to a frequency linewidth via $\Delta\omega = \gamma\mu_0\Delta H$. Figure adapted from Ref. [MF5].

to the data of the permalloy film and model the results as described above. Note that with *derivative divide*, the slowly varying background signal and any offsets are heavily suppressed. Hence, automated extraction of ω_{res} is straightforward. We fit cuts of $\mathrm{d_D}S_{21}$ at fixed H_0 to Eq. (2.6) multiplied with a phase factor $e^{i\psi}$. The distortion of the line due to *derivative divide* is taken into account by setting $\mu_0\Delta_{\mathrm{mod}}H = 2.4\,\mathrm{mT}$ corresponding to $\Delta_{\mathrm{mod}}\omega = 91\,\mathrm{MHz}$ for the fit. Inductively or capacitively generated currents flowing in the conducting permalloy film give rise to a finite phase shift ψ [74]. Note that for insulating ferromagnets no additional phase shift is expected and $\psi = 0$. An example of the usual excellent agreement of fit and data is shown in Fig. 2.8 (b). The resulting parameters resonance frequency ω_{res} and linewidth $\Delta\omega$ are displayed in Fig. 2.9 (green data points). Modeling $\omega_{\mathrm{res}}(H_0)$ with the Kittel equation, Eq. (1.15), for a thin ferromagnetic film magnetized perpendicular to its plane (solid lines in Fig. 2.9 (a)) gives a gyromagnetic ratio of $\gamma = 28.727(4)\,\mathrm{GHz\,T^{-1}}$ (corresponding to $g = \gamma\frac{\hbar}{\mu_{\mathrm{B}}} = 2.0525(2)$) and a saturation magnetization of $M_{\mathrm{s}} = 820.1(1)\,\mathrm{kA\,m^{-1}}$. Both fit parameters are in very good agreement with the literature [75]. The linewidth can be modeled accurately with the Gilbert-like damping model from Eq. (1.6) (solid lines in Fig. 2.9 (b)). The resulting Gilbert damping parameter $\alpha = 0.00722(3)$ is typical for permalloy thin films [75]. The inhomogeneous linewidth $\Delta\omega_0/2\pi = -5.9(6)\,\mathrm{MHz}$ is very close to zero indicating excellent homogeneity of our films. The very small negative value can be explained by uncertainties in the field readout or deviations from linearity of $\Delta\omega(f)$.

Finally, in order to confirm that *derivative divide* does not distort $\Delta\omega$ or ω_{res}, we perform the conventional procedure of fitting fixed frequency cuts of S_{21} using Eq. (2.2). Again, an exemplary fit is shown in Fig. 2.10 (solid lines) which shows good agreement with the data. The fit results are shown in Fig. 2.9 (blue data points). The extracted parameters (ω_{res} and $\Delta\omega$) result in material parameters of $g = 2.0517(5), M_{\mathrm{s}} = 820.0(2)\,\mathrm{kA\,m^{-1}}, \alpha = 0.00724(3)$ and $\Delta\omega_0/2\pi = -5.7(7)\,\mathrm{MHz}$. The material parameter extracted using the two methods are in excellent agreement which shows that *derivative divide* allows to faithfully determine $\Delta\omega$ and ω_{res} even when $\Delta_{\mathrm{mod}}\omega$ is not small compared to $\Delta\omega$.

Note that the complete set of raw data and the analysis programs are available at Ref. 76 and that a reference implementation of *derivative divide* and automated fitting models for S_{21} are freely available (Sec. A.1).

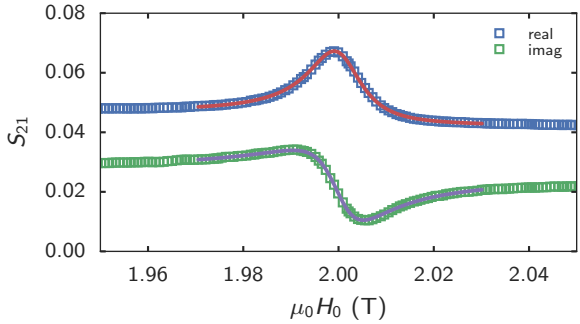

Figure 2.10: (a) Cut of S_{21} taken at $f = 27.8\,\mathrm{GHz}$. A constant offset has been subtracted for visual clarity. The solid lines are a fit to Eq. (2.3).

2.2.6 Quantiative analysis in field- and frequency-space – YIG sample

In order to confirm the assumption that the phase shift of the inductive signal is caused by currents induced in a conducting sample we now perform a similar analysis of bbFMR measurements on YIG thin film. We choose YIG as it represents a well studied prototypical example of an insulating ferromagnet. In an insulator such as YIG, no parasitic currents can be induced and hence, in the analysis an additional phase factor as in the previous section should not be required. The YIG film (WMI designation `YIG245`) has been grown on gadolinium gallium garnet substrate (GGG) to a thickness of 45 nm by Stephan Geprägs. The measurements have been conducted in collaboration with Lukas Liensberger. We record a field-frequency map of S_{21} and analyze the data using derivative divide and in field space as in the previous chapter. Note that the absolute signal and hence the signal-to-noise-ratio is lower than in the measurement of the permalloy sample. This is due to the lower saturation magnetization of YIG as compared to permalloy and fluctuations in the electromagnets field strength caused by the quick ramping of the field. We therefore include the small frequency-dependent background in the model as a linear complex-valued trend parametrized with B and C

$$\mathrm{d_D} S_{21} = \text{Eq. (2.6)} + B + C \cdot \omega. \tag{2.7}$$

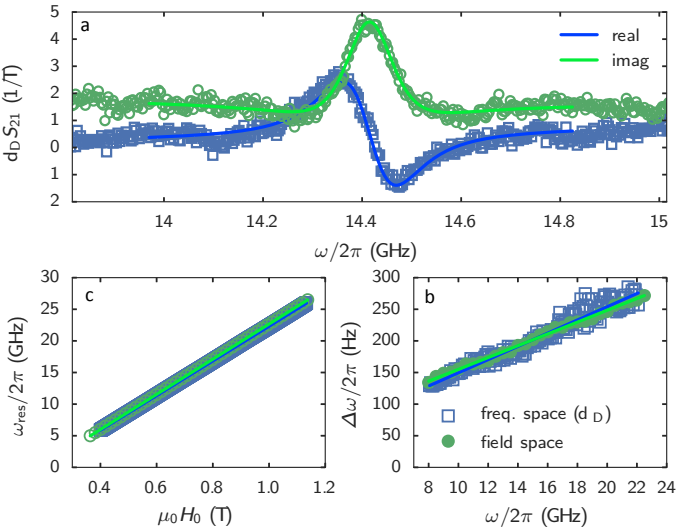

Figure 2.11: Broadband FMR on a YIG thin film sample with a thickness of 45 nm magnetized out of plane. **(a)** Slice of the complex-valued data at $H_0 = 715\,\mathrm{mT}$ and fit to Eq. (2.7). **(b)** ω_{res} vs. H_0 from fits as in (a) (blue squares) and from fits of the data to a field space model (green circles). The solid lines are the fit to the Kittel equation Eq. (1.15). **(c)** $\Delta\omega$ vs. ω_{res} from both approaches. The solid lines are the fit to a Gilbert-like damping model Eq. (1.6).

The fits to this model without the additional phase factor as shown as an example in Fig. 2.11 (a) match the data very well. We find that for the analysis of the FMR measurement data of an insulating ferromagnet processed with derivative divide an additional phase factor is not required. This indicates that the phase shift of the signal observed for the permalloy sample indeed originates from induced currents in the conducting ferromagnet permalloy.

The fit parameters ω_{res} and $\Delta\omega$ are shown in Fig. 2.11 (b) and (c) as blue squares and match qualitatively very well with the field space analysis with the model of Eq. (2.3) (green circles). As for the permalloy sample, the results of the two methods here are also in very good qualitative and quantitative agreement: The dispersion can be accurately modeled with the Kittel equation (Eq. (1.15)) and the linewidth follows a linear, Gilbert-like, trend (Eq. (1.6)). For the frequency space (derivative divide) analysis (solid blue line in Fig. 2.11) the resulting parameters are $M_{\mathrm{eff}} = 148.1\,\mathrm{kA\,m^{-1}}$, $g = 1.959$, $\alpha = 5.22(8) \times 10^{-3}$ and $\Delta\omega/2\pi = 23(1)\,\mathrm{MHz}$. For the field space analysis we extract $M_{\mathrm{eff}} = 146.8\,\mathrm{kA\,m^{-1}}$, $g = 1.985$, $\alpha = 4.67(6) \times 10^{-3}$ and $\Delta\omega/2\pi = 31(1)\,\mathrm{MHz}$. These values are in reasonable agreement with values reported for YIG in the literature [77]. Note that the values do not match within the given standard error (for the dispersion fits, the standard error is smaller than the given significant digits). This may be due to the fact that for high frequencies a frequency space analysis is more susceptible to imperfect transmission characteristics of the setup than a field space analysis. This is indicated by the larger scatter in Fig. 2.11 (c) at high frequencies (17-22 GHz) and can be explained by the fact that the density of states to which the magnonic excitation can relax varies for a cut of S_{21} at constant H_0 (frequency space analysis) but is constant for a cut of S_{21} at constant ω. Hence, the data may show a small deviation from the ideal model in frequency space giving rise to slightly different fit parameters. Furthermore, the point density in the field and frequency analysis is not constant and hence, deviations from the theoretically expected dispersion relation or deviations from the linear frequency dependence of $\Delta\omega$ may give rise to different extracted fit parameters too. This, however, is not an intrinsic problem of the data analysis method using *derivative divide* and as mentioned before, overall, the agreement between the two methods is good. We conclude that also for the insulating ferrimagnet YIG, the analysis using *derivative divide* returns values that are in reasonable agreement with a field space analysis.

2.2.7 Comparison of the methods

In this section, we summarized the most common methods for separating the FMR signal from a magnetic field and frequency-dependent background. The FMR signal can be analyzed quantitatively using the equations given in Sec. 2.2.1 and Sec. 2.2.4 as a function of H_0 or ω. The choice of the background separation method and whether to analyze the FMR as a function of H_0 or ω, depends on the experimental setup, the research goal and the knowledge of the FMR dispersion relation of the material.

Compared to the other background removal methods, the fixed field reference method (Sec. 2.2.2) is of little relevance for a quantitative analysis as it does not suppress a magnetic field-dependent background signal effectively. It, however, allows to very easily gain a first overview over the resonance modes that show in a field-frequency map of S_{21}. Due to its simplicity, it is probably the most-used method in the literature. When the dispersion relation of the FMR modes of the material under investigation is already know, recording a full field-frequency map of S_{21} with a high point density along both axes is not necessary. Instead, S_{21} can be recorded as a function of H_0 at several fixed ω and can be modeled with Eq. (2.3) which includes the parameters B and C for the magnetic field-dependent background. This analysis holds the advantage that the frequency dependence of S_{21} is already absorbed in B and C. Furthermore, this method typically offers the best signal-to-noise ratio, as VNAs typically feature a better noise floor in their continuous wave mode (exciting and measuring at a fixed frequency) and, as discussed in the previous section, the photon density of states stays constant during one measurement.[7] However, magnetization dynamics of materials with multiple magnetic phases, for example, can only be done in the frequency-domain, as changing the external magnetic field will inevitably also modify the magnetic configuration. Therefore, experiments at fixed magnetic field while sweeping the microwave frequency are highly desirable. In this case, the frequency dependence of the setup needs to be accounted for in a quantitative analysis which brings the later two background separation methods into play. Again, when the dispersion of the material is already known, a full field-frequency map of S_{21} is not required. The frequency dependence of S_{21} caused by the setup then needs to be removed. The moving field background removal method (Sec. 2.2.3)

[7] A detailed, quantitative, discussion of the noise characteristics of the setup including a comparison of the actual typical measurement times is given in the master's thesis of Philip Louis [64].

achieves this and, at the same time, suppresses a magnetic field-dependent background efficiently. However, when the dispersions of the FMR modes are not known a-priori or when the resonances are stretched over a wide field or frequency range, the moving field reference method can not be used as it can remove the background in a narrow frequency band only. In this case, *derivative divide* (Sec. 2.2.4) is the method of choice as it does not require any knowledge of the FMR dispersion and removes both, the field and frequency-dependent background, efficiently. The method has been applied already to investigate FMR in helical and conical magnetic phases of the chiral magnetic insulator Cu_2OSeO_3 [78]. We would like to stress that *derivative divide* is not restricted to the particular case of materials with complex magnetic phases but is suited for all of the above mentioned examples. Its limitation lies in the fact that for *derivative divide* the field steps need to be smaller than the FMR linewidth which may lead to long measurement times or large measurement files.

CHAPTER 3

MAGNETIC PROPERTIES OF YTTRIUM IRON GARNET SPHERES

In the previous chapters, we introduced ferromagnetic resonance and described the various analysis methods in detail. To demonstrate the technique and to establish the reliability of the background separation and the (newly developed and implemented) analysis methods, we performed FMR measurements of a permalloy film. On this basis, we already moved to the more complex, ferrimagnetic insulator yttrium iron garnet (YIG) in the last section where we investigated a YIG thin film. In agreement with the literature, we found a large inhomogeneous damping and a strong Gilbert like damping which is typical for YIG thin films and obscures the intrinsic damping properties of bulk YIG. Surprisingly, the Gilbert damping parameter of YIG single crystals has not been the subject of detailed studies yet, even though magnetization dynamics in YIG were investigated in a large number of studies in the 1960s [79–81]. With the renewed interest in the magnetization dynamics of bulk YIG for applications in spintronics and quantum information storage and processing (cf. Chap. 1), this property became highly relevant. It fundamentally limits the potential of YIG in these types of experiments and detailed knowledge of the frequency-dependent magnetic relaxation of YIG is needed for their design and optimization. To extract these relaxation properties, a detailed broadband study of the magne-

tization dynamics in particular for low temperatures is needed. Two recent studies [82, 83] which have been published very close to the here presented analysis consider the temperature-dependent damping of YIG thin films. Haidar et al. [82] report a large Gilbert-like damping of unknown origin, while the low damping thin films investigated by Jermain et al. [83] show a similar behavior as reported in the following. As noted before, spheres are particularly suited for the analysis of magnetic properties and especially the intrinsic damping due to their high symmetry. In the following, we present bbFMR measurements of a YIG sphere that was produced and pre-characterized by Carsten Dubs and Oleskii Surzhenko of Innovent Jena e.V. The results in this study have been published as Ref. [MF5] from which the text and figures in this chapter are adapted and used.

The chapter is organized as follows: We first introduce the sample and its mounting in detail and give a brief review of the magnetization damping mechanisms reported for YIG. We then present the measured data and compare the evolution of the linewidth with temperature and frequency with the discussed damping models and identify the phenomenology of slowly relaxing rare-earth impurities and either the Kasuya-LeCraw mechanism or the scattering with optical magnons as the microscopic damping mechanism. The complete set of raw data and all steps of the evaluation routine are publicly available [84].

3.1 Experimental details and magnetostatic modes in spheres

The experimental setup for the investigation of the temperature-dependent broadband ferromagnetic resonance is presented in detail in Chap. 2 and in particular in Fig. 2.4. The 300 µm diameter YIG sphere is mounted above the 300 µm wide center conductor of an 8 mil thick CPW (cf. Tab. 2.1). For this, the sphere is recessed in a ≈ 0.3 mm diameter bore with the same depth in a vespel cuboid. By applying a static magnetic field with a permanent magnet perpendicular to the sample holder plane, the single crystalline sphere freely rotates so its [111] direction aligns parallel to the external magnetic field. The alignment is confirmed using Laue diffraction (Fig. 3.1 (b)) and the sample is fixed in position with a drop of PMMA. When placing the holder on the CPW (Fig. 3.1 (a)), the [111] direction is perpendicular to the CPW surface normal to better than 4.2°. We mount a pressed diphenylpicrylhydrazyl (DPPH) powder sample in a distance of

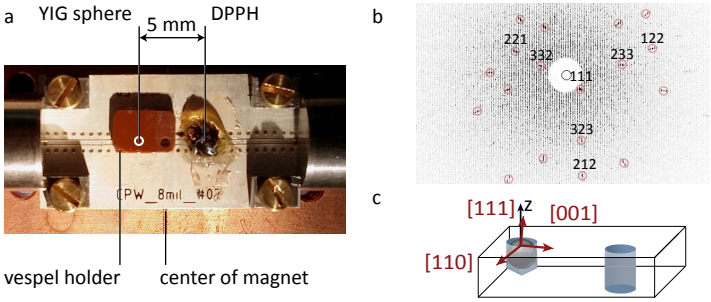

Figure 3.1: (a) Mounting of the YIG sphere (recessed in back side of the vespel holder) and the DPPH sample (pressed powder encapsulated in UV glue) on the CPW. The assembly is mounted on a cooper holder that is inserted into the cryostat as depicted in Fig. 2.4. **(b)** Laue diffraction pattern and simulated stereographic projection which describes the reflex pattern (red circles) well. The misalignment of the [111] direction with the z-axis extracted from the simulation is approximately 4.2°. **(c)** Schematic picture of the YIG sphere in the holder with annotated crystal directions.

approximately 5 mm to the sphere as shown in Fig. 3.1 (a). This assembly is mounted on a dip stick in order to place the YIG sphere in the center of a superconducting magnet (Helmholtz configuration) in a Helium gas-flow cryostat as described in detail in Chap. 2. Using the Keysight PNA vector network analyzer, the phase sensitive transmission of the setup is measured up to 43.5 GHz.

In the FMR measurements, the static external magnetic field $\mathbf{H}_0$ is applied perpendicular to the CPW surface. Hence, H_0 is pointed along the crystal [111] direction and $\mathbf{h}_{\mathrm{MW}}$ is oriented primarily perpendicular to H_0. The recorded field-frequency maps of S_{21} are corrected with the referenced background subtraction method outlined in Sec. 2.2.3. This method is chosen over the fixed field method as it efficiently supresses the spurious magnetic background signal stemming from the setup which allows to automate the fitting of the 1500 spectra. As noted in Sec. 2.2, the more complex data analysis method involving the background removal method *derivative divide* is not neccessary here as the dispersion the various resonant modes of YIG spheres are well known and a first experiment showed that they span over just 2 GHz. Instead of recording S_{21} over the whole frequency band (100 MHz to 43.5 GHz), we therefore restrict

the frequency band around the expected resonances. This reduces the measurement time compared to recording the full field-frequency map of S_{21} and hence allows us to use a higher field resolution (20 mT steps) and very high frequency resolution (100 kHz steps).

For the evaluation of the magnetization dynamics, we fit the transmission data as described in detail in Sec. 2.2 to

$$S_{21}(\omega)|_{H_0} = -i\omega A e^{i\phi}\tilde{\chi}(\omega, H_0) + B + C\cdot\omega \qquad \text{(2.4 revisited)}$$

for each H_0. $\tilde{\chi}$ is the ferromagnetic high-frequency susceptibility from Eq. (1.10) normalized to the saturation magnetization. From the fit, we extract the resonance frequency ω_{res} and the full width at half maximum (FWHM) linewidth $\Delta\omega$.

In spheres various so-called magnetostatic modes (MSMs) arise due to the electromagnetic boundary conditions [85]. These modes vary in the spatial profile of the magnetic excitation amplitude and phase and can be derived from the Landau-Lifshitz equation in the magnetostatic limit ($\nabla \times \mathbf{H} = 0$) for insulators [86]. The lineshape of all modes is given by Eq. (1.10). Due to the different spatial mode profiles and the inhomogeneous microwave field, the inductive coupling and thus A is mode dependent.[1] A detailed review of possible modes, their distribution and their dispersion relation is given by Röschmann and Dötsch [85]. We will only discuss the modes (110) and (440) in detail in the following as all the relevant characteristics of all other modes can be related to these two modes. Their linear dispersions are given by [85]

$$\omega_{\text{res}}^{110} = \gamma\mu_0 (H_0 + H_{\text{ani}}) \tag{3.1}$$

$$\omega_{\text{res}}^{440} = \gamma\mu_0 \left(H_0 + H_{\text{ani}} + \frac{M_s}{9}\right), \tag{3.2}$$

where H_{ani} is the magnetic anisotropy field along the direction of H_0, which we expect to originate from a magnetocrystalline anisotropy. Note that contrary to the thin film case discussed in the previous chapter, where

[1] Due to the comparable dimensions of center conductor width and sphere diameter, we expect that the sphere experiences an inhomogeneous microwave magnetic field with its main component parallel to the surface of the CPW and perpendicular to its center conductor. As the microwave magnetic field is sufficiently small to not cause any non-linear effects, a mode dependent excitation efficiency is the only effect of the microwave magnetic field inhomogeneity.

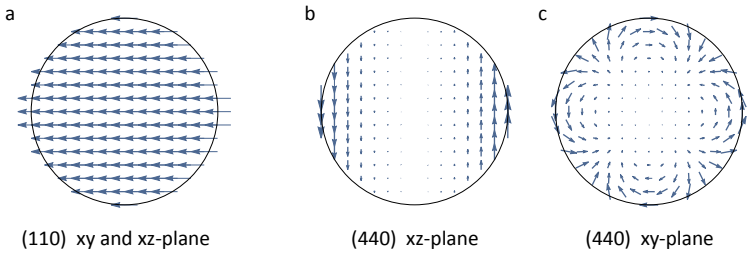

Figure 3.2: Profile of the dynamic magnetization m_x, m_y of the magnetostatic modes of a sphere in the xz ($y = 0$) plane and the xy ($z = 0$) plane (the H_0 is applied along **z**) after Ref. [87]. **(a)** (110)-mode: The profile is identical and uniform for both planes. **(b, c)** (440)-mode: A non-uniform magnetization profile with a fourfold symmetry in the xy-plane appears.

essentially $H_{\mathrm{ani}} = -M_{\mathrm{s}}$, the saturation magnetization does not enter in the equation of the fundamental mode. This is expected due to the symmetry of the sphere and the mode profile of the (110) mode which results in the same magnitude of the demagnetization field for all directions. The mode profile, i.e. the dynamic magnetization components m_x and m_y, of the (110) and (440) mode are simulated in Mathematica based on a program of Stefan Klingler following the calculations in Ref. [87]. Contrary to the uniform (110) mode, the (440) mode shows a fourfold symmetry in the xy-plane, and is located more towards the surface of the sphere. An impact of the demagnetization field on the modes dispersion as in the above equation is therefore expected.

As common in the literature, we use the more expressive, dimensionless g factor $g = \gamma\hbar/\mu_{\mathrm{B}}$ with the Bohr magneton μ_{B} (cf. Sec. 1.2) instead of γ for discussion of the results. The g-factor is a material property and is hence identical for all modes unless the different modes experience a substantially different anisotropy [88, 89]. Such an anisotropy contribution can be caused by surface pit scattering as it affects modes that are localized at the surface stronger than bulk like modes [90]. In our experiment, no such variation in g coinciding with a change in anisotropy was observed and we use a mode number independent g in the following.

Knowledge of the dispersion relations of the two modes allows to determine the saturation magnetization from

$$\mu_0 M_s(T) = \frac{9}{\gamma}\Delta\omega_M = \frac{9}{\gamma}\left(\omega_{res}^{440} - \omega_{res}^{110}\right). \tag{3.3}$$

The anisotropy field is extracted by extrapolating the dispersion relations in Eqs. (3.1) and (3.2) to $H_0 = 0$.

In the following, we investigate the $T-$ dependence of M_s, H_{ani}, g and $\Delta\omega$. Accurate determination of the g-factor and the anisotropy H_{ani} requires accurate knowledge of H_0. In order to control the temperature of the YIG sphere and CPW, they are placed in a gas-flow cryostat as described in detail in Chap. 2. The challenge in this type of setup is the exact and independent determination of the static magnetic field and its spatial inhomogeneity. Lacking an independent measure of H_0,[2] we only report the relative change of g and H_{ani} from their respective room temperature values which were determined separately using the same YIG sphere [MF4]. Note that we determine the resonance frequencies directly in frequency space. Our results on the extracted linewidth, the main focus of our study, and the magnetization are hence independent of a potential uncertainty in the absolute magnitude of H_0 and its inhomogeneity.

3.2 Relaxation theory

When relaxation properties of ferromagnets are discussed today, the most widely applied model is the Gilbert type damping discussed in Sec. 1.2. Its key signature is a linear dependence of the resonance linewidth on the resonance frequency with slope α. A linear frequency dependence is often found in experiments and the Gilbert damping parameter α serves as a figure of merit of the ferromagnetic damping that allows to compare samples and materials. In a separate bbFMR study [MF4] of the same sphere that is not discussed in detail in the following, we investigated the linewidth of

[2] The resonance frequency of the DPPH sample that was measured simultaneously was intended as a field calibration but can not be utilized due to the magnetic field inhomogeneity. In particular, since the homogeneity of our superconducting magnet system is specified to 1 ‰ for an off-axis deviation of 2.5 mm, the spatial separation of 5 mm of the DPPH and the YIG sphere already falsifies DPPH as an independent magnetic field standard. Placing DPPH and YIG in closer proximity is problematic as the stray field of the YIG sphere will affect the resonance frequency of the DPPH. Note further that we are not aware of any reports showing the temperature independence of the DPPH g-factor with the required accuracy.

all visible magnetostatic modes of the YIG sphere at room temperature in collaboration with Stefan Klingler. We find that the Gilbert damping parameter α is identical for all magnetostatic modes. The inhomogeneous linewidth $\Delta\omega$, on the other hand, varies with the localization of the observed magnetostatic mode towards the surface of the sphere. We successfully model the data quantitatively and conclude that $\Delta\omega$ is caused mainly by surface pit scattering while the Gilbert-like damping is a property of the bulk material.

The Gilbert-damping parameter α alone contains little insight into the underlying physical mechanisms. In order to understand the underlying microscopic relaxation processes of YIG, extensive work has been carried out. Improvements on both the experimental side (low temperatures [91], temperature dependence [79, 92, 93], separate measurements of M_z and M_{xy} [80]) and on the sample preparation (varying the surface pit size [90], purifying Yttrium [79], doping YIG with silicon [94] and rare-earth elements [94–97]) led to a better understanding of these mechanisms.

However, despite these efforts, the microscopic origin of the dominant relaxation mechanism for bulk YIG at room temperature is still under debate. It has been described by a two-magnon process by Kasuya and LeCraw [92] (1961). In this process, a uniformly-precessing magnon ($k = 0$) relaxes under absorption of a phonon to a $k \neq 0$ magnon. If the thermal energy $k_B T$ is much larger than the energy of the involved magnons and phonons ($T > 100\,\mathrm{K}$) and low enough that no higher-order processes such as four-magnon scattering play a role ($T < 350\,\mathrm{K}$), the Kasuya-LeCraw process yields a linewidth that is linear in frequency and temperature: $\Delta\omega_{\mathrm{KL}} \propto T, f$ [92, 94]. This microscopic process is therefore considered to be the physical process that explains the phenomenological Gilbert damping for low-damping bulk YIG. More recently, Cherepanov et al. [45] pointed out that the calculations by Kasuya and LeCraw [92] assume a quadratic magnon dispersion in k-space which is only correct for very small wave numbers k. Taking into account a more realistic magnon dispersion (quadratic at low k, linear to higher k), the Kasuya-LeCraw mechanism gives a value for the relaxation rate that is not in line with the experimental results. Cherepanov therefore developed an alternative model that traces back the linear frequency and temperature dependence at high temperatures (150 K to 300 K) to the interaction of the uniform-precession mode with optical magnons of high frequency. Recently, atomistic calculations by Barker and Bauer [98] confirmed the assumptions on the magnon spec-

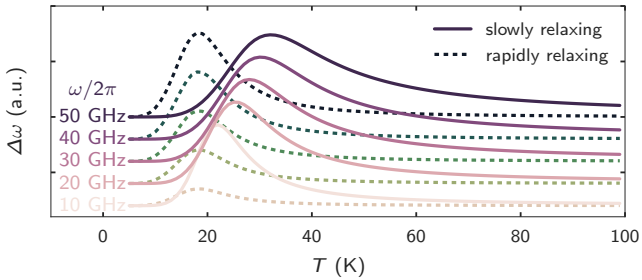

Figure 3.3: Signature of the relaxation of YIG excitations via rare-earth impurities. Shown is the qualitative dependence of the linewidth with temperature for different excitation frequencies (each trace is offset by a constant value). For the slowly relaxing impurity case (solid lines) the peak temperature increases with increasing temperature according to Eq. (3.4). For the rapidly relaxing impurity case (dashed lines), the peak temperature stays constant with changing frequency according to Ref. [94], Eq. (6.18). In both cases, an Orbach process has been taken into account for τ_{RE}.

trum that are necessary for the quantitative agreement of the latter theory with experiment.

Both theories, the Kasuya-LeCraw theory and the Cherepanov theory, aim to describe the microscopic origin of the intrinsic damping. They deviate in their prediction only in the low-temperature ($T < 100\,\mathrm{K}$) behavior [94]. At these temperatures, however, impurities typically dominate the relaxation and mask the contribution of the intrinsic damping process. Therefore, the dominant microscopic origin of the YIG damping at temperatures above 150K has not been unambiguously determined to date.

If rare-earth impurities with large orbital momentum exist in the crystal lattice, their exchange coupling with the iron ions introduces an additional relaxation channel for the uniform precession mode of YIG. Depending on the relaxation rate of the rare-earth impurities with respect to the magneto–dynamics of YIG, they are classified into slowly and rapidly relaxing rare-earth impurities. This is an important distinction as the efficiency of the relaxation of the fundamental mode of YIG via the rare-earth ion to the lattice at a given frequency depends on the relaxation rate of the rare-earth ion and the strength of the exchange coupling. In both, the slow and the rapidly relaxor case, a characteristic peak-like maximum is

observed in the linewidth vs. temperature dependence at a characteristic, frequency-dependent temperature [81]. The frequency dependence of this peak temperature allows to distinguish rapidly and slowly relaxing rare-earth ions: The model of a rapidly relaxing impurity predicts that the peak temperature is constant, while in the case of slowly relaxing rare-earth ions the peak temperature is expected to increase with increasing magnetic field (or frequency). These signatures of slowly and rapidly relaxing impurity are visualized in Fig. 3.3. The relaxation rate of rare-earths τ_{RE} is typically modeled by a direct magnon to phonon relaxation, an Orbach processes [99, 100] that involves two phonons, or a combination of both. The inverse relaxation rate of an Orbach process is described by

$$\frac{1}{\tau^{\mathrm{Orbach}}} = \frac{B}{e^{\Delta/(k_{\mathrm{B}}T)} - 1},$$

with the crystal field splitting Δ and a proportionality factor B. A direct process leads to an inverse relaxation rate of

$$\frac{1}{\tau^{\mathrm{direct}}} = \frac{1}{\tau_0} \coth \frac{\delta}{2k_{\mathrm{B}}T},$$

with τ_0, the relaxation time at $T = 0\,\mathrm{K}$. The evolution of the rare earth's relaxation rate with temperature sensitively influences the linewidth peak shape and temperature. It has been found experimentally that most rare-earth impurities are to be classified as slow relaxors [94]. The sample investigated here is not intentionally doped with a certain rare-earth element and the peak frequency and temperature dependence indicates a slow relaxor. We therefore focus on the slow relaxing rare-earth impurity model in the following.

Deriving the theory of the slowly and rapidly relaxing impurities has been performed comprehensively elsewhere [94]. The linewidth contribution caused by a slowly relaxing rare-earth impurity is given by [95]:

$$\Delta\omega^{\mathrm{SR}} = C \frac{\omega\tau_{\mathrm{RE}}}{1 + (\omega\tau_{\mathrm{RE}})^2} \tag{3.4}$$

with $C \propto \frac{1}{k_{\mathrm{B}}T} \operatorname{sech}\left(\frac{\delta_{\mathrm{a}}}{2k_{\mathrm{B}}T}\right)$. Therein, δ_{a} is the splitting of the rare-earth Kramers doublet which is given by the temperature independent exchange interaction between the iron ions and the rare-earth ions.

Also Fe^{2+} impurities in YIG give rise to a process that leads to a linewidth peak at a certain temperature. The physical origin of this so-called valence exchange or charge-transfer linewidth broadening is electron

hopping between the iron ions [94]. Simplified, it can be viewed as a two level system just like a rare-earth ion and thus results in the same characteristic linewidth maximum as a slowly relaxing rare-earth ion. For valence exchange, the energy barrier Δ_{hop} that needs to be overcome for hopping determines the time scale of the relaxation process. The two processes, valence exchange and rare-earth impurity relaxation, can therefore typically not be told apart from FMR measurements only. In the following, we use the slow relaxor mechanism exclusively. This model consistently describes our measurement data and the resulting model parameters are in good agreement with the literature. We would like to emphasize, however, that the valence exchange mechanism as the relevant microscopic process resulting for magnetization damping can not be ruled out from our measurements.

3.3 Experimental results and discussion

Two exemplary S_{21} broadband spectra (the background is corrected as described above) at two distinct temperatures are shown in Fig. 3.4. The color-coded magnitude $|S_{21}|$ is a measure for the absorbed microwave power. High absorption (bright color) indicates the resonant excitation of a MSM in the YIG sphere or the excitation of the electron paramagnetic resonance of the DPPH. In the color plot, the color scale is truncated in order to improve visibility of small amplitude resonances. In addition, the frequency axis is shifted relative to the resonance frequency of a linear dispersion with $g = 2.0054$ ($\omega_{\mathrm{res}}^{g=2.0054} = \frac{g\mu_{\mathrm{B}}}{\hbar}\mu_0 H$) for each field. In this way, modes with $g = 2.0054$ appear as vertical lines and a g-factor that deviates from this value is hence easily recognized by it's different slope. This representation of the data may seem convoluted at first but is superior to a field-frequency map with the usual, unshifted axis as it allows to distinguish the various resonant modes over the whole frequency and field range. Comparing the spectra at 290 K (Fig. 3.4 (a)) to the spectra at 20 K (Fig. 3.4 (b)), an increase of the g-factor is observed for all resonance modes upon reducing the temperature. The rich mode spectrum makes it necessary to carefully identify the modes and assign mode numbers. Note that the occurrence of a particular mode in the spectrum depends on the position of the sphere with respect to the CPW due to its inhomogeneous excitation field. We employ the same method of identifying the modes as used in Ref. [MF4] and find consistent mode spectra. As mentioned before, we do not use the DPPH resonance (green arrow in Fig. 3.4) but

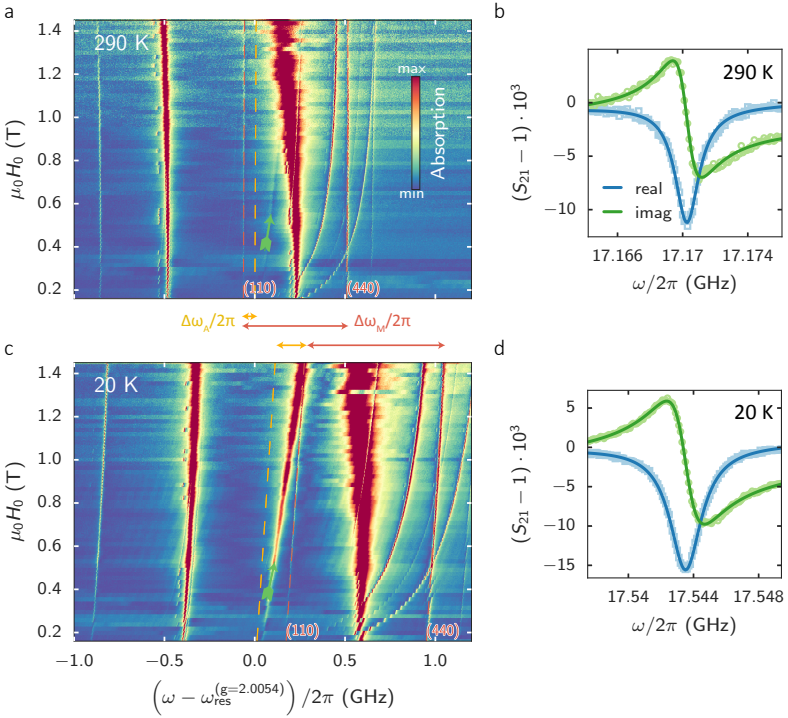

Figure 3.4: (a, b) Eigenmode spectra of the YIG sphere at (a) 290 K and (c) 20 K. The (110) and (440) MSM are marked with red dashed lines. The change in their slope gives the change of the g-factor of YIG. Their splitting ($\Delta\omega_M$, red arrow) depends linearly on the YIG magnetization. The increase in M_s to lower temperatures is already apparent from the increased splitting $\Delta\omega_M$. Marked in orange is the offset of the resonance frequency $\Delta\omega_A$ extrapolated to $H_0 = 0$ resulting from anisotropy fields H_{ani} present in the sphere. The green marker denotes the position of the DPPH resonance line which increases in amplitude considerably to lower temperatures. **(b, d)** $S_{21} - 1$ (data points) and fit to Eq. (2.4) (lines) at $\mu_0 H = 615\,\mathrm{mT}$ for both temperatures.

the (110) YIG mode as field reference. For this field reference, we take $g(290\,\mathrm{K}) = 2.0054$ and $\frac{\gamma}{2\pi}\mu_0 H_{\mathrm{ani}}(290\,\mathrm{K}) = 68.5\,\mathrm{MHz}$ determined for the same YIG sphere at room temperature in an electromagnet [MF4], which provides a more accurate knowledge of the applied external magnetic field (cf. Chap. 2). The discrepancy of the DPPH g-value from the literature values of $g = 2.0036$ is attributed to the non-optimal location of the DPPH specimen in the homogeneous region of the superconducting magnet coils.

In Fig. 3.4, the fitted dispersion relations of the (110) and (440) modes according to Eq. (3.1) and (3.2) are shown as dashed red lines. As noted previously, we only analyze these two modes in detail as all parameters can be extracted from just two modes. The (110) and (440) mode can be easily and unambiguously identified by simply comparing the spectra with the ones found in Ref. [MF4]. Furthermore, at high fields, both modes are clearly separated from other modes. This is necessary as modes can start hybridizing when their (unperturbed) resonance frequencies are very similar which makes a reliable determination of the linewidth and resonance frequency impossible The hybridization of the modes is visible in the low-field region of Fig. 3.4 (b) which is also displayed as zoom in Fig. 6.6 and discussed in this chapter in the context of strong coupling physics. These attributes make the (110) and the (440) mode the ideal choice for the analysis.

As described in Sec. 3.1, we simultaneously fit the (110) and the (440) dispersions with the same g-factor in order to extract M_{s}, H_{ani} and g. In the fit, we only take the high-field dispersion of the modes into account where no other modes intersect the dispersion of the (110) and (440) modes. The results are shown in Fig. 3.5. Note that the statistical uncertainty from the fit is not visible on the scale of any of the parameters M_{s}, H_{ani} and g. Following the work of Solt [101], we model the resulting temperature dependence of the magnetization (Fig. 3.5 (a)) with the Bloch-law taking only the first order correction into account:

$$M_{\mathrm{s}} = M_0 \left(1 - aT^{\frac{3}{2}} - bT^{\frac{5}{2}}\right). \tag{3.5}$$

The best fit is obtained for $\mu_0 M_0 = 249.5(5)\,\mathrm{mT}$, $a = 23(3) \times 10^{-6}\,\mathrm{K}^{-3/2}$ and $b = 1.08(11) \times 10^{-7}\,\mathrm{K}^{-5/2}$. The obtained fit parameters depend strongly on the temperature window in which the data is fitted. Hence, the underlying physics determining the constants a and b cannot be resolved.[3]

[3] Note that we failed to reproduce the fit of Ref. [101] using the data provided in this paper and that the reasonable agreement with the there-reported fit parameters might be coincidence.

We find reasonable agreement with results determined using a vibrating sample magnetometer [101], a Sucksmith-type [102] apparatus [103, 104], presumably using some sort of magnetometer measurement [105], and a not-mentioned technique [106]. In Fig. 3.5, these results are plotted for reference and comparison. Our data systematically deviates by a few millitesla from the often-quoted data of Anderson [103] and from the data of Gilleo and Geller [104]. On the other hand, our results of M_s are in very good agreement with the results of Hansen et al. [107] which have been obtained with the same technique as used in this work. In particular, the room temperature saturation magnetization of $\mu_0 M_s(300\,\mathrm{K}) = 180.0(8)\,\mathrm{mT}$ is in perfect agreement with values reported in the literature [46, 47]. Note that the Sucksmith-type apparatus as used in the former measurements measures the magnetic moment by placing it in a magnetic field gradient and measuring the force using a vacuum balance. The calibration of the magnetic field gradient therefore influences the absolute measured value of M_s sensitively and magnetic anisotropy fields need to be taken into account. Using FMR, M_s is given by the splitting of the modes which is measured purely in frequency space and hence, errors in the magnetic field calibration do not add to the uncertainty. Furthermore, the magnetic anisotropies are separated and do not influence the measurement of M_s as described above. We detect a small non-linearity of the (110) and (440) mode dispersions that is most likely due to deviations from an ideal spherical shape or strain due to the YIG mounting. This results in a systematic, temperature independent residual of the linear fits to these dispersions. This resulting systematic error of the magnetization is incorporated in the uncertainty given above. However, a deviation from the ideal spherical shape, strain in the holder or a misalignment of the static magnetic field can also modify the splitting of the modes and hence result in a different M_s [108]. This fact may explain the small discrepancy of the value determined here and the value determined for the same sphere in a different setup at room temperature [MF4].

From the same fit that we use to determine the magnetization, we can deduce the temperature dependence of the anisotropy field $\mu_0 H_{\mathrm{ani}}$ (Fig. 3.5 (b)). Most notably, H_{ani} changes sign at 200 K which has not been observed in the literature before and can be an indication that the sample is slightly strained in the holder. The resonance frequency of DPPH extrapolated to $\mu_0 H_0 = 0$ (Δf_{ani}, red squares) confirms that the error in the determined value H_{ani} is indeed temperature independent and very close to zero. Thus, the extracted value for the anisotropy is not merely given by an offset in the static magnetic field.

The evolution of the g-factor with temperature is shown in Fig. 3.5 (c). It changes from 2.005 at room temperature to 2.010 at 10 K where it seems to approach a constant value. As mentioned before, the modes' dispersion is slightly non-linear giving rise to a systematic, temperature independent uncertainty in the determination of g of ± 0.0008. The g-factor of YIG has been determined using the MSMs of a sphere for a few selected temperatures before [81]. Comparing our data to these results, one finds that the trend of the temperature dependence of g agrees. However, the absolute value of g and the magnitude of the variation differ. At the same time, we find a change of the g-factor of DPPH that is on the scale of 0.0012. This may be attributed to a movement of the sample slightly away from the center of magnet with changing temperature due to thermal contraction of the dip stick. In this case, the YIG g-factor has to be corrected by this change. The magnitude of this effect on the YIG g-factor can not be estimated reliably from the change of the DPPH g-factor alone. Furthermore, the temperature dependence of the DPPH g-factor has not been investigated with the required accuracy in the literature to date to allow excluding a temperature dependence of the g-factor of DPPH. We therefore do not present the corrected data but conclude that we observe a change in the YIG g-factor from room temperature to 10 K of at least 0.2 %.

Next, we turn to the analysis of the damping properties of YIG. We will almost exclusively discuss the damping of the (110) mode in the following but the results also hold quantitatively and qualitatively for the other modes [MF4]. This is shown exemplarily in Fig. 3.6 (b) for the temperature evolution of the linewidth at constant magnetic field. In particular, the linewidth peak temperature is identical for both modes for all fields (frequencies) while the absolute value is slightly higher. This can be attributed partially to the higher resonance frequency of the (440) mode and hence the higher linewidth due to the Gilbert like damping but mainly represents the scatter of the data (cf. Fig. 3.6 (a)). Varying the applied microwave excitation power P (not shown) confirms that no nonlinear effects such as a power broadening of the modes are observed with $P = 0.1$ mW. Note that due to the microwave attenuation in the microwave cabling, the microwave field at the sample location decreases with increasing frequency for the constant excitation power.

First, we evaluate the frequency-dependent linewidth for several selected temperatures (Fig. 3.6 (a)). At temperatures above 100 K, a linear dependence of the linewidth with the resonance frequency is observed. This dependence is the usual Gilbert-like damping and the slope is described by

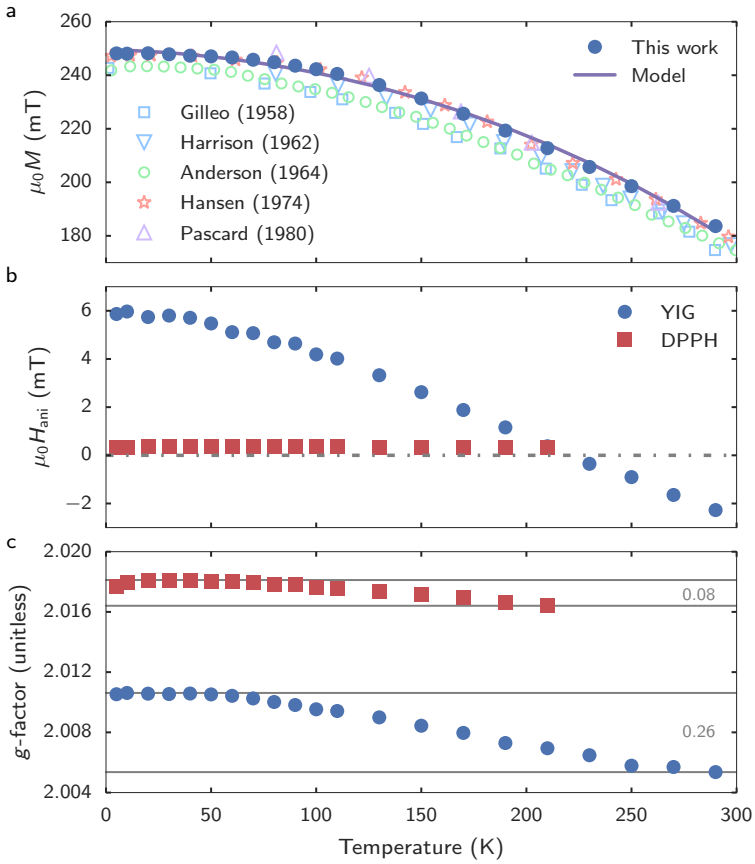

Figure 3.5: **(a)** YIG magnetization as function of temperature extracted from the (110) and (440) mode dispersions using Eq. (3.3). The purple line shows the fit to a Bloch model (cf. parameters in the main text). Plotted for reference are the results of Refs. [46, 103–106]. **(b)** YIG anisotropy field $\mu_0 H_{\mathrm{ani}}(T) = \Delta\omega_{\mathrm{ani}}/\gamma$. Red squares: Same procedure applied to the DPPH dispersion as reference. **(c)** YIG g-factor (blue circles). For reference, the extracted DPPH g-factor is also shown (red squares). The gray numbers indicate the relative change of the g-factors from the lowest to the highest measured temperature (gray horizontal lines). As we use the YIG (110) mode as the magnetic field reference, the extracted value of g and H_{ani} at 300 K are fixed to the values determined in the room temperature setup [MF4]. Figure adapted from Ref. [MF6].

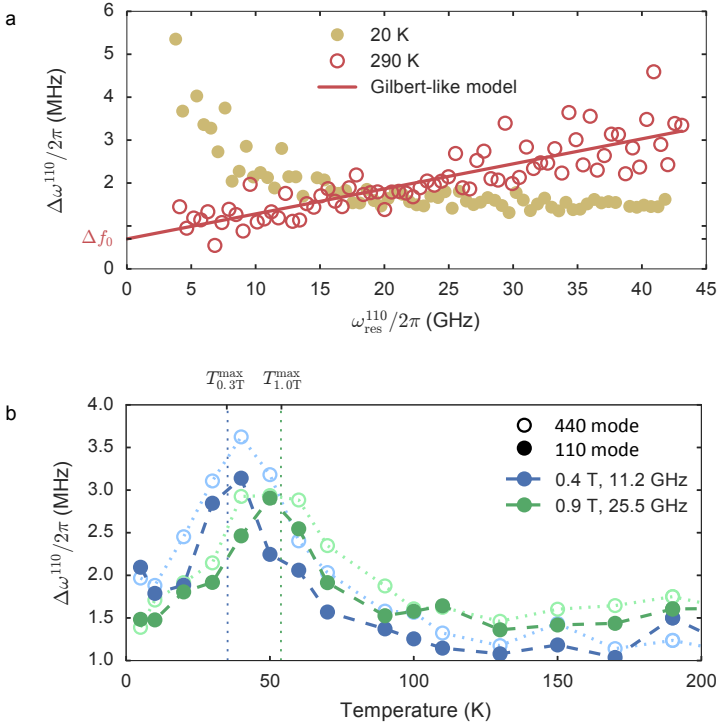

Figure 3.6: (a) Full width at half maximum (FWHM) linewidth $\Delta\omega^{110}_{\mathrm{res}}$ of the (110) mode as a function of frequency for different temperatures. A linear Gilbert-like interpretation is justified in the high-T case ($T > 100\,\mathrm{K}$) only. Below 100 K, the slope of $\Delta\omega^{110}(\omega^{110}_{\mathrm{res}})$ is not linear so that a Gilbert type interpretation is no longer applicable. **(b)** FWHM linewidth of the (110) mode (filled symbols) and the (440) mode (open symbols) as a function of temperature for two different fixed external magnetic fields (the frequency is given for reference for the (110) mode at room temperature). The linewidth peaks at a magnetic field-dependent temperature that can be modeled using the phenomenology of rare-earth impurities resulting in T_{max} (vertical dotted lines). Figure adapted from Ref. [MF6].

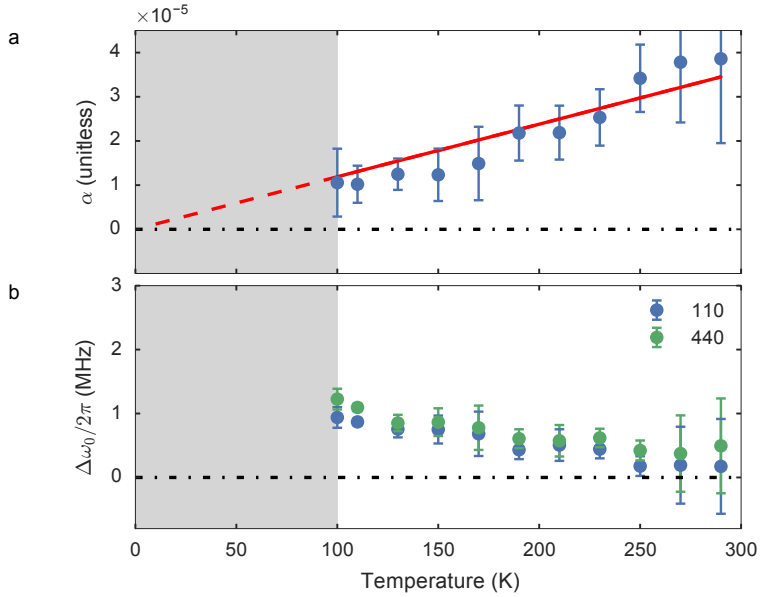

Figure 3.7: (a) Gilbert damping parameter α determined from the slope of a linear fit to the $\Delta\omega(f,T)$ data for frequencies above 20 GHz. The red line shows the linear dependence of the linewidth with temperature expected from the Kasuya-LeCraw process. **(b)** Inhomogeneous linewidth $\Delta\omega_0$ (intersect of the aforementioned fit with $\omega_{\mathrm{res}}^{110} = 0$) as a function of temperature. The inhomogeneous linewidth shows a slight increase with decreasing temperature down to 100 K. In the region where the slow relaxor dominates the linewidth (gray shaded area, cf. Fig. 3.6), the linear fit is not applicable and unphysical damping parameters and inhomogeneous linewidths are extracted. Figure taken from Ref. [MF6].

the Gilbert damping parameter α. A linear frequency dependence of the damping in bulk YIG has been described by the theory developed by Kasuya and LeCraw [92] and the theory developed by Cherepanov et al. [45] (cf. Sec. 3.2). We extract α from a global fit of a linear model to the (110) and (440) linewidth with separate parameters for the inhomogeneous linewidths $\Delta\omega_0^{110}$ and $\Delta\omega_0^{440}$ and a shared Gilbert damping parameter α for all modes (cf Eq. (1.6)):

$$\Delta\omega = 2\alpha\omega + \Delta\omega_0^{110,440} \tag{3.6}$$

The fit is shown exemplarily for the 290 K (red) data in Fig. 3.6 (a).

The Gilbert damping parameter α extracted using this fitting routine for each temperature is shown in Fig. 3.7 (a). Consistently with both theories, α increases with increasing temperature. The error bars in the figure correspond to the maximal deviation of α extracted from separate fits for each mode. They therefore give a measure of how α scatters in between modes. The statistical error of the fit (typically ± 0.00001) is not visible on this scale. The Gilbert damping parameter α linearly extrapolated to zero temperature vanishes. Note that this is consistent with the magnon-phonon process described by Kasuya and LeCraw [92] but not with the theory developed by Cherepanov et al. [45]. For room temperature, we extract a Gilbert damping of 4×10^{-5} which is in excellent agreement with the literature value [MF4, 109]. From the fit, we also extract the inhomogeneous linewidth $\Delta\omega_0$, which we primarily associate with surface pit scattering (Sec. 3.2, Ref. [MF4]). In the data, a slight increase of $\Delta\omega_0$ towards lower temperatures is present (Fig. 3.7 (b)). Such a change in the inhomogeneous linewidth can be caused by a change in the surface pit scattering contribution when the spin-wave manifold changes with M_s [MF4, 90].

Note that according to Fig. 3.7 (b) $\Delta\omega_0$ is higher for the (440) mode than for the (110) mode. This is in agreement with the theoretical expectation that surface pit scattering has a higher impact on $\Delta\omega_0$ for modes that are more localized at the surface of the sphere like the (440) mode compared to the more bulk-like modes such as the (110) mode [90].[4]

[4] In comparison to Klingler et al. [MF4], here, we do not see an increased inhomogeneous linewidth of the (110) mode and no secondary mode that is almost degenerate with the (110) mode. The difference can be explained by the orientation of the sphere which is very difficult to reproduce very accurately ($< 1°$) between the experimental setups: The change in orientation either separates the mode that is almost degenerate to the (110) mode or makes the degeneracy more perfect in our setup. The different placement of the sphere on the CPW can also lead to

Turning back to Fig. 3.6 (a), for low temperatures (20 K, orange data points), a Gilbert-like damping model is obviously not appropriate as the linewidth increases considerably towards lower frequencies instead of increasing linearly with increasing frequency. Typically, one assumes that the damping at low frequencies is dominated by so-called low field losses that may arise due to domain formation. The usual approach is then to fit a linear trend to the high-frequency behavior only. Note, however, that even though the frequency range we use is already larger than usually reported [82, 83, 110], this approach yields an unphysical, negative damping. We conclude that the model of a Gilbert-like damping is only valid for temperatures exceeding 100 K (Fig. 3.7) for the employed field and frequency range.

The linewidth data available in the literature are typically taken at a fixed frequency and the linewidth is displayed as a function of temperature [81, 93, 94]. We can approximately reproduce these results by plotting the measured linewidth at fixed H_0 as a function of temperature (Fig. 3.6 (b)).[5] A peak-like maximum of the linewidth below 100 K is clearly visible. For increasing magnetic field (frequency), the peak position shifts to higher temperatures. This is the signature of a slowly relaxing rare-earth impurity (Sec. 3.2). A rapidly relaxing impurity is expected to result in a field-independent linewidth vs. temperature peak and can thus be ruled out. At the peak position, the linewidth shows an increase by 2.5 MHz which translates with the gyromagnetic ratio to a field linewidth increase of 0.08 mT. For 0.1 at. % Terbium doped YIG, a linewidth increase of 80 mT has been observed [111]. Considering that the linewidth broadening is proportional to the impurity concentration and taking the specified purity of the source material of 99.9999% used to grow the YIG sphere investigated here, we estimate an increase of the linewidth of 0.08 mT, in excellent agreement with the observed value.

Modeling the linewidth data is more challenging: The model of a slowly relaxing rare-earth ion contains the exchange coupling of the rare-earth ion and the iron sublattice, and its temperature-dependent relaxation frequency as parameters. As noted before, a direct and an Orbach process are typically used to model the relaxation rate and both of these processes have two free parameters. Unless these parameters are known from other experiments for the specific impurity and its concentration in the sample, fitting the model

a situation where the degenerate mode is not excited and therefore does not interfere with the fit.

[5] Naturally, the resonance frequency varies slightly (± 0.9 GHz) between the data points because the magnetization and the anisotropy changes with temperature.

to the temperature behavior of the linewidth at just one fixed frequency gives ambiguous parameters. In principle, frequency resolved experiments as presented here make the determination of the parameters more robust as the mechanism responsible for the rare-earth relaxation is expected not to vary as a function of frequency. The complete frequency and field dependence of the linewidth is shown in Fig. 3.8. At temperatures above approx 100 K, the linewidth increases monotonically with field, in agreement with a dominantly Gilbert-like damping mechanisms, which becomes stronger for higher temperatures. On the same linear color scale, the linewidth peak below 100 K and its frequency evolution is apparent. Fig. 3.6 (b) corresponds to horizontal cuts of the data in Fig. 3.8 at $\mu_0 H_0 = 341$ and 1007 mT.

For typical YIG spheres, that are not specifically enriched with only one rare-earth element, the composition of the impurities is unknown. Different rare-earth ions contribute almost additively to the linewidth and have their own characteristic temperature-dependent relaxation frequency respectively peak position. This is most probably the case for the YIG sphere of this study. The constant magnitude of the peak above 0.3 T and the constant peak width indicates that rapidly relaxing rare-earth ions play a minor role. The evolution of the linewidth with H_0 and ω can therefore not be fitted to one set of parameters. We thus take a different approach and model just the shift of the peak position in frequency and temperature as originating from a single slowly relaxing rare-earth impurity. For this, we use a value for the exchange coupling energy between the rare-earth ions and the iron sublattice in a range compatible with the literature [94] of $\delta_a = 2.50\,\text{meV}$. To model the rare-earth relaxation rate as a function of temperature, we use the values determined by Clarke [96] for Neodymium doped YIG: $\tau_0 = 2.5 \times 10^{-11}\,\text{s}$ for the direct process and $\Delta = 10.54\,\text{meV}$ and $B = 9 \times 10^{11}\,\text{s}^{-1}$ for the Orbach process. The model result, i.e. the peak position, is shown as dashed line in Fig. 3.8 and shows good agreement with the data. This indicates that, even though valence exchange and other types of impurities cannot be rigorously excluded, rare-earth ions are indeed the dominant source for the linewidth peak at low temperatures.

3.4 Conclusions

In this section, we used the broadband FMR setup, the background removal methods and the data analysis models from Chap. 2 to investigate the mag-

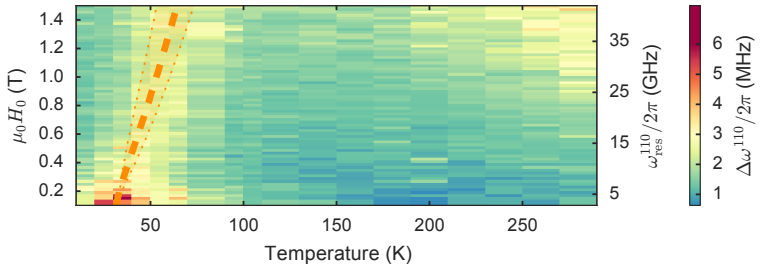

Figure 3.8: Full map of the FWHM linewidth of the (110) mode as function of temperature and field resp. resonance frequency $\omega_{\mathrm{res}}^{110}$. At low temperatures, only the slow relaxor peak is visible while at high temperatures the Gilbert-like damping becomes dominant. The position of the peak in the linewidth modeled by a slow relaxor is shown as dashed orange line. The model parameters are taken from Clarke et al. [95] and taking $\delta_a = 2.50\,\mathrm{meV}$. The dotted lines indicate the deviation of the model for $0.5\delta_a$ (lower $T^{\max}$) and $2\delta_a$ (higher $T^{\max}$). Figure taken from Ref. [MF6].

netization dynamics of a YIG sphere as a function of temperature. We extract the temperature-dependent magnetic properties M_s, H_{ani} and γ of YIG from the FMR dispersion relation of various magnetostatic modes and measure the temperature-dependent resonance linewidth. In agreement with the literature, we find that single crystalline YIG features an exceptionally low Gilbert-like damping with $\alpha = 4 \cdot 10^{-5}$ at room temperature – over two orders of magnitude lower than the Gilbert-damping parameter of permalloy ($\alpha = 7 \cdot 10^{-3}$) or a typical YIG thin film ($\alpha = 5 \cdot 10^{-3}$) that we determined in Sec. 2.2. The linear decrease of the YIG Gilbert-damping parameter α with decreasing temperature that we find matches well with the two microscopic theories given by Kasuya and LeCraw [92] and Cherepanov et al. [45]. Unfortunately, using our data it is not possible to unambiguously rule out one of the two competing theories. One approach to achieve this is to investigate a material where the splitting of the ferromagnetic and antiferromagnetic magnon branches can be controlled. The interaction of these magnon branches is the basis of the theory of Cherepanov et al. [45] and it is predicted that the splitting of the branches directly influences the relaxation rate which manifests in a change of the Gilbert-damping parameter. Achieving this is conceivable using GdIG, which features an additional magnon mode that considerably shifts in energy with temperature. A broad-

band study of GdIG is the topic of the following chapter. Furthermore, we find that below 100 K, the relaxation is dominated by slowly relaxing (rare-earth) impurities and gives rise to a characteristic linewidth maximum around 50 K. Here, examining a YIG single crystal that is doped intentionally with a certain rare-earth impurity is an interesting task which has only been performed with single frequency FMR measurements before [95, 96, 111]. Therefore, the frequency dependence of the resonance linewidth in such a intentionally enriched system remains to be investigated. Also here, it is very interesting to see how the magnetic properties of the YIG change, when the yttrium ion is not only partially substituted but completely replaced with a rare-earth element with a magnetic moment. We will describe a study of the damping and the magnetic anisotropy of a GdIG film, which represents such a substituted iron garnet, in the following chapter.

Chapter 4

Magnetization damping and anisotropy of GdIG thin films

In this section, we study the magnetic properties of a GdIG thin film sample using bbFMR and SQUID magnetometry. This study is published as Ref. [MF7]. Parts of the text and figures in this section are adapted from this reference. We use GdIG as a prototypical example of an iron garnet where the yttrium ions on the *c* lattice site are fully substituted with Gd ions which carry a magnetic moment. Using our bbFMR setup we extract the magnetic damping properties of GdIG as a function of temperature and report the magnetic properties of GdIG, confirming and extending previous results [30]. Furthermore, by changing the temperature, we achieve a transition from the typical in-plane magnetic anisotropy (IPA), dominated by the magnetic shape anisotropy, to a perpendicular magnetic anisotropy (PMA) at about 190 K. The change of the anisotropy form IPA to PMA is confirmed in an independent SQUID magnetometry measurement.

Sample details

The sample that we investigate is a 2.6 µm thick GdIG film grown by liquid phase epitaxy (LPE) on a (111)-oriented gadolinium gallium garnet substrate (GGG) provided by Zhiyong Qiu from the Institute for Materials

Research, Tohoku University, Sendai, Japan. The general magnetic properties of GdIG are introduced in Chap. 1. In the following, we will especially use the fact that the net remanent magnetization of GdIG vanishes at the so-called compensation temperature T_{comp}. The typical magnetic anisotropies in thin garnet films are the shape anisotropy and the cubic magnetocrystalline anisotropy, but also growth induced anisotropies and magnetoelastic effects due to epitaxial strain have been reported in the literature [112, 113]. We find that our experimental data can be understood by taking into account only shape anisotropy and an additional anisotropy field perpendicular to the film plane. A full determination of the anisotropy contributions is in principle possible with FMR and angle-dependent measurements indicate a cubic anisotropy as the origin of the additional anisotropy field. The low signal amplitude and the large FMR linewidth towards T_{comp} (see below), however, renders a complete, temperature-dependent anisotropy analysis impossible. In the following, we therefore exclusively use the shape anisotropy and the additional out-of-plane anisotropy field for the discussion of the magnetic anisotropy of GdIG.

Broadband ferromagnetic resonance

We perform broadband FMR measurements [114] as a function of temperature with the external magnetic field H_0 applied along the film normal (out-of-plane, oop).[1] In this configuration, two-magnon scattering is suppressed and hence, the linewidth is expected to be smaller than for the in-plane magnetized case [115, 116]. The microwave transmission S_{21} is recorded while sweeping H_0 at various fixed frequencies between 10 GHz and 25 GHz using the Keysight PNA-X VNA. We chose this measurement configuration and procedure (cf. Sec. 2.2) because we expect a very small signal to noise ratio close to the compensation point due to the vanishing net remanent magnetization. Furthermore, the dispersion relation of the material at a certain temperature can be predicted accurately by using the results from measurements at lower temperatures with a larger signal to noise ratio.

[1] The alignment of the sample is confirmed at low temperatures by performing rotations of the magnetic field direction at fixed magnetic field magnitude while recording the frequency of resonance ω_{res}. As the shape anisotropy dominates at low temperatures, ω_{res} goes through an easy-to-identify minimum when the sample is aligned oop.

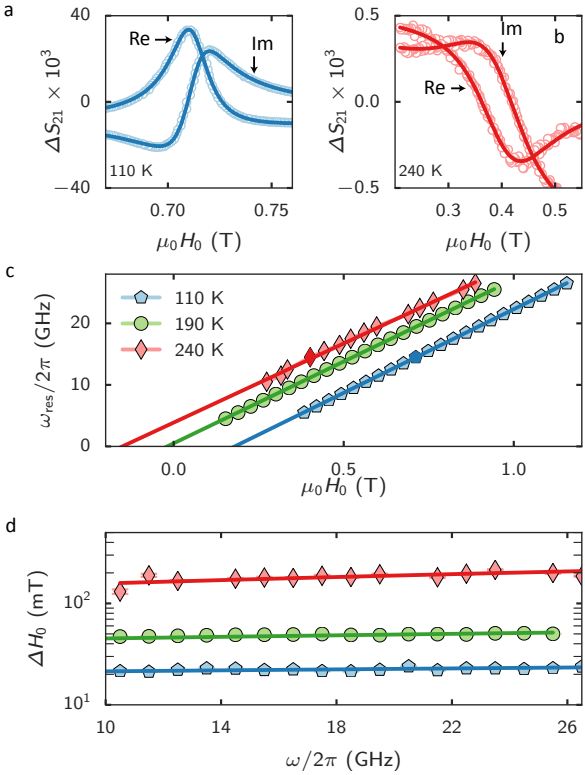

Figure 4.1: (a, b) Exemplary resonance spectra (symbols) at 14.5 GHz recorded at 110 K and 240 K as well as the fits to Eq. (2.3) (solid lines). A complex offset S_{21}^0 has been subtracted for visual clarity, plotted is $\Delta S_{21} = S_{21} - S_{21}^0$. **(c)** FMR resonance frequency plotted against H_0 taken for three different temperatures (symbols) and fit to Eq. (1.15) (solid lines). For an IPA, a positive effective magnetization M_{eff} (positive x-axis intercept) is extracted, whereas M_{eff} is negative for a PMA. **(d)** FMR field space linewidth as a function of ω_{res} (symbols) for the same three temperatures as in (c) and fit to Eq. (1.6)$\cdot\mu_0$ (solid lines). Parts of the figure are adapted from Ref. [MF7].

We analyze the data as described in Sec. 2.2.1 by performing fits of S_{21} at constant frequencies ω as a function of H_0 to

$$S_{21}(H_0)|_\omega = -i\omega A e^{i\phi}\tilde{\chi}(\omega, H_0) + B + C \cdot H_0. \qquad \text{(2.3 revisited)}$$

The complex parameters B and C account for a linear field-dependent background signal of S_{21}, A is the complex FMR amplitude, and $\tilde{\chi}$ is the Polder susceptibility in field space for an out-of-plane magnetized film (Eq. (1.16)) normalized to the magnetization. Exemplary data for S_{21} (symbols) and the fits to Eq. (2.3) (solid lines) at two distinct temperatures are shown in Fig. 4.1 (a, b). We obtain excellent agreement of the fits and the data. The data furthermore show that the signal amplitude is significantly smaller for $T = 240\,\mathrm{K}$ than for 110 K. This is expected as the signal amplitude A is proportional to the net magnetization M of the sample, which decreases considerably with increasing temperature (cf. Fig. 4.1 (b)). At the same time, the linewidth drastically increases as discussed in the following. These two aspects prevent a reliable analysis of the FMR signal in the temperature region $250\,\mathrm{K} < T < 300\,\mathrm{K}$ (i.e. around the compensation temperature). Therefore, we do not report data in this temperature region. Note that nevertheless, FMR is very well suited to investigate the magnetic properties of the GdIG film selectively, i.e. independent of the substrate, for temperatures below T_{comp}.

The FMR linewidth $\Delta H = \Delta\omega/\gamma$ (Fig. 4.1 (d)) that is extracted from the fit of the raw data can be separated into a inhomogeneous contribution $\Delta\omega_0 = \Delta\omega(H_0 = 0)$ and a damping contribution varying linear with frequency with the slope α (Eq. (1.6)). As opposed to the resonance linewidth of YIG measured in the previous chapter, GdIG does not exhibit a peak-like linewidth maximum at 50 K. In GdIG, the magnetic moments of Gd are collectively coupled to the magnetic Fe sublattice. Hence, they do not show the typical paramagnetic-like relaxation independent of YIG that is required for a temperature peak process. Close to $T_{\mathrm{comp}} = 285\,\mathrm{K}$, the dominant contribution to the linewidth is $\Delta\omega_0$ which increases by more than an order of magnitude from 390 MHz at 10 K to 6350 MHz at 250 K [Fig. 4.2 (c)]. This temperature dependence of the linewidth has been described theoretically by Clogston et al [117, 118] in terms of a dipole narrowing of the inhomogeneous broadening and was reported experimentally before [30, 119]. As opposed to these single frequency experiments, our broadband experiments allow to separate inhomogeneous and intrinsic damping contributions to the linewidth. We find that in addition to the inhomogeneous broadening of the line, also the Gilbert-like (linearly frequency-dependent) contribution to

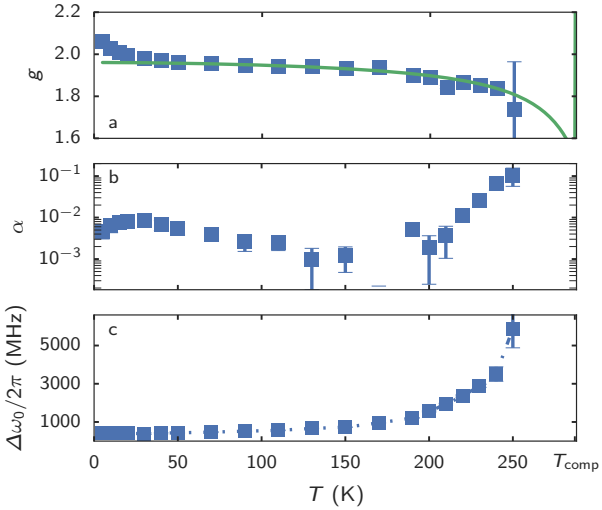

Figure 4.2: Key parameters characterizing the magnetization dynamics of GdIG as a function of T: **(a)** g-factor $g = \gamma\hbar/\mu_B$, **(b)** Gilbert damping constant α and **(c)** inhomogeneous linewidth $\Delta\omega_0/2\pi$. The solid line in panel (a) is the theoretical expectation according to Eq. (4.1). Figure adapted from Ref. [MF7].

the linewidth changes significantly: Upon approaching T_{comp} [Fig. 4.2 (b)], the Gilbert damping parameter α increases by an order of magnitude. Note, however, that due to the large linewidth and the small magnetic moment of the film, the determination of α has a relatively large uncertainty.[2] A more reliable determination of the temperature evolution of α using a single crystal GdIG sample that gives access to the intrinsic bulk damping parameters therefore remains an important task. Nevertheless, the data taken here show for the first time that both the inhomogeneous and the Gilbert damping change qualitatively with temperature.

As all measurements are performed in the high field limit of FMR, the dispersions shown in Fig. 4.1 (c) are linear and we can use the Kittel equation

$$\omega_{\mathrm{res}} = \gamma\mu_0 \left(H_{\mathrm{res}} - M_{\mathrm{eff}}\right) \qquad \text{(1.15 revisited)}$$

to extract γ and M_{eff}. The temperature evolution of the g-factor $g = \gamma\frac{\hbar}{\mu_{\mathrm{B}}}$ is shown in Fig. 4.2 (a).[3] We observe a substantial decrease of g towards T_{comp}. This is consistent with reports in the literature for bulk GdIG and can be explained considering that the g-factors of Gd and Fe ions are slightly different ($g_{\mathrm{Fe}} > g_{\mathrm{Gd}}$) such that the angular momentum compensation temperature is larger than the magnetization compensation temperature [53, 119, 120]. The effective g-factor in this case is given by [119, 121]:

$$g = g_{\mathrm{Fe}} g_{\mathrm{Gd}} \frac{M_{\mathrm{Fe}} - M_{\mathrm{Gd}}}{g_{\mathrm{Gd}} M_{\mathrm{Fe}} - g_{\mathrm{Fe}} M_{\mathrm{Gd}}} \tag{4.1}$$

This model is shown for $g_{\mathrm{Fe}} > g_{\mathrm{Gd}}$ and the calculated sublattice magnetization M_{Gd} and M_{Fe} from Chap. 1 in Fig. 4.2 (a) as solid line.

As noted in Sec. 1.2, is customary to describe the magnetic anisotropy using M_{eff} which can be related to an anisotropy field H_{ani} along $+\hat{z}$ as $M_{\mathrm{eff}} = -H_{\mathrm{ani}} = M_{\perp} - H_{\mathrm{k}}$ for positive H_0. Here, H_{ani} is given by the demagnetization field $H_{\mathrm{shape}} = -M_{\perp}$ (along $-\hat{z}$) and the anisotropy field H_{k} of the additional perpendicular anisotropy (along $+\hat{z}$). Evidently, M_{eff} can be determined by linearly extrapolating the data to $\omega_{\mathrm{res}} = 0$. The FMR dispersion and the fit to Eq. (1.15) (solid lines) are shown for three selected temperatures in Fig. 4.1 (a). At 110 K (blue curve) M_{eff} is positive. Therefore, $M > H_{\mathrm{k}}$ indicating that shape anisotropy dominates, and the

[2] For the given signal-to-noise ratio and the large linewidth, α and $\Delta\omega_0$ are correlated to a non-negligible degree with a correlation coefficient of $C(\mathrm{intercept}, \mathrm{slope}) = -0.967$.

[3] As in Chap. 3, we use the more memorable g-factor instead of γ for the discussion.

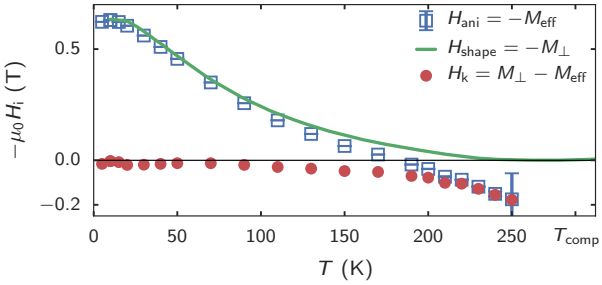

Figure 4.3: Anisotropy field $H_{ani} = -M_{eff}$ as a function of temperature (open squares). Prediction for shape anisotropy H_{shape} based on SQUID magnetometry data (solid line) from Ref. 122. The additional perpendicular anisotropy field $H_k = M_\perp - M_{eff}$ (red dots) increases to approximately 0.18 T at 250 K where its value is essentially identical to H_{ani} due to the vanishing $M_\perp$. Above 190 K, a PMA is observed. Figure adapted from Ref. [MF7].

film plane is a magnetically easy plane while the out-of-plane (oop) direction is a magnetically *hard* axis. At 240 K (red curve) M_{eff} is negative and hence, the oop direction is a magnetically *easy* axis. Figure 4.1 (b) shows the extracted $M_{eff}(T)$. At 190 K, M_{eff} changes sign. Above this temperature (marked in red), the oop axis is magnetically easy (PMA) and below this temperature (marked in blue), the oop axis is magnetically hard (IPA). The knowledge of $M_\perp(T)$ obtained from SQUID measurements allows to separate the additional anisotropy field H_k from M_{eff} (red dots in Fig. 4.1 (b)). $H_k = M_\perp - M_{eff}$ increases considerably for temperatures close to T_{comp} while at the same time, the contribution of the shape anisotropy, $H_{shape} = -M_\perp$, trends to zero. For $T \gtrapprox 180$ K, H_k exceeds H_{shape} which is indicated by the sign change of M_{eff}. Above this temperature, we thus observe PMA. We use the magnetization M determined using SQUID magnetometry from Ref. 122 normalized to the here recorded M_{eff} at 10 K in order to quantify H_k. The maximal value $\mu_0 H_k = 0.18$ T is obtained at 250 K which is the highest measured temperature due to the decreasing signal-to-noise ratio towards T_{comp}.

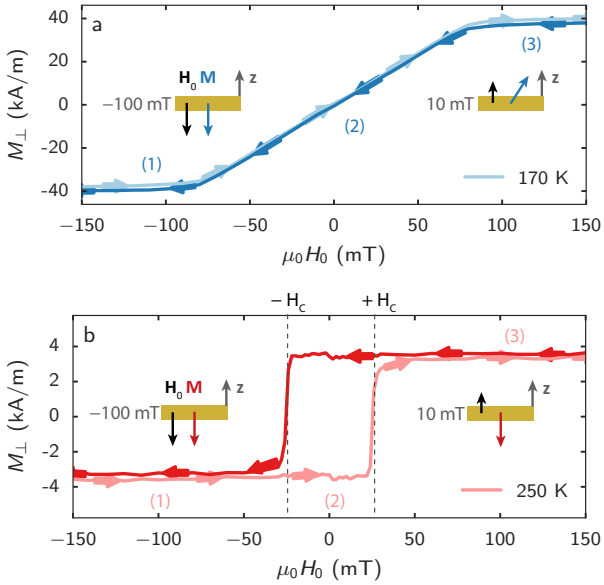

Figure 4.4: Out-of-plane magnetization component $M_\perp$ measured by SQUID magnetometry. For different temperatures, magnetically hard (170K, (a)) and easy (250K, (b)) axis loops are observed. The arrows on the data indicate the sweep direction of H_0. The insets schematically show the magnetization direction $\mathbf{M}$ and $\mathbf{H}_0 = H_0\hat{z}$ with the film normal $\hat{z}$ at the indicated values of H_0. Figure adapted from Ref. [MF7].

SQUID magnetometry

In order to independently confirm the observation of a perpendicular magnetic anisotropy, we perform SQUID magnetometry measurements on the GdIG film. The presented magnetometry measurements have been performed by Stephan Geprägs. SQUID magnetometry measures the projection of the magnetic moment of a sample on the applied magnetic field direction. For thin magnetic films, however, the background signal from the comparatively thick substrate can be on the order of or even exceed the magnetic moment m of the thin film and hereby impede the quantitative determination of m. Our 2.6 µm thick GdIG film is grown on a 500 µm thick GGG substrate warranting a careful subtraction of the paramagnetic background signal of the substrate. In our experiments, H_0 is applied perpendicular to the film plane and thus, the projection of the net magnetization $\mathbf{M} = \mathbf{m}/V$ to the out-of-plane axis is recorded as $M_\perp$. Fig. 4.4 shows $M_\perp$ of the GdIG film as function of the externally applied magnetic field H_0. In the investigated small region of H_0, the magnetization of the paramagnetic substrate can be approximated by a linear background that has been subtracted from the data. The two magnetic hysteresis loops shown in Fig. 4.4 are typical for low temperatures ($T \lesssim 170\,\mathrm{K}$) and for temperatures close to T_comp. The hysteresis loops unambiguously evidence hard and easy axis behavior, respectively. Towards low temperatures ($T = 170\,\mathrm{K}$, Fig. 4.4 (a)) the net magnetization $M = |\mathbf{M}|$ increases and hence, the anisotropy energy associated with the demagnetization field[4] $H_\mathrm{shape} = -M_\perp$ dominates and forces the magnetization to stay in-plane. At these low temperatures, the anisotropy field perpendicular to the film plane, H_k, caused by the additional anisotropy contribution has a constant, comparatively small magnitude. We therefore observe a hard axis loop in the out-of-plane direction: Upon increasing H_0 from $-150\,\mathrm{mT}$ to $+150\,\mathrm{mT}$, $\mathbf{M}$ continuously rotates from the out-of-plane (oop) direction to the in-plane (ip) direction and back to the oop direction again. The same continuous rotation happens for the opposite sweep direction of H_0 with very little hysteresis. For temperatures close to T_comp ($T = 250\,\mathrm{K}$, Fig. 4.4 (b)), H_shape becomes negligible due to the decreasing M while H_k increases as shown below. Hence, the out-of-plane direction becomes the magnetically easy axis and, in turn, an easy-axis hysteresis loop is observed: After applying a large negative H_0 ((1) in Fig. 4.4 (a)), M and H_0 are first parallel. Sweeping to a positive H_0, M first stays parallel to the film normal and hence $M_\perp$ remains constant ((2) in

[4] We use the demagnetization factors of a infinite thin film (cf. Sec. 1.2): $N_\mathrm{x,y,z} = (0,0,1)$

Fig. 4.4 (a)) until it suddenly flips to being aligned antiparallel to the film normal at $H_0 > +H_c$ ((3) in Fig. 4.4 (a)). These loops clearly demonstrate that the nature of the anisotropy changes from IPA to PMA on varying temperature.

Conclusions

In this chapter, we performed bbFMR studies on a GdIG thin film using the setup described in Chap. 2. We analyze the temperature dependence of the FMR linewidth and the g-factor of the GdIG thin film and we find values compatible with bulk GdIG [30, 118]. The linewidth can be separated into a Gilbert-like and an inhomogeneous contribution. We show that in addition to the previously reported increase of the inhomogeneous broadening, also the Gilbert-like damping parameter α increases significantly when approaching T_{comp}. In order to relate this increase in the inhomogeneous linewidth and in α to the change in the magnon-spectrum of GdIG, however, the data is not sufficient yet. Supplementary information is needed as the antiferromagnetic resonance mode could not be observed in this sample and as reliable neutron scattering data that gives the magnon spectrum of GdIG is not available. Another approach, that is currently worked upon, is to conduct bbFMR measurements on a GdIG single crystal in a similar fashion as performed in the previous chapter. In single crystalline GdIG, we expect a narrower linewidth and a higher signal strength (due to the larger volume) and hence observing FMR close to the compensation point and the antiferromagnetic mode of GdIG is possible.

The bbFMR measurements reveal a sign change of the effective magnetization which is in line with the magnetometry measurements and allows a quantitative analysis of the anisotropy fields. We explain the qualitative anisotropy modifications as a function of temperature by the fact that the magnetic shape anisotropy contribution is reduced considerably close to T_{comp} due to the reduced net magnetization, while the additional perpendicular anisotropy field increases considerably. We confirm the findings using SQUID magnetometry. The magnetometry measurements reveal hard axis magnetic hysteresis loops in the out-of-plane direction due to shape anisotropy dominating the magnetic configuration at temperatures far away from the compensation temperature T_{comp}. In contrast, at temperatures close to the compensation point, easy axis magnetic hysteresis loops are observed.

We conclude that by changing the temperature the nature of the magnetic anisotropy can be changed from an in-plane magnetic anisotropy to a perpendicular magnetic anisotropy. Broadband FMR using our setup in combination with SQUID magnetometry proves to be an adequate tool to quantify additional anisotropies in thin magnetic films.

CHAPTER 5

SUMMARY

In this first part of the thesis, we investigated the magnetic properties of two ferrimagnetic insulators using broadband ferromagnetic resonance.

We described the experimental setup, which was assembled as an important part of this thesis, and discussed how reliable and highly sensitive FMR measurements can be performed as a function of temperature. We furthermore presented a novel data analysis method which allows to analyze broadband FMR in frequency space. The method does not require any microwave calibration of the setup and allows to reduce unwanted magnetic background signals without the need for a prior knowledge of the dispersion relation of the material under investigation. Several more conventional data analysis and background removal methods are described and their various optimal use cases are discussed and compared. All presented methods are implemented in an open-source python software library that is discussed in detail in Appendix A.1.

The first sample that we investigated is a single crystal YIG sphere. We performed a broadband temperature-dependent study of the resonance frequency and the linewidth of several magnetostatic modes for the first time. The acquired data allows us to report the magnetization, magnetic anisotropy and g-factor as a function of temperature in detail. The focus of our experiments here, however, is the temperature-dependent damping of YIG. We find that there are two temperature regions with distinctly different frequency dependencies of the linewidth. In the high temperature region ($100\,\mathrm{K} < T < 300\,\mathrm{K}$) a Gilbert-like linear linewidth-frequence dependence

is dominant. In agreement with the measurements and predictions by Kasuya and LeCraw [92] and Cherepanov et al. [45], the Gilbert damping parameter increases towards higher temperatures. In the low temperature region ($5\,\mathrm{K} < T < 100\,\mathrm{K}$) the relaxation of magnetic excitations is dominated by the coupling to impurities. Our data indicates that in our sphere, rare-earth ions are the cause for a linewidth maximum around 40 K. Our systematic and truly broadband FMR experiments thus confirm the notion that slowly relaxing impurities typically dominate the relaxation in this temperature region, established in the literature, and provide a detailed frequency dependence of the linewidth.

The second sample is a GdIG thin film. In its crystal structure, GdIG is very similar to YIG but exhibits magnetization compensation, i.e. a vanishing net remanent magnetization, at around 288 K due to the magnetic moment of the Gd ions. For the GdIG sample too, we performed a study of the temperature-dependent damping. We observe a drastic increase in the linewidth close to the compensation temperature and are able to confirm speculations in the literature that the increase in linewidth is dominantly due to an inhomogeneous broadening. However, we find that also the Gilbert-like damping contribution increases by several orders of magnitude close to the compensation temperature, an effect hitherto unknown. Another very interesting finding is that the nature of the anisotropy of YIG changes towards the compensation temperature. The usual easy plane anisotropy due to the shape anisotropy of the thin film gets negligible with the decreasing net magnetization towards the compensation point. At the same time, an additional anisotropy, presumably of cubic magnetocrystalline origin, increases and gives rise to a perpendicular magnetic anisotropy. Such a perpendicular magnetic anisotropy is of considerable interest as it may enable optical and spin torque switching experiments in a magnetic insulator.

PART II

CAVITY FMR

Table of Contents

INTRODUCTION

Broadband ferromagnetic resonance with planar waveguide structures as discussed in the previous chapter is a comparably new technique mainly developed in the early 2000's [70, 123–126]. In contrast, magnetic resonance experiments using 3D waveguides or 3D cavities to create a microwave magnetic field at the sample position have been performed in the 1940's already [127, 128]. Both, 3D waveguides and cavities, however, hold their particular advantages and are thus still relevant today:

Three-dimensional waveguides allow to perform magnetic resonance in a frequency band of several gigahertz [15]. By placing the sample under investigation at an off-center position, they furthermore provide an easy method to generate circularly polarized microwaves [129]. This method, which allows to determine the absolute sign of the g-factor of a magnetic specimen, was implemented and optimized by Sho Watanabe in his master project [129] whom I supervised as part of this doctorate.[1] Three-dimensional microwave cavities, on the other hand, exhibit discrete standing modes, given by the geometry and the employed dielectric materials of the cavity. Typically, one specific mode is selected for a given experiment and hence, the microwave frequency is fixed to a certain value, the cavity resonance frequency ω_c. A sample in the cavity therefore experiences a different density-of-states for photon emission as compared to free space. At all frequencies except ω_c, the relaxation of the magnetic system via emission of a photon to the cavity is therefore heavily suppressed. In total, radiation damping losses can be reduced to the cavity decay rate [39, 130, 131]. Furthermore, the often inevitable inhomogeneous broadening of a macroscopic magnetic sample's magnetic resonance can be effectively

[1] We will not discuss this work in the following but refer the reader to the excellent master's thesis of Watanabe [129] for a detailed discussion of the method.

suppressed [132] due to the interaction of the moments via the cavity. These intriguing features have been employed to protect qubits in a cavity against decoherence [133, 134] and are one of the key aspects of a proposal to detect dark matter via its interaction with a magnetic sample [131] showing the versatility of cavity based magnetic resonance. Microwave cavities furthermore allow to separate the magnetic and electric microwave field and can be used to create a very homogeneous microwave magnetic field at the sample position [68]. This attribute allows to suppress the generation of DC currents due to microwave rectification in conducting samples. It is therefore of particular interest when aiming for an electrical detection of magnetic resonance as in Chap. 7.

Moreover, the coupling and hybridization of spin excitations such as magnons with cavity photons is an intriguing effect by itself. It is the basis for the concept of hybrid quantum information systems that combine the fast manipulation rates of superconducting qubits and the long coherence times of spin ensembles. Achieving a strong spin excitation–microwave photon coupling, i.e. a coupling rate that exceeds the individual relaxation rates, and thereby achieving coherent information exchange between the two systems is therefore a major goal of quantum information memory applications. Coherent information exchange between microwave photons and a spin ensemble was initially demonstrated for paramagnetic systems [135, 136] and has since been employed in a number of experimental schemes [134, 136–139]. Only recently, this concept has been transferred to magnetically ordered systems where the coupling rate of the magnetic excitations (magnons) to the cavity is boosted by the large spin density of the materials. Coupling rates of hundreds of megahertz can therefore be achieved [36, 38, 140–142]. Utilizing the flexibility of exchange coupled magnetically ordered systems, more complex architectures involving multiple magnetic elements have already been developed [37, 40]. Additionally, magnetically ordered systems allow to study and utilize classical strong coupling physics even at room temperatures [36, 37, 40, 141, 143].[2]

In the following, we use the two materials YIG and GdIG, which we introduced and characterized in detail in the first part of the thesis, to study the magnon-photon coupling of iron garnet materials with a standard electron paramagnetic resonance cavity resonator. In a first experiment we aim to experimentally proof that, in analogy to the paramagnetic case, the magnon-photon coupling rate scales with the square root of the magnetiza-

[2] This paragraph is adapted from Ref. [MF2].

tion M for magnetically ordered systems. To this account, we quantitatively evaluate the coupling rate of a GdIG sample and a microwave cavity resonator as a function of temperature, utilizing the temperature dependence of the magnetization of GdIG to transition between weak and strong coupling. This task is challenging because the evaluation needs to be robust for the weak, intermediate and strong coupling regime and hence the typically employed approximative models cannot be used. It, however, also allows to showcase the signature of magnon-photon coupling in different coupling regimes and to evaluate GdIG for the use in experiments similar to the ones mentioned above. In a second experiment, we examine the coupling of a YIG sample to the same microwave cavity. With the high spin density and the exceptionally low damping of YIG, strong coupling can easily be reached with typical micrometer thick film samples. Using a thin film allows to study the coupling of perpendicular standing modes to the cavity and allows to again evaluate the scaling of the coupling strength as the dynamic magnetization the couples to the cavity is expected to be decreased for higher order modes. A further advantage of using a thin film is that a bilayer of a YIG layer and a metal (platinum) layer can be produced with a high quality interface. Such bilayers allow the transfer of spin currents from the ferromagnet to the metal layer, a process called spin pumping. Utilizing the inverse spin Hall effect in the metal layer, the spin current can be detected electrically. Establishing spin pumping in strongly coupled systems is the first step on the way to electrically detecting the magnon state in hybrid photon–magnon systems. Such an independent readout channel is advantageous for the above introduced applications in (quantum) information processing and transfer.

The following chapter is organized as follows: We first give a brief introduction to the concept of microwave cavities with a particular focus on the TE_{011} mode of cylindrical cavities that we employ in the following experiments. In Sec. 6.3, we then present a detailed study of the coupling mechanism of a microwave cavity with a compensating ferrimagnetic insulator. In this section, we extract the scaling of the coupling rate with the magnitude of the ferrimagnets magnetic moment and show that reaching the so-called strong coupling regime is easily possible using this particular hybrid system. In Chap. 7, we investigate the electrical readout of magnetic excitations using spin pumping in a ferrimagnet–microwave cavity hybrid system. In this chiapter, we show that the effect of spin pumping is still observed in the strong coupling regime and follows the theoretical predic-

tions. Finally, Chap. 8 briefly summarizes the results of both experimental studies.

CHAPTER 6

MAGNON-PHOTON COUPLING IN THEORY AND EXPERIMENT

In order to investigate the magnon-photon coupling of a cavity resonator loaded with a magnetic sample, the characteristic eigenmodes of the system need to be determined. This can be achieved either by measuring the frequency-dependent transmission of microwaves through the loaded cavity or the reflection of microwaves at the cavity. In the following, we use a one-port approach, in which the cavity is coupled capacitively to a single microwave cable, the so-called cavity feed line. This approach allows to read out the resonant modes of the system via the frequency-dependent microwave reflection at the cavity. High reflected microwave power indicates that at the given frequency no resonant mode can be excited. Low reflected power indicates that some resonant mode is excited by the incident power which is then partially dissipated in the cavity or the sample.

6.1 Experimental details

The complete setup to record this type of spectra is schematically displayed in Fig. 6.1. It consists of a cryostat (1), the sample rod (not shown) and sample holder (2) that insert the sample (4) into the microwave cavity (3).

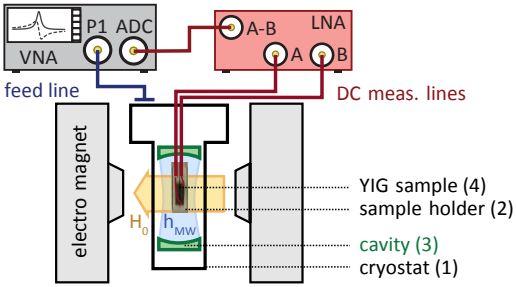

Figure 6.1: Block diagram of the experimental setup including low-noise voltage amplifier (LNA), vector network analyzer (VNA) and sample mounting. The loaded cavity is shown schematically in Fig. 7.2, the sample holder is shown in Fig. 6.3

The assembly is mounted in-between the pole shoes of an electromagnet. The microwave cavity is connected to a vector network analyzer (VNA) that measures the complex microwave reflection parameter S_{11}. The DC leads to the sample are connected to a low-noise voltage amplifier (LNA) whose output, in turn, is measured by the VNA as a function of the applied microwave power and frequency.

The cavity that we use is a commercially available Bruker Flex-line MD5 dielectric ring cavity (ER 4118X-MD5) typically used for pulsed electron paramagnetic resonance. In our experiments, we use the cavity's TE_{011} mode. Fig. 6.2 shows the mode profile of the TE_{011} mode of a simple cylindrical cavity with air as the dielectric.[1] The electric field exhibits a node in the center of the cavity, whereas the magnetic field exhibits an anti-node at the same position. The sample is placed on a non-metallic sample holder in the center of the cavity. Since it is hence positioned in the center of the magnetic field anti-node, it experiences a very homogeneous magnetic field and ideally zero electric field. By careful placement, microwave rectification effects that lead to unwanted DC currents flowing in conducting samples can thereby be reduced. The resonance frequency of the cavity is given by its geometry and the dielectric constant of the materials used in the

[1] Dielectric ring cavities are slightly more complex and contain a ring of a dielectric material with a high dielectric constant near the walls of the cavity. This concentrates the electric field in this ring and the magnetic field in the center of the cavity [144]. The mode profile is, however, very similar to the one of a simple cylindrical cavity as in Fig. 6.2.

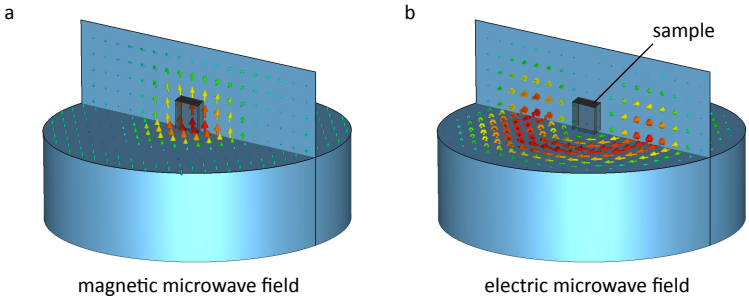

Figure 6.2: Magnetic (a) and electric (b) field distribution of the TE_{011} mode of the dielectric ring cavity simulated using the finite element modeling software `CST Microwave Studio` (not to scale). At the indicated sample position, the electric microwave field has a node while the magnetic field has an anti-node.

cavity. Our cavity is designed such that it operates in the microwave X-band with a resonance frequency of the TE_{011} mode of $\omega_c/2\pi \approx 9.6\,\mathrm{GHz}$.

An important figure of merit of any microwave resonator is its quality factor Q_c which is given by

$$Q_c = \frac{\omega_c}{\Delta\omega} = \frac{\omega_c}{2\kappa_c} = \frac{\omega_c}{2\left(\kappa_c^{int} + \kappa_c^{ext}\right)} = \left(1/Q_c^{int} + 1/Q_c^{ext}\right)^{-1} \tag{6.1}$$

with the cavity relaxation rate (half width half maximum linewidth) $\kappa_c = 2\Delta\omega$. Q_c is determined by the cavity's internal and external loss rates κ_c^{int} and κ_c^{ext} and is expressed with internal and external quality factors Q_c^{int} and Q_c^{ext}. Internal losses are due to dielectric heating and ohmic heating in the cavity walls. External losses are due to the coupling to the feed line that is needed to excite and read out the cavity. In our case, the cavity is coupled capacitively to the microwave feed line and κ_c^{ext} can be controlled by mechanically adjusting the coupling mechanism.

Typically, for magnetic resonance spectroscopy, the cavity–feed line coupling is adjusted so that the characteristic impedance of the cavity equals the characteristic impedance of the feed line ($50\,\Omega$). This so-called critical coupling leads to optimal power transfer from and to the cavity and hence maximum sensitivity to the magnetic resonance signal. The external losses and internal losses are then of equal magnitude $\kappa_c = \kappa_c^{int} + \kappa_c^{ext} = 2\kappa_c^{int}$. For experiments where a broad cavity linewidth (and thus a high κ_c and low Q_c) is the limiting factor, up to a factor of 2 can be gained in decay

rate at the expense of the signal-to-noise ratio by reducing the cavity–feed line coupling (undercoupling). In contrast, when the cavity is loaded with a large piece of magnetic material and the cavity linewidth is narrow (low κ_c), effects of strong coupling can appear that compromise the experimental results of the typical fixed-frequency magnetic resonance experiments. These effects can be reduced by increasing the cavity–feed line coupling (overcoupling) and thus increasing κ_c^{ext}. We use this control over κ_c^{ext} in Chap. 7 to investigate the characteristic behavior of the ferrimagnet–cavity system for different ratios of the magnon–photon coupling rate, and the cavity and magnon relaxation rate. In Sec. 6.3, we take a different approach and keep the cavity critically coupled to the feed line but vary magnon–photon coupling rate by tuning the total magnetization of the sample by means of changing the temperature.

To achieve the necessary temperature control, the cavity and the coupling mechanism are placed in the sample space of an Oxford CF 935 gas continuous flow cryostat. In contrast to the cryostat used in Part I, the CF 935 cryostat here does not feature a superconducting magnet and has no reservoir for the liquid helium or nitrogen. Instead, either liquid helium or nitrogen is supplied directly from an external storage vessel to the cryostat using an insulated transfer tube. By opening or closing a needle valve in the transfer tube, the flow rate and hence the available cooling power can be adjusted. In the cryostat, the helium or nitrogen flows through a heat exchanger below the sample space. The heat exchanger is equipped with a heater and a temperature sensor. Using a PID control loop, the temperature of the gas and hence the temperature of the cavity and sample can be controlled and stabilized. In the experiments, we employ both helium and liquid nitrogen for cooling. Both gases work equally well in terms of cooling power and temperature stability. We therefore do not distinguish between experiments performed using the one or the other gas. The cryostat has a small diameter and can hence be mounted in-between the pole shoes of an water cooled electromagnet. This allows quick ramping of the magnetic field and very small field steps (cf. Chap. 2) which will be necessary for the investigation of the standing spin wave modes of YIG in Chap. 7 which exhibit a very small resonance linewidth. However, the pole shoe gap of approximately 6 cm limits the maximal magnetic field that can be generated to approximately 300 mT when the coil current is supplied by a Kepco BOP 20-20M power supply and to approximately 1 T, when a Lakeshore 643 power supply is used. Note that upon decreasing the temperature of the cavity, the resistivity and the dielectric losses of the

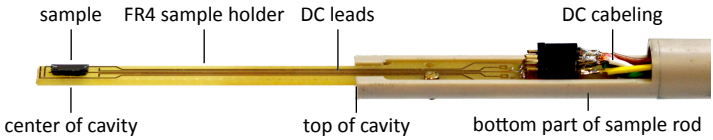

Figure 6.3: Bottom part of the sample rod (gray) with mounted sample holder (yellow). When fully inserted, the sample rod rests on top of the cavity and the sample is placed in the center of the cavity. A thin film sample is mounted on the sample holder and connected with bond wires to the DC leads.

materials used in the cavity typically decrease. Due to this decrease of the internal losses, one expects a decrease of the total linewidth of the cavity with decreasing temperature. However, the thermal contraction of the setup and the resulting change in the cavity resonance frequency, requires to readjust the coupling mechanism at each temperature in order to maintain critical coupling. As this manual adjustment is usually not perfect, also the external losses vary slightly from temperature to temperature. The change in linewidth due to the temperature-dependent decrease of the linewidth is small compared to the change upon readjusting the cavity–feed line coupling. Furthermore, we do not observe a systematic decrease of κ_c with decreasing temperature and therefore take the cavity relaxation rate to be approximately constant over temperature in the following.

In order to change or reposition the sample quickly without the need to warm up the whole system, a sample rod that supports the sample on its holder is inserted into the cryostat and sealed against ambient atmosphere by an O-ring. When fully inserted, the bottom of the sample rod rests on top of the microwave cavity and extends to an interchangeable sample holder that is inserted into the center of the cavity. For typical EPR experiments, the sample holder is a quartz glass tube that contains the magnetic specimen. For the electrical detection using spin pumping, electric leads to the sample need to be added to the setup. To achieve this, a sample holder consisting of a FR4 printed circuit board and a matching new sample rod has been designed and constructed. The lower part of the sample rod that inserts into the cavity is shown in Fig. 6.3. It was ensured that the metal DC leads reaching into the cavity and the FR4 IT158 (Tg155) substrate material do not overload and distort the cavity mode or cause a large magnetic

background. The sample rod details and drawings are available freely under the CERN open hardware license.[2]

The cavity feed line is connected via microwave cable with SMA connectors to a Agilent/Keysight N5242A PNA-X VNA that measures the complex reflection parameter S_{11} as a function of the microwave probe frequency. After each complete frequency sweep, S_{11} is automatically recorded on a control computer. Using the same computer, an electromagnet can be set to generate a specific fixed magnetic field H_0 at the sample location. The magnetic field is measured and stabilized by an Hall effect sensor which is placed between the pole shoes of the magnet at ambient temperature next to the cryostat. In this way, it is possible to record the field and frequency dependence of S_{11}, thereby mapping out the resonant modes of the system. In contrast to broadband FMR, where the FMR modes are observed directly, here, we observe the cavity mode and its field-dependent distortion due to the magnetic material. A field-frequency map of S_{11} in a frequency band centered around the cavity resonance frequency is needed in order to investigate the coupling of an FMR mode with the cavity mode. The probe power is kept low enough so that no non-linear effects are observed. For ferromagnets, this is typically given when the average number of photons in the cavity is much smaller than the total number of spins in the sample. We ensure that this is the case separately for each of the experiments in Sec. 6.3 and Chap. 7. Due to impedance mismatches at the connectors, it is unavoidable that standing waves form in the feed line and the SMA cabling. For a quantitative analysis, the signal of interest has to be separated from this complex background signal which will be discussed in Sec. 6.2.1.

The field and frequency dependence of a DC voltage generated at the sample can also be measured in the setup. For this, we connect the leads of the sample holder to a Stanford Research Systems LNA model 560 and amplify the differential ("$A - B$") voltage between the two ends of the sample. The amplified signal at the output of the amplifier (0 to 10 V) is then fed into the auxiliary input channel of the VNA and is recorded simultaneously to S_{11} as a function of the microwave frequency. Limiting the bandwidth of the amplifier by filtering is required in order to achieve a good signal-to-noise ratio. The amplifier is equipped with analog high- and low-pass filters that can be used for this task. Care has to be taken, however, as the lineshape may be quickly distorted by inappropriate settings and

[2] The detailed design blueprints and bill of materials of the sample rod and the sample holder are published at http://hannes.maier-flaig.de/flexline-sample-rod.

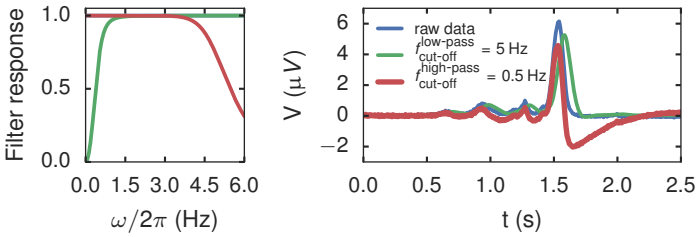

Figure 6.4: Effect of high- and low-pass filtering on the DC voltage signal when recording the signal as a function of frequency with a VNA. **(a)** Filter response of a 0.5 Hz high-pass Butterworth filter 2nd order (green) and a 5 Hz low-pass Butterworth filter of 6th order (red). **(b)** Typical voltage signal as a function of time during a frequency sweep with IF bandwidth 100 Hz displayed for the filters of (a) and without filtering (blue).

thus the signature of spin pumping might be masked. The VNA sweeps the microwave frequency at a rate comparable to the intermediate frequency (IF) bandwidth chosen for a certain measurement. Even though the voltage signal that is detected is a DC signal when the microwave drive has a constant frequency, the voltage signal recorded for such a frequency sweep will naturally vary with time. A typical example of experimental voltage signal for a frequency sweep with an IF bandwidth of 100 Hz, leading to a total sweep time of 2.6 s, is shown in Fig. 6.4 (b). The signal varies with a frequency of around 0.5 Hz for these settings. A digital high-pass filter with a cut-off frequency of $f_{\text{cut-off}}^{\text{high-pass}} = \omega_{\text{cut-off}}^{\text{high-pass}}/2\pi = 0.5\,\text{Hz}$ [Fig. 6.4 (a)] is applied to the data (red line in Fig. 6.4 (b)). It shows that high-pass filtering leads to a dispersive-like contribution to the signal that can be mistaken for rectification effects that exhibit the same characteristic lineshape. Low-pass filtering (the green lines in Fig. 6.4 show a low-pass filter with the cut-off frequency $\omega_{\text{cut-off}}^{\text{low-pass}}/2\pi = 5\,\text{Hz}$) will give rise to asymmetric line shapes and a shift of the peak positions depending on the ratio of IF bandwidth and low-pass frequency. For the electrical detection performed in Chap. 7, it was ensured that the filter band is chosen such that the signal is not distorted. The detailed filter settings used in the experiment are noted in Chap. 7.

6.2 Signature and theory of magnon-photon coupling

The theoretical description using the theory of Cao et al. [145] in this section is based our publication Ref. [MF3], from which parts of the text are adapted and used here. The description of the harmonic oscillator model, using the input-output formalism and the analysis model following Herskind et al. [146] are based on Ref. [MF2]. Also from this reference, some smaller parts of the text are adapted and used in the following.

The theoretical description of the effects of the coupling between an ordered ferromagnet and a microwave cavity resonator have been discussed in various publications [39, 140, 141, 143, 145]. The most basic description of the coupling of any resonant systems is, however, to regard the system simply as two coupled harmonic oscillators. The phenomenology of coupled harmonic oscillators can be found in most introductory physics text books and already describes main features of a magnon-photon system at high temperatures and low excitation powers quantitatively. A derivation can for example be found in Ref. [147] and gives a dispersion of the hybrid system of

$$\omega_{\pm} = \omega_{\mathrm{c}} + \frac{\Delta}{2} \pm \frac{1}{2}\sqrt{\Delta^2 + 4g_{\mathrm{eff}}^2}. \tag{6.2}$$

Here, ω_{c} is the resonance frequency of one oscillator (which represents the constant cavity resonance frequency in the following discussion), Δ is the frequency detuning of the two oscillators and g_{eff} is the effective coupling rate.

Equation 6.2 describes an anti-crossing of the dispersion of the two oscillators when one of the dispersions is tuned across the other via an external control parameter, e.g. H_0. This signature is shown in Fig. 6.7 (a). Note that the presence of strong coupling and hence a visible anti-crossing of the dispersion relations requires a sufficiently fast coupling rate, i.e. the effective coupling rate g_{eff} needs to exceed the individual loss rates κ_{c} and κ_{s} of the two oscillators. In the above equation, this is implicitly assumed and hence, only the strong coupling case can be described with Eq. (6.2). The dispersion of the hybrid system allows to directly read of g_{eff}, which is given by the half splitting at the so-called degeneracy field H_{deg}, the value of H_0 at which the unperturbed dispersions (dashed lines in Fig. 6.7 (a)) cross.

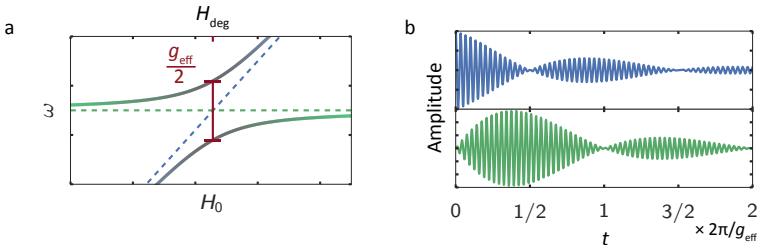

Figure 6.5: Coupling of two subsystems. **(a)** Dispersion of two coupled harmonic oscillators according to Eq. (6.2) (solid lines). The dashed lines are the dispersion of the unperturbed systems. In the example, only the blue oscillator's frequency is tuned by adjusting H_0. **(b)** Step response of the damped coupled system after excitation of one oscillator. After the time $t = 2\pi/(2g_{\mathrm{eff}})$, the excitation is transfered completely to the second subsystem.

It is instructive to discuss the coupling of the two systems in the time domain instead of the frequency domain. When only one oscillator (either the magnetic system or the cavity) is excited, after the time $2\pi/(2g_{\mathrm{eff}})$, the excitation is transfered completely to the other oscillator. After another $2\pi/(2g_{\mathrm{eff}})$, the excitation is transfered back completely and the first oscillator is excited again. At the same time, the two systems experience relaxation (and dephasing) and hence, the oscillations are damped on a time scale of $1/\kappa_{\mathrm{c}}$ and $1/\kappa_{\mathrm{s}}$. If either of the relaxation rates is large, the excitation relaxes predominantly in this systems. The strong coupling regime, which allows coherent transfer of excitation between the systems, is hence intuitively reached if this transfer of excitation between the oscillators can be performed multiple times which gives the criteria $g_{\mathrm{eff}} > \kappa_{\mathrm{c}}, \kappa_{\mathrm{s}}$. This case is illustrated in Fig. 6.5 (b).

In the following we will describe the coupling of the FMR modes of a ferromagnet with cavities. Note, however, that the concept of hybridizing modes is not restricted to this case but is much more general and occurs in many physical system. It reaches from mechanical systems like the famous coupled pendulums to plasmonics. In solid state physics in particular, the characteristic anti-crossing of hybridizing modes can often be observed directly or by its indirect influence on the physical properties and therefore the coupling needs to be taken into account. In Chap. 3, we explicitly excluded the low field region of the YIG spectra from the linewidth and dispersion analysis. In this region, shown as a zoom-in in Fig. 6.6, we

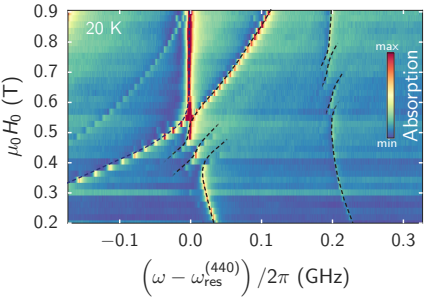

Figure 6.6: The modified dispersion of magnetostatic modes in imperfect spheres is an example of the effect of hybridization of modes. Shown is a zoom-in to the low field region of Fig. 3.8. The dotted lines are a guide to the eye.

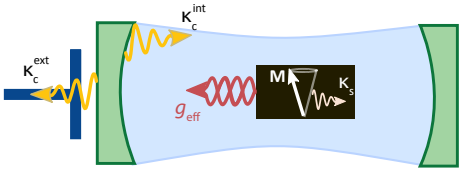

Figure 6.7: Schematic of the coupling of a microwave cavity (green) and the magnetic sample (black). Illustrated are the cavity decay due to intrinsic losses (κ_c^{int}) and losses to the feed line (κ_c^{ext}), the magnon decay (κ_s) as well the collective coupling rate g_{eff}.

observe the hybridization of multiple magnetostatic modes. For an ideal spherical specimen with a vanishing surface roughness, the magnetostatic modes are linearly independent and are hence they are not expected to hybridize. In a real sample, however, the effects of the coupling always play a role and hence, the linewidth and resonance frequency in this region reflects the properties of the hybrid systems instead of the intrinsic YIG properties. Note that also modes that have a very low excitation efficiency and hence do not show as absorption lines in the field-frequency map, affect the dispersion of the other (excited) modes.

The general dispersion of two coupled harmonic oscillators is adapted for a ferromagnet–cavity system by including the field-dependent FMR dispersion in the frequency detuning $\Delta = \omega_s(H_0) - \omega_c \approx \gamma\left(\mu_0 H_0 - \mu_0 H_{\mathrm{deg}}\right)$ with H_{deg} satisfying the magnon resonance condition for a given cavity

frequency $\omega_c = \omega_s$. Conventionally, ferromagnetic resonance (FMR) is modeled in terms of the Landau-Lifshitz-Gilbert (LLG) equation as described in Sec. 1.2. In the following, we will only consider the case when the magnetic field H_0 is applied perpendicular to the interface normal (i.e. in the interface plane) as this configuration is required to measure spin pumping (Chap. 7) electrically [18, 66, 148, 149]. In this case, the magnon dispersion of the uniform FMR mode $\omega_s(H_0)$ is given by:

$$\omega_s = \frac{\gamma}{2\pi}\mu_0\sqrt{H_0\,(H_0+M_{\text{eff}})}. \qquad \text{(1.14 revisited)}$$

As shown explicitly in Chap. 4, the effective magnetization $M_{\text{eff}} = M - H_{\text{ani}}$ is equal to the magnetization M of the magnetic specimen when shape anisotropy is the only relevant contribution to the magnetic anisotropy. H_{ani} accounts for additional anisotropies such as magnetocrystalline anisotropy or strain induced anisotropy. Contrary to ω_s, the resonance frequency ω_c of a cavity resonator is determined by geometrical and dielectric parameters only and therefore usually does not depend on the magnetic field. Since the magnonic mode (magnetization excitation) and the photonic mode (cavity excitation) interact on resonance, we expect modifications to the pure FMR and the pure cavity dispersions as described above.

This description given above is purely classical or rather, purely phenomenological for the classical case. In the scope of the quantum mechanical Tavis-Cummings model [150, 151], hybrid systems of many, non-interacting (paramagnetic) spins and cavity photons can be described even for low spin and low photon numbers. As all our experiments are conducted at fairly elevated temperatures, at which quantum mechanical effects do not play a role, a classical picture is sufficient. From the above description, only the dispersion of the system can be deduced. This is sufficient to describe strongly coupled systems, for which extracting g_{eff} using the splitting of the anti-crossing is reliably possible. In the following, we explicitly study the transition from the weak coupling case to the strongly coupled case. A model that describes the system in the weak, intermediate and strong coupling regime and that allows to experimentally extract the characteristic rates using microwave spectroscopy is therefore needed.

The field and frequency-dependent reflection of the coupled system can be modeled using the input-output formalism [151–154] or with a first-principles theory starting from Maxwell's equations [145]. Both approaches, of course, give the same result in the classical limit. The reflected

microwaves expressed as S_{11} parameter, the ratio of the reflected and the incident microwave voltage ($S_{11} = V_{\text{reflected}}/V_{\text{incident}}$) is given by

$$S_{11} = 1 + \frac{S_{11}^0 \kappa_c^{\text{ext}}}{i(\omega - \omega_c) - \kappa_c - i g_{\text{eff}}^2 (\omega - \omega_s + i\kappa_s)^{-1}}. \tag{6.3}$$

Here, the dimensionless, complex-valued parameter S_{11}^0 accounts for losses and phase shifts in the cavity feed line, κ_c and κ_s are the relaxation rates of cavity and spin system, respectively, as introduced in Sec. 6.1 (i.e. the half width at half maximum frequency line width).

When the external magnetic field is adjusted to tune the FMR frequency ω_s close to the unperturbed cavity frequency ω_c, the excitations of the magnetic system (magnons) and the microwave cavity (photons) start hybridizing with a signature in S_{11} described by Eq. (6.3). We first discuss the strongly coupled case again, which is shown in Fig. 6.8 (a_i) for $g_{\text{eff}} = 2\pi \cdot 100\,\text{MHz}$, $\kappa_c = \kappa_s = 2\pi \cdot 50\,\text{MHz}$ and typical parameters for the FMR dispersion and a typical cavity frequency. Note that the coupling rate exceeds the relaxation rates ($g_{\text{eff}} > \kappa_c, \kappa_s$), indicating strong coupling. The characteristic anti-crossing of the H_0-independent cavity mode and the H_0-dependent spin resonance dispersion as shown in Fig. 6.7 (a) is immediately obvious. The clearest indication of this anti-crossing is the emergence of two separate peaks in a line cut at H_{deg}. The minimal splitting of the absorption peaks occurs at H_{deg} and gives $2g_{\text{eff}}$. Therefore, tracing the peak position can be used to reliably determine the coupling rate g_{eff}.

In the weak coupling regime shown in Fig. 6.8 (d_i), where $g_{\text{eff}} < \kappa_c, \kappa_s$, the cavity mode is only marginally disturbed. Here, the coupling rate can be determined by analyzing the change in the line width of the microwave cavity for each H_0 [146] as described below. This case is equivalent to conventional cavity FMR, where effects of strong coupling are avoided by choosing small or diluted samples and the microwave response is recorded at the cavity frequency only. Therefore, plotting the S parameter at ω_c as a function of H_0 (Fig. 6.8 (d_1)) shows the typical FMR absorption line shape (red dotted line) which is given by Eq. (1.16).[3]

In Fig. 6.8, also the two cases where only one of the relaxation rates is significantly higher than g_{eff} are shown. In case with $\kappa_c > g_{\text{eff}} > \kappa_s$ (panel c_i), the excitation predominantly decays in the cavity system. This

[3] Note that for standard cavity magnetic resonance measurements at fixed frequency, a field modulation technique is typically employed and hence, the field derivative of the signal is recorded.

regime is uncommon as only few materials feature a damping as low as YIG, while the producing high quality cavities is comparatively easy. It is also called the regime of magnetically induced transparency (MIT) [36]. Note that this naming suggests a non-existing close relation to electromagnetically induced transparency, which, however, requires a third level that can be (de)populated using an additional stimulus with a different frequency than the microwave probe frequency ω. When $\kappa_s > g_{\mathrm{eff}} > \kappa_c$ (panel b_i), the so-called Purcell regime, the opposite is the case and the spin relaxation dominates the relaxation of the hybrid system. The naming is based on the Purcell effect which, in this system can be used to describe the increase in the cavity relaxation rate due to the coupling to the magnonic system.

In ferromagnetic films, apart from the uniform FMR mode, additional magnetic modes, so-called perpendicular standing spin waves modes, appear due to magnetic boundary conditions much like the magnetostatic modes observed in the sphere in Chap. 3. The dynamic magnetization forms a standing wave over the film thickness and is labeled with the mode number n, which represents the number of anti-nodes of the mode. The theory of Cao et al. [145] covers these modes explicitly. The gist of the theory is that every mode couples individually with a different coupling strength $g_{\mathrm{eff}}^{(n)}$ to the cavity. When the modes are closely spaced in field and the coupling is large, the modes couple to the already hybridized magnon-photon system of the cavity and the other modes. We will treat this case in Chap. 7 in more detail, where we will use perpendicular standing spin waves of a YIG film to observe spin pumping simultaneously in the strong and in the weak coupling regime.

6.2.1 Evaluation methods

The analysis of the measurement data can be challenging, e.g. when a background signal caused by standing waves in the microwave cabling connecting the cavity and the VNA is superimposed onto S_{11}. Also, often multiple FMR modes like the aforementioned PSSWs exist in the material and need to be taken into account.

Two Lorentzian fits (strong and high cooperativity coupling)

As mentioned before, the simplest method of estimating g_{eff} is to evaluate the frequency splitting of the anti-crossing at the field of degeneracy. A slightly more accurate approach is to fit a composite model of two

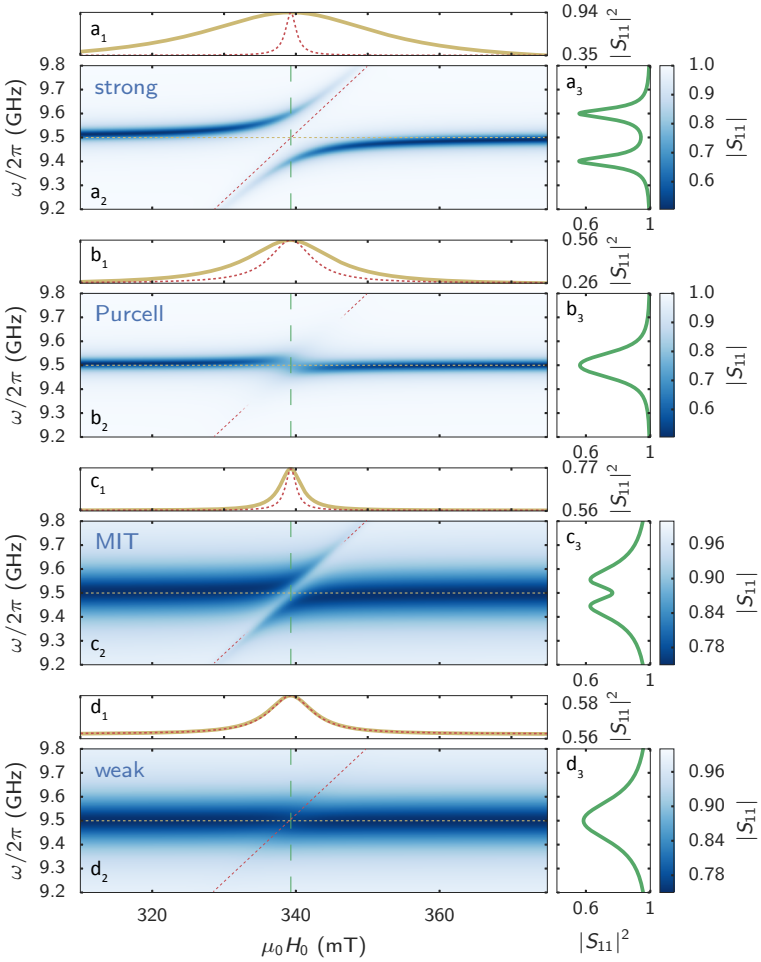

Figure 6.8: Simulation of S_{11} of a ferromagnet–cavity hybrid system according to Eq. (6.3). The dotted lines represent the unperturbed cavity with $\omega_c/2\pi = 9.5\,\mathrm{GHz}$ (orange) and the unperturbed spin system (red) with $\gamma/2\pi = 28\,\mathrm{GHz\,T^{-1}}$ and $M_{\mathrm{eff}} = 0$. **(a)** Strong coupling $g_{\mathrm{eff}} = 2\pi \cdot 100\,\mathrm{MHz} > \kappa_c, \kappa_s$. **(b)** Purcell regime, $\kappa_s = 2\pi \cdot 100\,\mathrm{MHz} > g_{\mathrm{eff}} = 2\pi \cdot 50\,\mathrm{MHz} > \kappa_c = 2\pi \cdot 25\,\mathrm{MHz}$. **(c)** MIT regime, $\kappa_c = 2\pi \cdot 100\,\mathrm{MHz} > g_{\mathrm{eff}} = 2\pi \cdot 50\,\mathrm{MHz} > \kappa_s = 2\pi \cdot 25\,\mathrm{MHz}$. **(d)** Weak coupling, $g_{\mathrm{eff}} = 2\pi \cdot 25\,\mathrm{MHz} < \kappa_c, \kappa_s = 2\pi \cdot 100\,\mathrm{MHz}$. Line cuts: Cuts at ω_c (a_1, b_1, c_1, d_1) and at H_{deg} (a_3, b_3, c_3, d_3) (along the dashed green lines) of the adjacent colorplot.

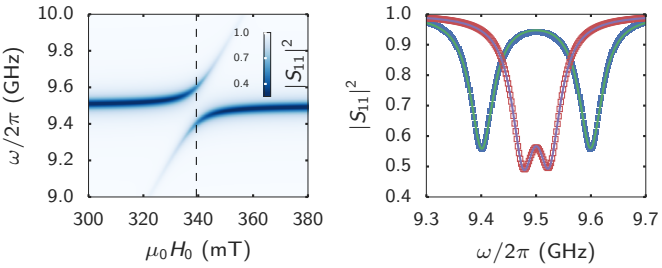

Figure 6.9: Strongly and intermediately strong coupling can be modeled by fitting two Lorentzian distributions. **(a)** S_{11} parameter simulated according to Eq. (6.3) with $\kappa_c/2\pi = 25\,\text{MHz}$, $\kappa_s/2\pi = 25\,\text{MHz}$ and $g_{\text{eff}}/2\pi = 100\,\text{MHz}$. **(b)** Cuts of S_{11} of (a) at degeneracy field indicated with the dashed line in (a) (blue symbols). Same cut of S_{11} of a more weakly coupled system with $\kappa_c = \kappa_s = g_{\text{eff}} = 2\pi \cdot 25\,\text{MHz}$ is shown as red symbols. The solid lines are fits to Eq. (6.4).

Lorentzian distributions to the square of the absolute-value of a cut of S_{11} at H_{deg}:

$$|S_{11}(\omega)|^2 = 1 - \text{L}_1(\omega) - \text{L}_2(\omega) \tag{6.4}$$

with

$$\text{L}_j(\omega) = \frac{a_j \kappa_j^2}{\kappa_j^2 + (\omega - \omega_{0,j})^2} \tag{6.5}$$

which contains the amplitude a_j the center frequency $\omega_{0,j}$ and the HWHM linewidth κ_j. The difference of $\omega_{\text{center},i}$ of the two distributions then gives $2g_{\text{eff}}$. The approach is visualized in Fig. 6.9 using a simulated field-frequency map of S_{11}. The method is slightly more accurate and robust because it takes into account a complete frequency trace as opposed to only two points in the simple estimate of the peak splitting. Just like for simply reading of the splitting of the peaks, it requires identifying the degeneracy field. The analysis is complicated by the fact that a parasitic (capacitive) coupling of the feed line and the cavity can shift the phase of the signal. Standing waves in the feed line give rise to a background signal in the reflection parameter. If needed, the phase shift can be introduced phenomenologically or the complex-valued spectrum can be corrected by the inverse mapping technique put forward by Petersan and Anlage [155].

Also for an intermediately strong coupling ($g_{\text{eff}} \approx \kappa_c, \kappa_s$), i.e. when the two peaks are not clearly separated, this method can still be applied as

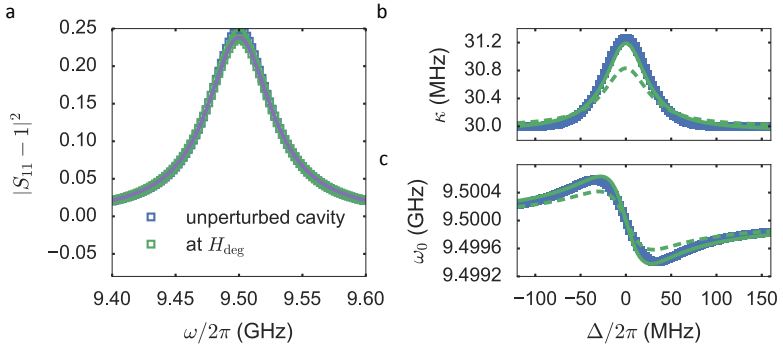

Figure 6.10: Data analysis using the Herskind model at the example of simulated S_{11} with $\kappa_c/2\pi = 30\,\mathrm{MHz}, \kappa_s = 30\,\mathrm{MHz}$ and $g_{\mathrm{eff}}/2\pi = 5\,\mathrm{MHz}$. **(a)** Cut of the simulated S_{11} at and far away from $H_{\mathrm{deg}} = H_{\mathrm{res}}(\omega = \omega_c)$ (symbols). Lorentzian fit (solid line), the linewidth κ increases slightly towards H_{deg}. **(b)** κ as a function of the frequency detuning $\Delta = \omega_s - \omega_c$. **(c)** Resonance frequency ω_0 as a function of Δ. The solid lines in panels (b) and (c) are a simultaneous fit to the Herskind model (Eqs. (6.6) and (6.7)). The dashed lines are the expected result according to the Herskind model, given the parameters for κ_c, κ_s and g from the simulation.

shown in Fig. 6.9 (b) for $g_{\mathrm{eff}} = \kappa_c = \kappa_s = 2\pi \cdot 25\,\mathrm{MHz}$. The scatter of the experimental data, of course introduces a large uncertainty for this method. Note furthermore that only in the strong coupling regime, the lineshape is accurately modeled by Lorentzian distributions. For weaker couplings it is modified and the fit of two Lorentzian distributions in the example of Fig. 6.9 results in $g_{\mathrm{eff}} = 23.7\,\mathrm{MHz}$ instead of the expected $g_{\mathrm{eff}} = 25\,\mathrm{MHz}$. For a more accurate analysis, the slice of S_{11} needs to be modeled with Eq. (6.3) which, however, requires knowledge of the dispersion and the linewidth of the magnetic system.

Herskind model (weak coupling)

As obvious from the above example for an intermediately strong coupled system, the above analysis method is not adequate for the weak coupling regime. The system can instead be modeled as proposed by Herskind et al. [146]. In this model, a single Lorentzian is fitted to $|S_{11}(\omega, H_0 = \mathrm{const}) - 1|^2$ for each H_0. We choose a narrow range for the fits as indicated in Fig. 6.10 (a). From these fits, we extract the resonance

frequency ω_0 and the (HWHM) line width κ of the absorption signal (Fig. 6.10 (b,c)). Both κ and ω_0 can be modeled as proposed by Herskind et al. [146] by

$$\kappa = \kappa_c + g_{\text{eff}}^2 \kappa_s / \left(\kappa_s^2 + \Delta^2\right) \tag{6.6}$$

and

$$\omega_0 = \omega_c - g_{\text{eff}}^2 \Delta / \left(\kappa_s^2 + \Delta^2\right). \tag{6.7}$$

where Δ is the frequency detuning as defined before. From fits to these models, $\omega_c, g_{\text{eff}}, \kappa_s$ and κ_c can be extracted readily. Note that this model can only be successful for weak coupling, i.e. $g_{\text{eff}} \lesssim \kappa_c, \kappa_s$. For more strongly coupled systems, the evolution of κ and ω_{res} is not accurately described by Eqs. (6.6) and (6.7). If this effect is neglected, the extracted coupling rate and relaxation rates are distorted. In the example of Fig. 6.10 (which is well in the weak coupling regime), a coupling rate of $g^{\text{Herskind}} = 5.9\,\text{MHz}$ is extracted using the Herskind model, while a coupling rate of $g^{\text{sim}} = 5\,\text{MHz}$ is expected from the simulation parameters. To establish and visualize bounds of the coupling and relaxation rates for which the Herskind approach returns accurate parameters, we simulate S_{11} for different coupling strengths with Eq. (6.3) and analyze the simulated data sets using the approximate Herskind model as described above. [4] The results are shown in Fig. 6.11. The expected behavior is that for strong coupling, the coupling rate g_{eff} is underestimated, while the relaxation rate of the spin system κ_s is overestimated. In the weak coupling regime, on the other hand, the extracted parameters from the Herskind model are expected to represent the true rates of the system. Note that we cannot reproduce this behavior with the numerical simulations and therefore conclude that the Herskind model, as it is commonly employed to evaluate coupling strengths of hybrid systems (e.g. Refs. [135, 138, 141, 146, 153]), introduces a fairly large error. This fact gets clear by taking a closer look at $|S_{11}(\omega)|^2$:

$$|S_{11}(\omega) - 1|^2 = \frac{\left(\kappa_c^{\text{ext}}\right)^2}{\left(\omega - \omega_c - \frac{g^2(\omega_s - \omega)}{\kappa_s^2 + (\omega_s - \omega)^2}\right)^2 + \left(\kappa_c + \frac{g^2 \kappa_s}{\kappa_s^2 + (\omega_s - \omega)^2}\right)^2} \tag{6.8}$$

The Herskind model assumes a Lorentzian lineshape of $|S_{11}(\omega)|^2$ with the linewidth κ and resonance frequency ω_0 given by Eqs. (6.6) and

[4] The python package `pybbfmr` (Sec. A.1) contains models that simultaneously fit κ and ω. When the signal to noise ratio is high enough, fitting either one of these parameters is sufficient. In the following, we will only analyze the evolution of ω.

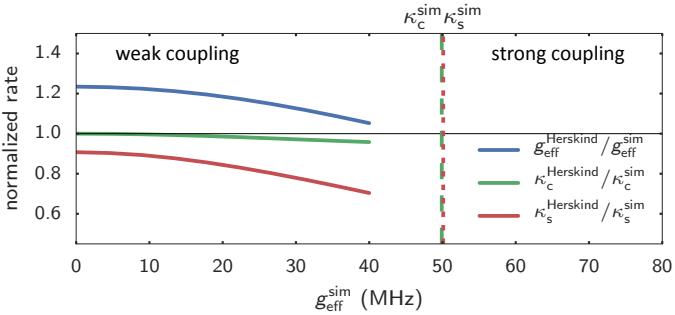

Figure 6.11: Results (solid lines) of the evaluation according to [146] of simulated data for S_{11} with $\kappa_c^{sim} = \kappa_s^{sim} = 2\pi \cdot 50\,\mathrm{MHz}$ (dashed lines). The coupling rate g_{eff}^{sim} of the simulation is varied and the extracted parameters $g_{eff}^{Herskind}$, $\kappa_c^{Herskind}$ and $\kappa_s^{Herskind}$ from the Herskind model are shown (normalized to the respective simulation value). Note that ideally for $g_{eff}^{sim} \to 0$, all rates should converge to 1 in this plot.

(6.7). The form of Eq. (6.8) resembles a Lorentzian distribution Eq. (6.5) and it is highly suggestive to identify a "linewidth" $\kappa' = \kappa_c + g^2\kappa_s / \left(\kappa_s^2 + (\omega_s - \omega)^2\right)$ and a "resonance frequency" $\omega_0' = \omega_c - \left(g^2(\omega_s - \omega)/\kappa_s^2 + (\omega_s - \omega)^2\right)$. However, in Eq. (6.8) $(\omega_s - \omega)$ appears instead of $\Delta = \omega_s - \omega_c$ as in the Herskind model. Note that the former term depends on ω (highlighted in orange) and hence, the lineshape is not a simple Lorentzian but much more complex and depends also on the form of ω_s.[5] Therefore, a Lorentzian fit of $|S_{11}(\omega) - 1|^2$ at constant magnetic field is not appropriate and returns a different linewidth and resonance position as required for Eqs. (6.6) and (6.7). This issue can not be solved easily, as any more elaborate approximation requires prior knowledge of the FMR dispersion, g and κ_s. Alternatively, an iterative approach can be used which is, however, not superior to the method presented in the following section. A radically different approach is to perform experiments in the time domain. Here, the relaxation rate of the (hybrid) system can be extracted for any given H_0 and ω from the ring-down after a step excitation, giving the true relaxation rate at this H_0 and ω, which can then be modeled with Eqs. (6.6) and (6.7). These issues were not known at the time of the experiment and

[5] In other words, the Herskind model is correct when the cavity and FMR dispersion cross perpendicularly, i.e. when $\gamma \to \infty$.

the experimental protocol for a time domain measurement and a correct replacement model for the Herskind approach is still a major challenge. In lack of an adequate approximative model, the Herskind model can nevertheless be used to get an estimate of the coupling rate and allows to compare the results to reports in the literature [135, 138, 141, 153]. With this in mind, we employ the Herskind model in Chap. 7, in which the spectrum is too complex to use the mathematically exact approach described in the following.

Full S21 fit (all coupling regimes)

In the intermediately strong coupled regime, the approximations of the previous models do not hold. We therefore implement a full 2D fit of the complex-valued S_{11} parameter which allows to extract all relevant parameters for all ratios of $g_{\mathrm{eff}}, \kappa_{\mathrm{c}}$ and κ_{s}. Such a fit is challenging as the implementation needs to be efficient enough to enable the fit to converge in a reasonable time and, for the same reason, the initial parameter guess needs to be fairly accurate. Apart from these technical issues, the field independent background signal interferes with the fit and either needs to be included in the model or to be removed efficiently. We choose a simple but powerful method in which we calculate the field derivative of S_{11}: $\partial_B S_{11} = \frac{\partial S_{11}}{\partial(\mu_0 H_0)}$. This selects only the part of the signal that varies with H_0 and hence eliminates the field independent background caused e.g. by standing waves in the feed line. In contrast to Sec. 2.2.4, we do not divide the by the central value of S_{11} as this value can be close to zero at the cavity frequency and hence the result diverges. Naturally, the signature of strong coupling in $\partial_B S_{11}$ is quite different as the absorption signal of the unperturbed (field independent) cavity mode vanishes. The simulated field-derivative spectrum $\partial_B S_{11}$ of the simulation of the strongly coupled system (Fig. 6.8 (a)) is shown in Fig. 6.12. We then fit $\partial_B S_{11}$ to ∂_B (Eqn. 6.3), i.e. we simply apply the same operation to Eq. (6.3) in the residual function of the fit. Note that not only the absolute value is used for the analysis but the full complex-valued S_{11} parameter. In the visualizations, we plot $|S_{11}|$ which already allows to judge the quality of the fit. We perform this method of analysis in the following section in order to evaluate the coupling rate in the strong and the weak coupling using only a single sample.

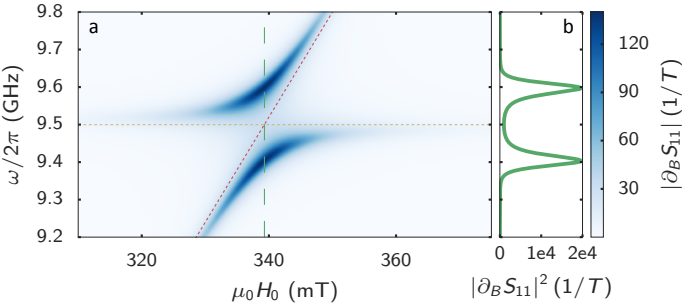

Figure 6.12: Field-frequency map of $\partial_B S_{11}$ for $g_{\text{eff}} = 2\pi \cdot 100\,\text{MHz} > \kappa_c, \kappa_s = /2\pi \cdot 25\,\text{MHz}$ (cf. Fig. 6.8 (a)). The dotted lines are the unperturbed spin (red) and cavity (orange) dispersions.

6.3 From weak to strong coupling in a GdIG – 3D-cavity system

The study presented in this chapter has been conducted in close collaboration with Michael Harder from the University of Manitoba, Canada and is published as Ref. [MF3]. Parts of the text and figures are adapted from this reference.

For the dipolar interaction of the cavity and the magnetic system, the single spin-single photon coupling strength g_0 is proportional to the vacuum microwave magnetic field h^0_{MW} and the dipole moment of the spin [150]. In the scope of the quantum mechanical Tavis-Cummings model, it can be shown that the collective coupling strength g_{eff} of an ensemble of many non-interacting spins to the vacuum microwave magnetic field of a cavity is proportional to the square root of the number N of polarized spins. The classical theories simply take the effective coupling rate of an spin ensemble to be proportional to the square root of the net magnetic moment $m = MV$ of the sample.[6] In this section, we aim to experimentally investigate whether this relation holds for exchange-coupled magnetic systems. In contrast to paramagnets, the magnetization M of ferromagnets typically shows only a weak temperature dependence for temperatures well below the Curie temperature. This weak temperature dependence is advantageous for appli-

[6] While in the 1D model of Ref. 145 the magnetic moment is proportional to the thickness of the sample, in the 3D case considered here, it scales with the total volume V of the sample.

cations as it makes the system more robust against external perturbations. In order to reach and study different coupling regimes, however, the sample size typically needs to be changed [38], which also involves readjusting the cavity-feed line coupling. Furthermore, changing the sample is prone to introduce experimental uncertainties as any slight inaccurate placement of the sample changes the loading and hence the coupling strength of cavity and sample.

Here, we take a simple, robust and continuously tunable approach that allows for an in-situ manipulation of g_{eff} by simply adjusting an external control parameter: We vary the net magnetic moment of the compensating ferrimagnet GdIG by changing the temperature. As introduced in Chap. 1, compensating ferrimagnets are a particular class of ferrimagnets containing two or more magnetic sublattices that feature a compensation point, at which the net remanent magnetization vanishes. In the case of GdIG, this magnetic compensation occurs at the compensation temperature $T_{\mathrm{comp}} \approx 270\,\mathrm{K}$. By investigating the temperature region between 5 and 190 K, we experimentally achieve a variation of the macroscopic net magnetization of over one magnitude and expect to observe the according change in g_{eff}.

6.3.1 Sample details

The investigated sample is a $t = 2.6\,\mu\mathrm{m}$ thick Gadolinium iron garnet film grown by liquid phase epitaxy on gadolinium gallium garnet (GGG) provided by Zhiyong Qiu/Eiji Saitoh from the Institute for Materials Research, Tohoku University, Sendai, Japan. The sample with lateral dimensions $l = 5\,\mathrm{mm}$ and $b = 2\,\mathrm{mm}$ is a slice of the same sample investigated in Chap. 4. The net magnetization M^{SQUID} of the GdIG thin films was measured using SQUID magnetometry at an external magnetic field of 0.1 T by Geprägs et al. [122] (see Fig. 6.13).

6.3.2 Results and discussion

For the magnon-photon coupling experiments, we employ the setup described in Chap. 6 and place the sample in the magnetic field anti-node (electric field node) of the TE_{011} mode of a 3D microwave cavity.

We measure the complex (phase sensitive) reflection scattering parameter S_{11} around the resonance frequency of the cavity mode while applying a variable external magnetic field H_0 in the film plane. The applied probe power is chosen to be small (0 dBm source power of the VNA) so that non-

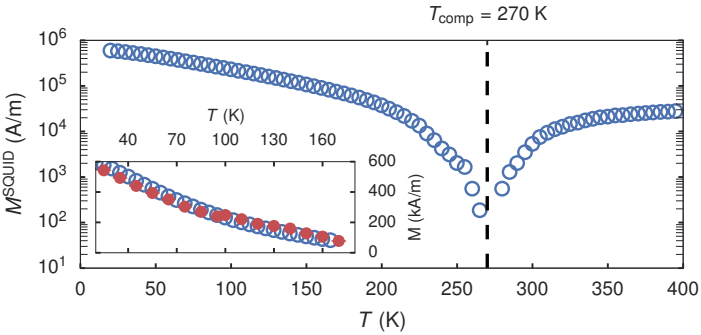

Figure 6.13: Net magnetization M_s measured at $\mu_0 H_0 = 0.1\,\mathrm{T}$ (applied in the film plane) using SQUID magnetometry (blue circles). Data taken from [122] and normalized to the here measured effective magnetization at 15 K. Inset: Within the investigated temperature range, the evolution of the effective magnetization M_{eff} extracted from the FMR measurements (red data points) agrees very well with the net magnetization M_s as determined by SQUID magnetometry. This figure is adapted from Ref. [MF3].

linear processes do not play a role. At this power, the number of photons excited in the cavity is approximately $N_{\mathrm{Ph}} = P/(\hbar\omega_c\kappa_c) = 2\times10^{13}$ and is several orders of magnitude lower than the minimum effective number of spins in the sample (1×10^{17}).

Because we aim to observe the transition of the system from the weak coupling regime ($\kappa_c, \kappa_s > g_{\mathrm{eff}}$) to the strong coupling regime ($\kappa_c, \kappa_s \leq g_{\mathrm{eff}}$), the approximate methods using Lorentzian fits or the Herskind model (Sec. 6.2.1) are not sufficient. The system has to be modeled by the complete reflection characteristic given by Eq. (6.3) for a quantitative evaluation instead. We fit $\partial_B S_{11}$ for each temperature as described above and extract M_{eff}, g_{eff}, κ_c and κ_s. The g-factor is fixed to $g = 2$ over the whole temperature range based on Ref. 30, thereby reducing the number of free parameters further.[7] Typical data for the absolute value of $\partial_B S_{11}$ is shown in Fig. 6.14 for two distinct temperatures. In Fig. 6.14 (110 K) the char-

[7] In Chap. 4, we determined the temperature-dependent value of g via broadband FMR as a function of temperature in a sample from the same batch and find that g is close to 2 over the observed temperature range and increases only slightly towards lower temperatures. The 2D fit is robust against a small changes in g and it has been verified that the results reported in this chapter do not change when taking the deviations from $g = 2$ into account explicitly.

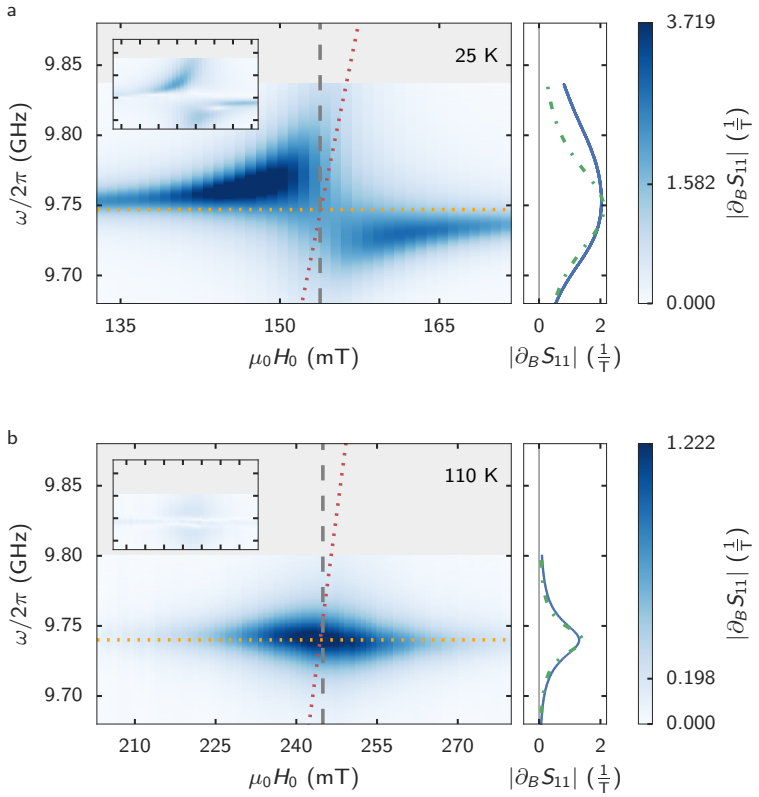

Figure 6.14: Magnitude of the magnetic field derivative of the reflection parameter S_{11} for **(a)** 25 K and **(b)** 110 K. The coupling visibly decreases from 25 K to 110 K. The resonance frequency of the unperturbed cavity $\omega_c/2\pi$ (orange) and the unperturbed spin system $\omega_s/2\pi$ (red) are marked with dotted lines. Inset: Residuals of the fit to Eq. (6.3) on the same scale. Line cuts: Data (blue) and fit (green line) at the field where the unperturbed cavity mode and magnon mode are degenerate (dashed vertical gray line in the adjacent colorplot). This figure is adapted from Ref. [MF3].

acteristic weak coupling response is observed (cf. Fig. 6.8 (d_i)). Note that by taking the field derivative of S_{11}, the unperturbed cavity absorption peak vanishes (Fig. 6.14) as ω_c is field independent. Towards low temperatures (Fig. 6.14 (25 K)), the coupling visibly increases. The resulting fit is virtually indistinguishable from the data in Fig. 6.14. We therefore display the residual of the fit to the data in the insets on the same scale as the data in order to make deviations of the fit visible more clearly and to demonstrate the good agreement of fit and data. A vertical cut (dashed gray lines) of the 2D data and the fit is shown for the static magnetic field corresponding to $\omega_s = \omega_c$ as an example. The 2D-fit is very good for high temperatures (Fig. 6.14 (110 K)), but the residuum shows some deviation of fit and data for low temperatures (Fig. 6.14 (25 K)). We attribute this slight discrepancy to the presence of a second resonance line in our GdIG sample, which is apparent at low temperatures upon close examination. The second resonance might originate from spatial inhomogeneities in the sample. The data, the analysis scripts and results are publicly accessible under Ref. [114] for further analysis and evaluation.

We first discuss the effective magnetization M_{eff} extracted from the fitting procedure and displayed in the inset of Fig. 6.13 (red data points). The temperature evolution of the effective magnetization M_{eff} determined using FMR and the net magnetization M_s measured by SQUID magnetometry agree well, indicating that the dominant anisotropy contribution in our GdIG thin film is indeed given by shape anisotropy in the here observed temperature range. This result is in agreement with the results of Chap. 4 where we find that the cubic anisotropy field increases drastically close to T_{comp} but is small compared to the net magnetization at the temperatures below 160 K which are investigated here. We therefore take $M_s = M_{\text{eff}}$ in the following. The observed slight difference of M_s and M_{eff} can be explained by a small increase of the g-factor with decreasing temperature as indicated in Ref [156] and in the broadband measurements in Chap. 4.

As central result, we confirm the scaling of the effective coupling rate g_{eff} with the magnetic moment (or magnetization). As mentioned above, we expect $g_{\text{eff}} \propto \sqrt{M_{\text{eff}}}$ in analogy to the paramagnetic case. Figure 6.15 shows g_{eff}^2 as a function of M_{eff}, where a straight line indicates the expected scaling with $g_{\text{eff}} = 0$ at $M_{\text{eff}} = 0$. The data follows this behavior accurately over an order of magnitude of the magnetization. As noted above, for low temperatures (large magnetization) a second resonance is indicated that we do not fit separately. The fit therefore slightly overestimates the coupling in this regime which can also be seen in Fig. 6.15. From the

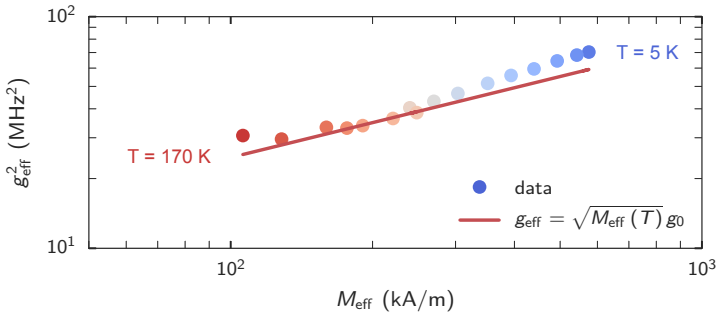

Figure 6.15: Effective coupling rate g_{eff}^2 as a function of the effective magnetization. The data agrees very well with the expected scaling behavior $g_{\mathrm{eff}} \propto \sqrt{M_{\mathrm{eff}}}$ (red line). This figure is adapted from Ref. [MF3].

slope, we can calculate the single spin – single photon coupling rate to $g_s/2\pi = g_0/2\pi \left(\mu_B\sqrt{3}/V\right)^{1/2} = 0.072\,\mathrm{Hz}$ with the sample volume V and assuming a spin 1/2 particle with a g-factor of 2. This value is in reasonable agreement with the values of $g_s/2\pi = 0.043\,\mathrm{Hz}$ determined for paramagnetic ensembles [153].

In order to coherently exchange excitations between a magnonic system such as GdIG and a photonic system, strong coupling (i.e. $\kappa_c, \kappa_s \leq g_{\mathrm{eff}}$) is required. Fig. 6.16 displays the relaxation rate of the cavity κ_c and the magnons κ_s for comparison. The cavity decay rate κ_c depends on the coupling of the feed line to the cavity and therefore varies slightly with temperature as the coupling mechanism has to be readjuste for each temperature (cf. Chap. 6). The mean value of κ_c is shown as green line in Fig. 6.16, while its standard deviation is depicted as green shaded area. The FMR line width, κ_s significantly increases towards T_{comp}, in good agreement with reports in the literature [156]. Finally, g_{eff} is plotted on the same scale and shows the increase towards low temperatures also shown in Fig. 6.15. Comparing the three rates, we find that the system is in the high cooperativity regime ($g_{\mathrm{eff}}^2 > \kappa_c\kappa_s$) for temperatures below 110 K (shaded region II in Fig. 6.15) and enters the strong coupling regime (region III) for liquid helium temperatures. By choosing a slightly larger sample size or specially shaped cavity modes [142], strong coupling and thus the coherent exchange of information between a 3D cavity and GdIG is feasible even at higher temperatures.

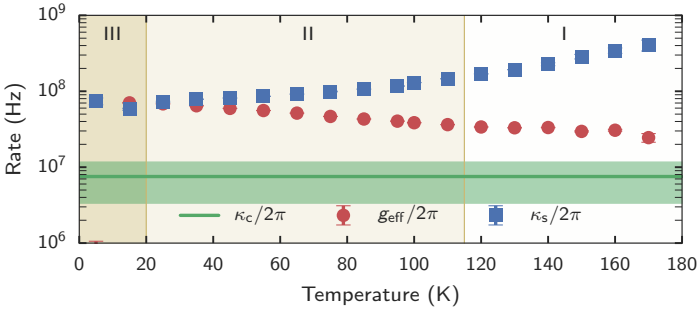

Figure 6.16: Magnon relaxation rate κ_s (blue dots), cavity relaxation rate κ_c (gereen line) and effective coupling rate g_{eff} (red dots) as a function of temperature. The shaded green area denotes the standard error of the cavity relaxation rate. The coupling rate increases to low temperatures while the magnon relaxation rate drops. Thus, the system transitions from weak coupling (shaded region I) to a high cooperativity regime (region II) and enters strong coupling at low temperatures (region III), where g_{eff} exceeds κ_s and κ_c. This figure is adapted from Ref. [MF3].

6.4 Conclusion

In this chapter, we introduced the general concept of the coupling of two resonant systems. We discussed the coupling of a magnetic system to a microwave cavity resonator and its phenomenology in detail. For this, we described and critically compared different methods for analyzing the signature of the magnon-photon coupling in the measured microwave reflection parameter S_{11}. In this scope, we discussed the error introduced by the approximative models for the weak and for the strong coupling case. We linked these approximative models via a comprehensive analysis method, in which the full field-frequency map of S_{11} is fitted. In the last part of the chapter, we investigated the magnon-photon coupling in a system consisting of the compensating ferrimagnet (GdIG) and a microwave cavity by using the later method. In the experiment, we control the magnetization of GdIG with temperature and extract the scaling of the coupling rate with the net magnetization of the sample. We thereby confirm the expected scaling behavior $g_{eff} = g_0\sqrt{M_s}$ of the ferrimagnet–cavity system. This result proves that the description used for paramagnets is equally appropriate for exchange-coupled spin systems. In order to realize the transition from the

strong to the weak coupling regime without modifying the sample or setup, we use a sample size that is just sufficient to reach the strong coupling regime. We emphasize, however, that strong coupling is easily accessible with a GdIG – 3D microwave cavity system.

CHAPTER 7

SPIN PUMPING IN THE STRONG COUPLING REGIME

A key advantage of magnetically ordered systems over their paramagnetic counterparts – which has yet to be fully explored – is the ability to probe magnetic excitations electrically through spin pumping and the inverse spin Hall effect. Spin pumping, in general, relies on ferromagnet/normal metal (FM/NM) heterostructures and has been demonstrated for a wide variety of material combinations [18]. Under resonant absorption of microwaves, the precessing magnetization in the ferromagnet sources a spin current into the normal metal where it is converted into a charge current via the inverse spin Hall effect. This spin Hall charge current is then detected. In ferromagnetic insulator (FMI)-based FMI/NM heterostructures, charge current signals from the rectification of the microwave electric field are very small [157], leading to a dominant spin pumping/spin Hall signal. This makes it particularly easy to investigate spin Hall-related phenomena in FMI/NM heterostructures.

In this chapter, we use a FMI/NM bilayer consisting of YIG and platinum layers, which have been employed extensively in the literature to investigate spin pumping [18, 39, 149]. The spin pumping effect in general is well understood for weak photon-magnon coupling [18, 66], i.e. for situations where the decay rates of the cavity and the magnetic system are larger than the photon-magnon coupling strength. However, the large spin density of YIG and the resulting large effective coupling strength allows one to

reach the strong coupling regime easily in typical spin pumping experiments. The experimental observation [39] and theoretical treatment [145, 154] of spin pumping in a strongly coupled magnon-photon system has only recently been performed. These results suggest that combining spin pumping and strong magnon-photon coupling may enable the control and electrical read-out of quantum states in ferromagnets using a hybrid architecture. Experiments directly linking spin pumping in the weak and strong coupling regime are, however, still missing. Such experiments are one important step towards understanding the functional principle and key requirements for such a hybrid architecture.

In this chapter, we present a systematic study of the interplay of magnons and photons in a magnetic resonance experiment in a YIG|Pt bilayer mounted in 3D microwave cavity. The experiments have been performed in close collaboration with Michael Harder from the University of Manitoba, Canada. Our study has been published as Ref. [MF2]. Parts of the text and the figures in this section are adapted from this reference.

In the experiments, we measure the microwave reflection spectra and the electrically detected spin pumping signal in the system. The tunable cavity quality factor (Chap. 6) allows us to systematically move in and out of the strong coupling regime. Measurements with high magnetic field and frequency resolution allow us to clearly observe the coupling of spin wave modes with the hybridized mode formed by the cavity and the fundamental ferromagnetic resonance mode, i.e. the Kittel mode. We explore a different approach as recently used by Zhang et al. [36]: In our setup, instead of tuning the cavity frequency we tune its decay rate while the effective magnon-photon coupling rate and the magnon decay rate stay constant. We thus achieve a transition from the strong coupling regime where the decay rates of spin and cavity system are both considerably smaller than the effective coupling rate, to the weak coupling regime where the cavity decay rate is much higher than the magnon-photon coupling rate.

This chapter is organized as follows: We first review the general theory of spin pumping and highlight the main features of spin pumping in the case of strong magnon-photon coupling. A description of the experimental details follows, which extends Chap. 6 to simultaneously measure the microwave reflection of the system while simultaneously recording the DC spin pumping voltage across the Pt. Finally, we discuss the observation of strong coupling between the cavity mode and both the fundamental magnetic resonance and standing spin wave modes. We also demonstrate the transition from strong to weak (MIT) coupling by tuning the cavity

line width and discuss the difference in the experimental spin pumping signature in both the strong and weak regimes.

7.1 Theory of spin pumping and strong coupling

Spin pumping in insulating ferromagnet/normal metal bilayers in the weak coupling regime is well understood [18, 66, 149]: An additional mechanism which dampens the magnetization precession becomes available by spin pumping, as the precessing magnetization is driving a spin current into the adjacent normal metal [66]. This process, depicted in Fig. 7.1 (a), can be observed as an increase in the Gilbert damping parameter or indirectly by detecting the spin current electrically. In electrically detected spin pumping, this spin current is converted in the normal metal layer into a charge current via the inverse spin Hall effect (ISHE) [158]. For electrical open circuit conditions, one thus obtains a voltage which scales as [18, 149]

$$V_{\mathrm{SP}} = e g^{\uparrow\downarrow} \eta \lambda_{\mathrm{SD}} \tanh \frac{t_{\mathrm{N}}}{2\lambda_{\mathrm{SD}}} \sin^2(\theta) \zeta \frac{\omega}{2\pi} R w P \theta_{\mathrm{SH}}, \tag{7.1}$$

with the elementary charge e, the width w and the resistance R of the Pt layer.

It contains information on the spin mixing conductance $g^{\uparrow\downarrow}$, the spin diffusion length λ_{SD} in the normal metal, the magnetization precession cone angle θ, the metal's spin Hall angle θ_{SH}, and depends on the thickness of the normal metal layer. The spin backflow correction factor η describes that the created spin accumulation in the normal metal can drive a spin current back into the ferromagnet thereby reducing the effective spin current that contributes to the spin pumping voltage [159]. In the following, we will use a YIG|Pt bilayer with a Pt layer thickness $t_{\mathrm{N}} \gg \lambda_{\mathrm{SD}} \approx 1.5\,\mathrm{nm}$ [18]. In this case, the spin accumulation in the normal metal decays on the length scale of λ_{SD} away from the interface. Hence, the spin current is driven along the gradient of the spin accumulation further into the normal metal. The spin backflow is therefore small and $\eta \approx 1$ for $t_{\mathrm{N}} \gg \lambda_{\mathrm{SD}}$. The ellipticity correction factor ζ accounts for an anisotropy induced elliptic precession of the magnetization as touched upon in Sec. 1.2. In the high field limit of FMR, i.e. for $H_0 \gg H_{\mathrm{ani}}$, the ellipticity reduces and ζ becomes 1. The maximal precession cone angle θ and thus the maximal expected spin pumping voltage depends on the microwave power but, as Lotze [154]

derived, also on the coupling strength between cavity and spin system. For strong coupling, the cone angle is reduced as compared to the weak coupling case due to the hybridized nature of the excitation. The detected spin Hall voltage at the field of degeneracy and the resonance frequency of the hybrid system in the high cooperativity case ($g_{\mathrm{eff}} > \kappa_{\mathrm{s}}\kappa_{\mathrm{c}}$) is given by [154]:

$$V_{\mathrm{SP}} \propto \frac{1}{2g_{\mathrm{eff}}^2\kappa_{\mathrm{s}}\kappa_{\mathrm{c}}} \tag{7.2}$$

This dependence of V_{SP} on g_{eff} is shown in Fig. 7.1 (b).

The other contributions in the equation for V_{SP} are material constants: The spin mixing conductance $g^{\uparrow\downarrow}$ describes the transparency of the ferromagnet/normal metal interface and limits the spin pumping efficiency generally; the spin diffusion length λ_{SD} in conjunction with the normal metal thickness t_{N} accounts for a spin accumulation in the normal metal and reduces the spin pumping efficiency if $t_{\mathrm{N}} \lessapprox \lambda_{\mathrm{SD}}$. Furthermore, short circuiting of the generated spin pumping voltage via the normal metal layer reduces the detected voltage. For the YIG|Pt heterostructures this plays a role for Pt thicknesses considerably larger than the spin diffusion length $t_{\mathrm{N}} \gg \lambda_{\mathrm{SD}} \approx 1.5\,\mathrm{nm}$ [18].

7.2 Experimental details

Sample preparation

In our experiments, we use YIG|Pt heterostructures. The YIG layer was grown by liquid phase epitaxy (LPE) on (111)-oriented Gadolinium Gallium Garnet (GGG) substrates to a thickness of 2.8 µm and was purchased from Innovent Jena e.V. The Pt layer was deposited at the WMI using electron beam evaporation in collaboration with the help of Michaela Lammel and Stephan Geprägs. This low energy deposition technique avoids interdiffusion of Pt and YIG and hence gives an interface with well separated layers. Earlier studies on in-house bilayers with the same Pt deposition method show that the Pt layer exhibits no proximity magnetization [160]. Hence, rectification of an induced high frequency current in the platinum, for example via the AMR effect, which would mask the spin pumping signal, is not possible. In order to produce a high quality interface between YIG and Pt and thus a large spin mixing conductance $g^{\uparrow\downarrow}$, we follow the work of Jungfleisch et al. [161]: After cleaning the sample with acetone

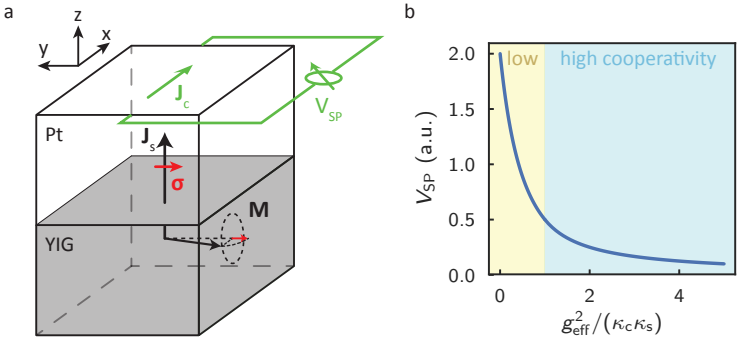

Figure 7.1: Process of spin pumping. **(a)** Angular momentum is transfered as spin current from the ferromagnet to the adjacent normal metal layer. Only the static (DC) component of the pumped spin current $\mathbf{J}_\mathrm{s}$ which is polarized (σ) along the equilibrium magnetization direction is depicted. In the normal metal, the spin current is converted into a charge current $\mathbf{J}_\mathrm{c} = \mathbf{J}_\mathrm{s} \times \sigma$ via the spin Hall effect, which, in the open-circuit configuration, is detected as a voltage V_SP. **(b)** Due to the coupling of the magnetic system to the spin system, the cone angle of the magnetic precession is reduced for higher coupling resulting in a lower net spin current flow and hence a lower maximal DC voltage. Panel (b) is based on calculations from Ref. [154].

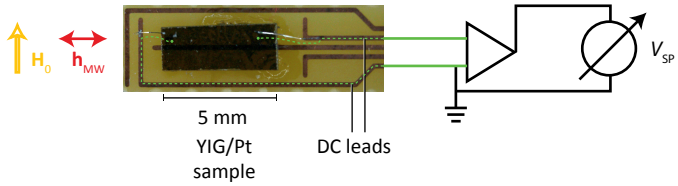

Figure 7.2: The mounted YIG|Pt bilayer bonded to the DC leads of the sample holder (highlighted in green). The direction of the static magnetic field $\mathbf{H_0}$ and the microwave magnetic field $\mathbf{h}_\mathrm{MW}$ is indicated with the arrows. The electrical detection circuit is depicted schematically, for a description of the complete setup, see Chap. 6.

and isopropyl alcohol, we treat the YIG surface by piranha etching for 5 minutes in ambient conditions. Thereafter, the sample is annealed at 500 °C for 40 minutes in an oxygen atmosphere of 25 µbar. Under high vacuum, it is transferred into an electron beam evaporation chamber where nominally 5 nm Pt are deposited. The exact Pt thickness is determined after deposition using X-ray reflectometry. Note, however, that for our analysis the Pt layer thickness is of minor importance as it was larger than the spin diffusion length $\lambda_{SD} \approx 1.2\,\text{nm}$ of Pt such that the Pt layer simply serves as a perfect spin sink [162].

In order to achieve collective strong coupling between magnons and cavity photons, the number of magnetic moments must be sufficiently high. Therefore, we diced the sample into several pieces of different lateral dimensions. Magnetic resonance experiments in the strong coupling regime showed that the $\sqrt{N}$ scaling of the coupling strength discussed in Section 7.1 is indeed obeyed upon comparing samples with different volume and thus different total magnetic moment. In the following, we focus on a sample with lateral dimensions 2 mm × 3 mm, which, with the effective spin density $\rho_S = 2.1 \times 10^{22}\,\frac{\mu_B}{\text{cm}^3}$ of iron atoms in YIG [104], contains on the order of 4×10^{17} spins. The sample is mounted on the FR4 printed circuit board sample holder described in Chap. 6 and is wire bonded as depicted in Fig. 7.2 (b).

Experimental setup

The setup consists of the YIG|Pt sample, positioned in the electrical field node of a Bruker Flexline MD5 dielectric ring cavity, a water-cooled electromagnet and the Agilent PNA-X VNA. It allows to record the S_{11} parameter as a function of H_0 and ω and is described in detail in Chap. 6. The measurement protocol for these field-frequency maps of S_{11} is essentially identical to the procedure in Sec. 6.3. Here, we use the ability to tune the external relaxation rate κ_c^{ext} of the cavity by manually adjusting the mechanical coupling of cavity and feed line. This allows us to achieve unloaded quality factors of Q_c from 0 to 8000.

The driving power of the VNA of 15 dBm that we use in this chapter excites at maximum on the order of $N_{Ph} = P/(\hbar\omega\kappa_c) = 3 \times 10^{14}$ photons in the cavity. This number is considerably smaller than the number of spins in the sample (4×10^{17}). The theory presented in Sec. 6.2 is therefore well justified [163]. Here, we use a fairly high excitation power to achieve a large spin Hall voltage. By performing a power-sweep (not shown), we ensure

that no non-linear effects such as line-broadening, resonance frequency shift or a subsidiary resonance distort the measurements. The VNA's intermediate frequency (IF) bandwidth was chosen to be 100 Hz which leads to a frequency sweep time of approximately 2 s for each magnetic field step. A microwave calibration of the cables up to the resonator's SMA connector was performed. However, the calibration did not include the feed line inside the resonator mount, which is not easily accessible. Therefore, S_{11} still contains a frequency-dependent background signal which needs to be removed for the quantitative analysis of the relaxation rates and the coupling rate. Performing a full 2D fit of the field-frequency map of S_{11} as in Sec. 6.3 is not possible due to the many PSSWs that are observed in the YIG sample. We therefore choose to utilize the full complex S parameter for the background subtraction by using the inverse mapping technique outlined by Petersan and Anlage [155] and a subsequent Lorentzian fit to the magnitude of the data to gain a reliable measurement of the linewidth (Sec. 6.2.1). The method allows to selectively analyze the contribution of the each mode with the Herskind model.

Note that even though standing waves in the microwave feed line will not appear in the calibrated reflection measurement they will still change the total power in the cavity and therefore may complicate the electrically detected DC spin pumping signal. Uncalibrated measurements did not show sharp feed line resonances in the frequency range studied here but only smooth oscillations with an amplitude change of less than 1 dB and there was no correlation with the DC signal amplitude resolved. In order to fit the data and as it improves clarity, we only discuss calibrated measurements in the following.

The DC voltage from the sample was measured along the cavity axis and thus perpendicular to the external magnetic field and the sample normal. As outlined in Chap. 6, it was amplified with a low noise differential voltage amplifier model 560 from Stanford Research Systems. The amplifier was operated in its low noise (4 nV/$\sqrt{\text{Hz}}$) mode and set to a gain of 2×10^4. The analog high-pass filter of the amplifier was disabled; However, a low-pass filter with a 6dB roll-off at 1 kHz was employed. The amplified voltage signal was finally recorded using the auxiliary input of the VNA simultaneously with the cavity reflection S_{11}.

All following experiments have been performed at room temperature.

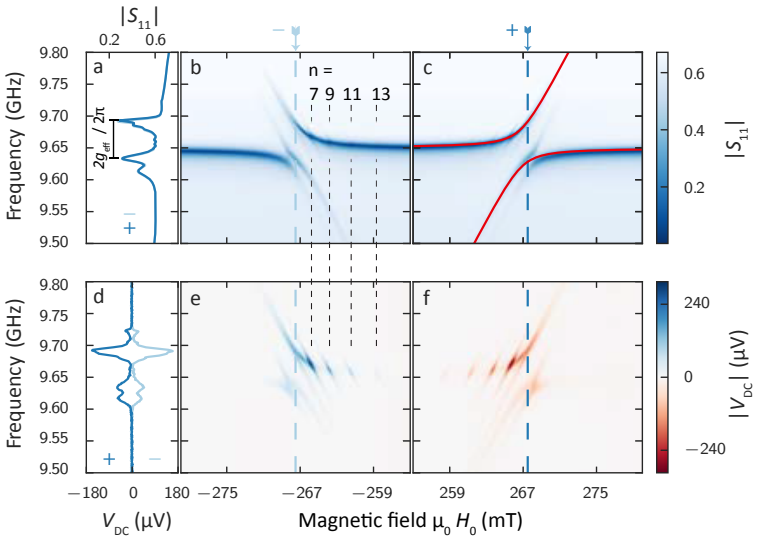

Figure 7.3: (b, c) Reflection parameter S_{11} recorded while sweeping the magnetic field and the microwave frequency. Strong coupling of the collective spin excitations is indicated by a clear anti-crossing that is modeled with Eq. (6.2) (red line). Perpendicular standing spin wave modes to the low field side of the main resonance are visible. **(e, f)** Simultaneously recorded DC voltage. Fundamental and spin wave modes are visible where the latter couple less strongly and thus pump spin current more efficiently. **(a, d)** Line cuts at $H_0 = \pm 267.5\,\mathrm{mT}$ show the symmetry under field reversal for S_{11} (a) and V_{DC} (d). This figure is adapted from Ref. [MF2].

7.3 Results and discussion

We first focus on the case of the critical coupling of the feed line to the cavity in which most FMR experiments are conducted. As introduced in Chap. 6, in this case, the internal loss rate of the cavity equals the loss rate to the feed line and the quality factor is $Q_{\mathrm{c}} = Q_{\mathrm{c}}^{\mathrm{int}}/2$. Note that inserting a sample and holder into the cavity will reduce the cavity Q_{c} further by an amount which depends on the sample and holder details such as conductivity and dielectric losses. Based on our measured loaded $Q_{\mathrm{c}} = 706$, the cavity decay rate is calculated to be $\kappa_{\mathrm{c}}/2\pi = \frac{\omega_{\mathrm{c}}}{2\pi}/(2Q_{\mathrm{c}}) = 6.8\,\mathrm{MHz}$.

The strong coupling of the magnon and cavity system is immediately clear from the strong anti-crossing of the field independent cavity resonance

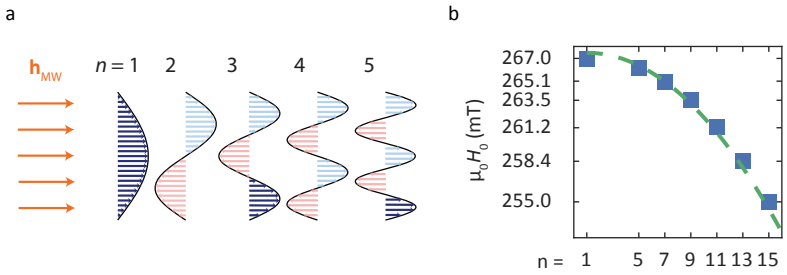

Figure 7.4: (a) A homogeneous excitation microwave field $\mathbf{h}_{\mathrm{MW}}$ couples only to the part of the dynamic magnetization of a PSSW that has no corresponding π-phase shifted component (dark blue). For the shown pinned boundary conditions only odd modes can be excited, where the effective magnetization (blue) scales as $1/n$. **(b)** PSSW resonance fields extracted from the weakly coupled case (symbols, cf. Fig. 7.6) and resonance fields anticipated with values from literature [46, 164, 165] (dashed line).

frequency ω_{c} and the magnon dispersion ω_{s} (Fig. 7.3). In the investigated microwave frequency band around $\omega_{\mathrm{c}} = 9.65\,\mathrm{GHz}$, the resonance frequency is approximately linear in magnetic field, given by Eq. (1.14) with $g = 2.0$ and $M_{\mathrm{eff}} = 147\,\mathrm{kA\,m^{-1}}$ of YIG. As shown in Sec. 6.2, this anti-crossing corresponds to two distinct peaks in a cut at constant $H_0 = H_{\mathrm{res}}$. In the reflection spectrum in Fig. 7.3 (a), these two peaks are immediately visible. From the splitting of the peaks, we extract the effective coupling rate of $g_{\mathrm{eff}}/2\pi = 31.8\,\mathrm{MHz}$ of the fundamental mode and any degenerate modes to the cavity. Taking into account the number of spins in the sample, the single spin coupling rate is on the order of $g_0/2\pi = 0.1\,\mathrm{Hz}$ which is in agreement with experiments on paramagnetic systems [153] and the results from Sec. 6.3. Using Eq. (6.2), we model the resonance frequencies for this value of g_{eff} and superimpose it with the experimental data in Fig. 7.3 (c). The modeled resonance frequencies (red solid line) agree very well with the experimental resonance frequencies of the system that are distinguished by the minimal absolute value of $|S_{11}|$ for each H_0 (color coded).

In our setup, even the coupling of higher order perpendicular spin wave modes (PSSWs) to the cavity can be resolved. In the 3D case, for the condition where the magnetization is pinned at least at one surface of the film (and in the absence of any anisotropies or magnetic gradients), the magnon spectrum can be calculated easily [166]. The difference of

the resonance field of the n^{th}-mode from the fundamental ($n = 1$) mode $H_{\text{res}}^{(n)} - H_{\text{res}}^{1}$ is proportional to $(n-1)^2$. We number the spin waves as noted in Fig. 7.3 taking into account that with an uniform driving field only odd numbered modes can be excited as illustrated in Fig. 7.4 (a). In the anti-crossing of the fundamental mode, at least one further spin wave mode can be observed and a slight asymmetry indicates that there are further modes that can not be resolved. We therefore start the numbering for the clearly separated spin waves with $n = 7$. The resonance fields of the spin wave modes, shown in Fig. 7.4 (b), agree well with the anticipated $H_{\text{res}}^{(n)} - H_{\text{res}}^{1} \propto n^2$ behavior which confirms our numbering. The resonance fields can be quantitatively modeled with values of the exchange stiffness $D = 5.30 \times 10^{-17}\,\text{T}\,\text{m}^2$, $M_{\text{s}} = 140\,\text{kA}\,\text{m}^{-1}$ and $\gamma/2\pi = 28.0245\,\text{GHz}\,\text{T}^{-1}$ reported in the literature [46, 164, 165].

Cao et al. [145] also calculated the expected coupling strength for different modes and found that the coupling decreases with increasing mode number as $g_{\text{eff}} \propto 1/n$. This can be understood when considering the microwave mode profiles and the fact that the spatial mode profile of the microwave field h_{MW}^{0} in a cavity is typically homogeneous and in phase throughout the thickness of the (thin film) sample. As noted above, this is the reason why only every second mode can be excited and furthermore, it effectively reduces the magnetization to which the microwave can couple to is to M_{s}/n.

The resonance field of the lowest order spin wave mode $n = 5$ is very close to the resonance field of the fundamental resonance and is thus difficult to analyze quantitatively. The $n = 7$ spin wave mode exhibits the largest effective coupling (3 MHz) of all other spin wave modes. It is shown Fig. 7.5 in detail. The red and white lines correspond to the harmonic oscillator model (Eq. (6.2)) for the fundamental mode and $n = 7$ spin wave mode, respectively. As the spin wave couples to an already hybridized system, we superimposed the dispersion $\omega_{\text{c}} = \omega_{\text{res}}(H_0)$ of the hybridized system of fundamental mode and unperturbed cavity as the "cavity" mode in the modeling of the spin wave mode couplings.

In order to quantify the coupling strength of the higher order modes which interact only weakly with the hybridized cavity–fundamental FMR mode ($n = 11, 13, 15$), we follow the approach of Herskind et al. [146] which is described in detail in Sec. 6.2.1. In Fig. 7.6 (a), the characteristic line broadening around the resonance field of each spin wave mode that arises due to the coupling can be clearly distinguished. The background

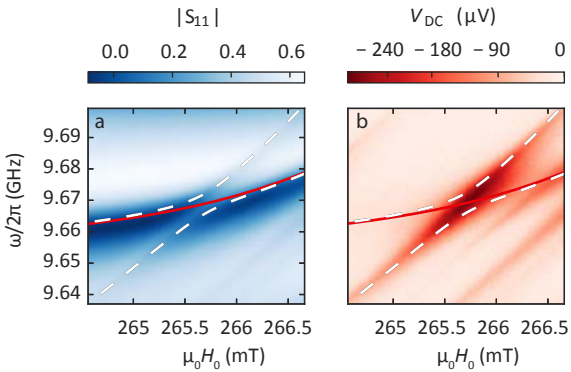

Figure 7.5: Detail of the $n = 7$ spin wave mode in microwave reflection (a) and as voltage-detected spectrum (b). Superimposed is the dispersion relation of the strong coupling between the fundamental FMR mode and the cavity as solid red line. The anti-crossing of this hybrid and the $n = 7$ spin wave mode is displayed as dashed white lines. This figure is adapted from Ref. [MF2].

slope originates from the strong coupling between the fundamental FMR mode and the cavity mode. We remove this background by interpolating linearly over the region-of-interest in which we fit Eq. (6.6) (red solid line).

From the fit, we extract the spin wave–cavity coupling strength $g_{\text{eff}}^{(n)}$ for each weakly coupled spin wave mode. It has to be considered (Sec. 6.2.1) that the Herskind model causes an unknown systematic uncertainty on the extracted coupling rate that is not reflected in the error bars, which represent the statistical standard error only. We expect that this uncertainty does not change significantly for the different modes (cf. Fig. 6.11). The data therefore allows to deduce that the coupling strength of the spin waves to the already hybridized cavity resonance decreases with the order of the mode. This can be understood by taking into account that the effective magnetic moment to which the homogeneous microwave field can couple decreases with increasing mode number as illustrated in Fig. 7.4. For the more strongly coupled spin wave modes ($n = 7$ and 9) we determine the effective coupling strength from the splitting of two fitted Lorentzian absorption peaks. The fit of the $n = 7$ spin wave mode is displayed as an example in Fig. 7.6 (b). The extracted values, shown in Fig. 7.6 (c), match with the also shown theoretically expected $\frac{1}{n}$ dependence of the coupling

strength [145]. Note, however, that due to the uncertainty introduced by the Herskind model and the limited range of $1/n$ values, we need to consider $g_{\mathrm{eff}}^{\infty} = 0$ to obtain a reliable fit. From this fit we can extrapolate an effective coupling of the $n = 1$ mode, the fundamental mode, of $22.7(19)$ MHz. This value, however, deviates from the effective coupling extracted from the main anti-crossing (Fig. 7.3 (a)) by 9.1 MHz. The discrepancy can be lifted by taking into account that the magnon mode $n = 3$ is not resolved. Hence, the previously measured coupling rate of 31.8 MHz is comprised of the $n = 3$ and the $n = 1$ mode. With an extrapolated value of 7.6 MHz for the coupling rate of the $n = 3$ mode, the coupling rate of the fundamental mode exclusively calculates to $g_{\mathrm{eff}}^{1}/2\pi = 24.2$ MHz which is in agreement with the extrapolated value.

The ratio of the effective coupling rate and the spin decay rate κ_{s} (Fig. 7.6 (c)) confirms that the higher order spin waves couple weakly to the cavity, whereas the $n = 7$ and $n = 9$ spin wave modes are already in an intermediate coupling regime and need to be analyzed separately.

Additionally we observe a secondary anti-crossing (Fig. 7.3) at a field higher than the fundamental mode, which stems from an unidentified mode. A similar feature was found in other experiments [39] and has been interpreted in the same manner. In our data, we can clearly distinguish between the fundamental mode and this additional mode – simply by remembering that the relative intensity and coupling strength is expected to be higher for the fundamental mode. Possible origins for this additional mode are an inhomogeneous sample or a gradient in the magnetic properties across the film thickness [167]. Lastly, we note that the recorded signal in the reflection parameter is completely symmetric upon magnetic field reversal.

Next, we turn to the voltage-detected response of the system which is shown in Fig. 7.3 (d-f). Contrary to the reflection parameter, the voltage signal reverses sign on inverting $\mu_0 H_0$ Fig. 7.3 (d). The lineshape that we record for all individual modes is completely symmetric as far as they can be clearly distinguished from each other. This is the anticipated signature of a voltage caused by spin pumping only in an FMI/NM bilayer [157]. We thus conclude that we observe a signal purely caused by spin pumping and not by any rectification effect. In an FMI/NM bilayer ($\rho_{\mathrm{YIG}} \geq 10\,\mathrm{G\Omega\,m}$) [168] rectification can only arise from a change of the spin Hall magneto resistance (SMR) in the normal metal in combination with a high frequency current in the Pt. According to model calculations [157], this effect is negligible for the system we investigate because of the small magnitude of the SMR effect ($< 0.1\%$). This notion is further corroborated by the

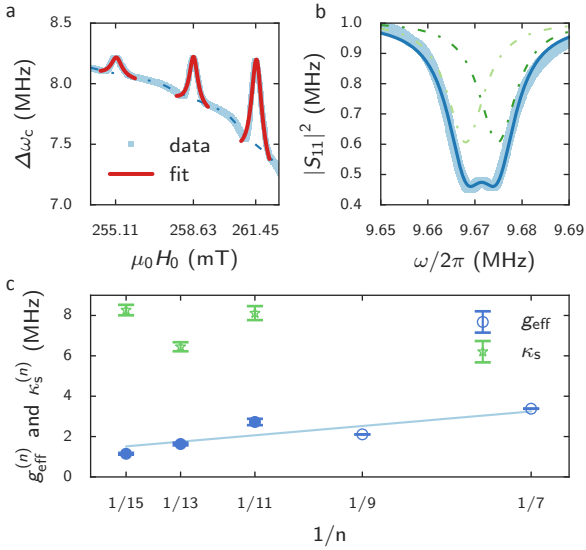

Figure 7.6: (a) Linewidth κ (light blue) from fits of a Lorentzian to frequency cuts at fixed fields. Fitting Eq. (6.6) for each spin wave resonance enables extraction of the coupling strength for weakly coupled spin waves. **(b)** For the more strongly coupled spin waves $n = 7$ and 9 (shown is $n = 7$), we model a cut at constant field $\mu_0 H_0 = 266.17\,\mathrm{mT}$ (light blue) with the sum of two Lorentzian absorption peaks (dashed, sum as solid dark blue line) and extract $2g_{\mathrm{eff}}/2\pi$ from the splitting of the centers of the distributions (cf. Sec. 6.2.1). **(c)** Spin wave–cavity coupling strength $g_{\mathrm{eff}}^{(n)}$ and spin decay rate $\kappa_s^{(n)}$ as a function of the inverse mode number. Also displayed is the predicted $1/n$ behavior. This figure is adapted from Ref. [MF2].

fact that the change in lineshape expected for rectification type signals is not visible in our data. Apart from the spin wave modes, which are well resolved in the DC voltage signal, we can also clearly see the electrically detected spin pumping voltage originating from the hybridized system of cavity and fundamental FMR mode (the main anti-crossing). As mentioned above, this strongly hybridized mode can, however, pump spin current into the normal metal only very inefficiently and thus the observed DC voltage is small. In the voltage-detected response, we can distinguish the spin wave modes and their coupling to the cavity mode too (Fig. 7.3 (d-f)). Fig. 7.5 (b) shows the $n = 7$ spin wave mode with the same model of two coupled harmonic oscillators as in Fig. 7.5 (a). The resonance position and dispersion of the spin wave reproduces the behavior detected via the microwave reflection. The anti-crossing that is visible in the microwave reflection can not be clearly observed in the voltage-detected response for this weakly coupled mode. This is due to the fact that the voltage signal is strongest when the hybridization is largest. For a weakly coupled mode, due to the large linewidth, the signal from the upper and the lower branch of the anti-crossing overlap giving rise to the observed shape.

The upper panels (b-d) of Fig. 7.7 show the change in cavity reflection as we gradually increase the coupling of the cavity to the feed line and thus increase the cavity decay rate. Starting from the critically coupled case (internal cavity losses are equal to losses into the feed line) in panel (a) to a highly overcoupled cavity (losses into the cavity feed line dominate the cavity's decay rate) in panel (b), we clearly see an increase in the cavity line width up to the point were the unperturbed cavity is no longer recognizable.

This changes the appearance of the magnetic resonance drastically: In the critically coupled case the cavity also acts as filter for the probing microwaves. Thus, the resonances can not be observed at frequencies far from the unperturbed cavity resonance frequency. Therefore, no resonant absorption is observed at 9.80 and 9.50 GHz in Fig. 7.7 (b). As the quality of the cavity and thus the quality of the filter is reduced, the resonances can be observed over a broader frequency range. In the intermediate case shown in panel (c), effects of the magnon-cavity coupling can still be observed. The fundamental mode's dispersion is distorted near the cavity resonance frequency. In the extremely overcoupled case, the microwave reflection $|S_{11}|$ is essentially flat over the observed frequency range at frequencies where no FMR is expected (panel d). The response of the system then shows the dispersion of the magnon system directly. Multiple diagonal lines of high absorption corresponding to the dispersion of the individual

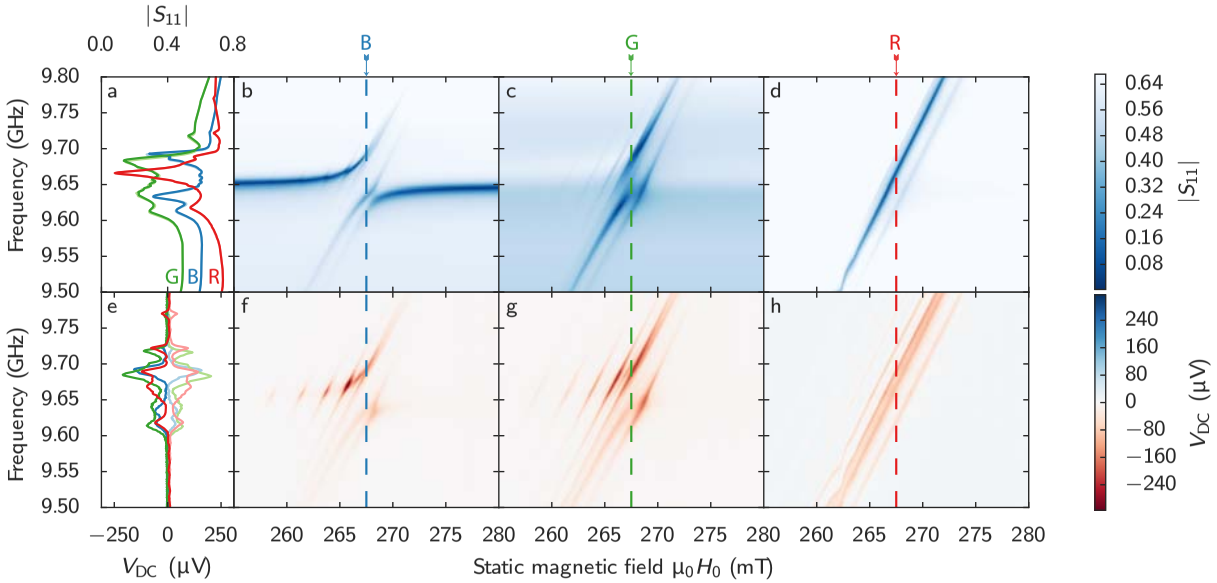

Figure 7.7: Increasing the coupling of the cavity to the feed line (from left to right) increases the cavity loss rate κ_c and thus line width $\Delta\omega/2\pi$. This enables experimental control of the transition between strong and weak coupling. **(b-d)** Microwave reflection. **(f-h)** DC voltage. **(a, e)** Line cuts at fixed field ($H_0 = \pm 267.5\,\mathrm{mT}$) are shown for the different coupling regimes (R, G, B and corresponding colors) in both reflection (a) and voltage (e) measurements. They clearly show the merging of the two dispersion curves during the strong/weak transition. Cuts at positive field (intense colors) and negative field (pale colors) again confirm the symmetry, $V(-H_0) = -V(H_0)$ and $S_{11}(-H_0) = S_{11}(H_0)$. This figure is adapted from Ref. [MF2].

spin wave modes can be observed. From their slope, the true g-factor and the effective magnetization M_{eff} can be estimated. For the well separated $n = 9$ spin wave mode, we extract $g = 2.0$ and $M_{\mathrm{eff}} = 147\,\mathrm{kA\,m^{-1}}$ which are both in good agreement with corresponding values for YIG reported in the literature (Ref. [46, 164] and Chap. 3).

In the same way as the cavity line width, the cavity decay rate increases from left to right and, in turn, the microwave magnetic field strength h_{MW} in the cavity decreases. For the already weakly coupled spin wave modes the spin pumping voltage decreases with decreasing microwave magnetic field strength h_{MW} (indicated by the higher S_{11} parameter) in the cavity. The DC spin pumping voltage amplitude corresponding to the fundamental mode (Fig. 7.7 (f-h)) does, however, not decrease for lower Q-factors but stays approximately constant. This behavior can be understood considering that the absorbed power of the cavity-spin system stays approximately constant when changing the cavity decay rate (Fig. 7.7 (a)) and the fact that the absolute effective coupling strength g_{eff} does not change when changing the cavity decay rate.

The best measure of the true magnon spectrum and line widths of the spin system can be extracted from the highly overcoupled case (Fig. 7.7 (d, h) and Fig. 7.8). There, the magnon-photon coupling is negligible compared to the cavity loss rate and therefore, the magnon-cavity mode hybridization distorts the dispersion only marginally. A mode that strongly couples with the cavity, on the contrary, can vanish completely in the fixed-frequency spectrum. This is shown exemplarily in Fig. 7.8 (a): In the weakly coupled case (cavity and feed line are highly overcoupled), the fundamental mode is easily distinguishable by its amplitude. In the strongly coupled case (critical cavity feed line coupling), however, the fundamental mode can only be observed as a broad slope in the data and linewidth or resonance position can not be extracted. The same situation is observed in the spin pumping voltage (Fig. 7.8 (b)). There, the intensity connected with the fundamental mode is reduced even further by the low spin pumping efficiency of a strongly hybridized mode and by the fact that the maximal spin pumping voltage appears at a different frequency than the cavity resonance frequency. In the weakly coupled case, on the other hand, the fundamental mode appears as a distinct peak. We finally note that we observe the described anti-crossing due to the magnon-photon coupling and thus the distortion of the lines in a fixed-frequency experiment (with the cavity tuned to high Q, as usually done in cavity-based FMR experiments) already for sample volumes as small as $V = 2 \times 10^{-3}\,\mathrm{mm^3}$ in the case of YIG ($M_{\mathrm{s}} = 147\,\mathrm{kA\,m^{-1}}$) [46]. These

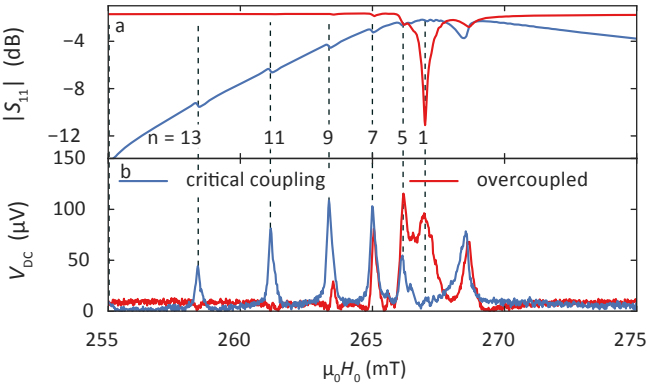

Figure 7.8: Line cuts of (a) reflection parameter and (b) DC voltage at the resonator frequency $\omega_c\,(H_0 = 0) = 9.651\,\mathrm{GHz}$. In the strongly coupled magnon-photon case (blue lines, cavity and feed line are critically coupled) the only indication of the fundamental mode ($n = 1$) is the large slope in $|S_{11}|$ whereas in the weakly coupled case (red lines, cavity and feed line are highly overcoupled) the magnon spectrum is accurately and clearly reproduced. This figure is adapted from Ref. [MF2].

sample volumes are easily achieved for LPE grown samples, suggesting that in most cavity FMR experiments (e.g. Ref. [169]) the effects of the coupling need to be taken into account in order to yield accurate results. This fact also holds in particular for magnetic resonance setups that employ an automatic frequency control.

7.4 Conclusions

In this chapter, we presented systematic measurements of spin pumping in a YIG|Pt bilayer in different regimes of the magnon-photon coupling strength. We use a micrometer thick YIG film sample, which allows to reach the strong coupling regime at room temperature due to its low damping of magnetic excitations (Chap. 3). For the fundamental FMR mode, we find an effective coupling strength of $g_{\mathrm{eff}}^{(1)}/2\pi = 22.7\,\mathrm{MHz}$ which gives a single spin coupling rate of 0.1 Hz. The characteristics of the coupled magnon-photon system fit well to the established theory and are consistent with recent results on similar samples. In particular, the single spin coupling

rate is in reasonable agreement with the results of the single spin coupling (0.4 Hz) that we extracted in the previous chapter (Sec. 6.3) for the coupling of a GdIG sample to the same cavity at low temperatures. The slight discrepancy may be attributed to a different placement and shape of the sample and a change in the cavity's mode profile due to the bond wires and the platinum layer.

Simultaneously, we recorded the electrically detected spin pumping signal of the fundamental mode. By changing the cavity's decay rate, we were able to tune the system from the strong to the weak coupling regime. The evolution of the spin pumping signal of the fundamental mode has been analyzed qualitatively and follows the predictions of Lotze [154]: In the strongly coupled magnon-photon system the spin pumping efficiency is reduced as the precession cone angle is smaller than in the weakly coupled case. Additionally, we were able to observe the coupling and the electrically detected spin pumping signal of several spin wave modes with distinctly different coupling strengths. The coupling strengths of the spin waves follow the theoretically expected $1/n$ scaling predicted by Cao et al. [145]. We used this scaling behavior to disentangle contributions of higher order spin waves and the fundamental mode to the observed main anti-crossing. Furthermore, we experimentally demonstrated the implications of strong coupling on fixed-frequency FMR experiments. We conclude that small sample volumes or a highly overcoupled cavity are mandatory for a qualitatively and quantitatively correct evaluation of the magnon spectrum and damping.

CHAPTER 8

SUMMARY

In this second part of the thesis, we investigated the magnon-photon coupling of two ferrimagnet–microwave cavity hybrid systems in detail. We described and critically compared different methods and approximative models used to extract the coupling rate and the magnon and cavity relaxation rates from the field and frequency-dependent microwave reflection parameter S_{11}. In particular, we find that the often-used approximative method of Herskind et al. [146] for the weak coupling case introduces a fairly large error on the extracted rates and should therefore – if possible – be avoided. Instead, the here-developed analysis of the full field-frequency map of S_{11} is often (especially for simple FMR dispersions with only a single mode) a viable alternative. Experimentally, we use two distinctly different approaches to tune in and out of the strong coupling regime that have not been reported for such hybrid systems in the literature before:

In the first approach (Sec. 6.3), we vary the coupling rate g_{eff} by changing the magnetic moment of a magnetically ordered system that couples to the cavity. To achieve this, we use a compensating ferrimagnet (gadolinium iron garnet) that changes its magnetization strongly with temperature while still remaining in a magnetically ordered state. In this way, we are able to tune in and out of strong coupling using a single sample as it has been shown previously only for unordered, paramagnetic samples. Apart from this, our detailed analysis of the complete field and frequency dependence of the reflection parameter S_{11} sets the experiments apart from most work previously reported in the literature. We successfully model and fit the

reflection parameter and thereby faithfully extract the coupling, magnon and cavity decay rates even for the intermediately strong coupled regime.

In a second experiment (Chap. 7), we electrically detect the magnetic excitations using spin pumping in a ferrimagnet/normal metal (YIG/Pt) bilayer in a cavity. We show that, as expected theoretically, the effect of spin pumping stays effective but shows a reduced efficiency when the system is tuned into the strong coupling regime. In this experiment, we achieve the transition from the weak-coupling to the strong coupling regime by changing the decay rate of the cavity. For this purpose, we tune the external loss rate of the cavity by adjusting the mechanical cavity–feed line coupling mechanism. This approach allows to change the ratio of cavity decay rate and magnon-photon coupling rate in a wide range and thereby allows to investigate spin pumping in both, the weak and the strong coupling regime. Furthermore, we investigate the electrical spin pumping signal of multiple perpendicular standing spin wave modes of the YIG thin film. We quantitatively analyze how the magnon-photon coupling rate and the spin pumping signal of the modes varies with the mode number. For higher mode numbers, a smaller effective magnetization couples to the cavity and hence, the mode-number dependent analysis provides a third approach to access different magnon-photon coupling regimes. The fact that this approach does not require changing the sample, holds the advantage that spin pumping can be investigated independently of the interface quality which typically varies between samples.

In summary, we presented a comprehensive study of the magnon-photon coupling in ferromagnet–microwave cavity hybrid systems with a focus on the tunability of the coupling. Our results improve the experimental understanding of this type of hybrid systems and help to predict their behavior upon changing temperature, the cavity and magnetic properties. They are a step on the way to implementing quantum hybrid systems with an electrical readout via spin pumping.

CHAPTER 9

CONCLUSIONS AND OUTLOOK

The presented thesis is divided into two main parts: “Broadband ferromagnetic resonance” (Part I) and “Cavity FMR” (Part II). This structure was chosen because the two parts do not only use a different experimental approach but also have a different research goal: Part I addresses fundamental magnetism research that aims at improving the understanding of the microscopic mechanisms in magnetic materials using ferromagnetic resonance (FMR). Part II on the other hand—while treating a very fundamental topic too, namely the interaction of magnons, photons and spin currents—is much more applied. In this second part, FMR is not only used as a looking glass to understand a state that exists in nature but instead, we artificially combine two systems and use FMR to manipulate and study the hybrid system.

However, we might also have grouped the research in one “Yttrium iron garnet (YIG) ” and one “Gadolinium iron garnet (GdIG)” chapter instead. For both materials, we first conducted a fundamental study of the magnetic properties and then used the material in a more applied experiment where we study the interaction of the material with photons and analyze spin currents in a bilayer in detail. This highlights the fact that applied research, which often gets a lot of attention, is not possible without fundamental research. Magnetism research in particular benefits from the strong foundations that have been laid by the many fundamental and material

science studies in the mid of the 20th century. Still, it is necessary to revisit these foundations and to confirm, improve and extend the understanding of magnetic materials.

Charles Kittel, one of the pioneers of magnetism research, noted that YIG is to ferromagnetic resonance research what the fruit fly is to genetics research [94]. As such, especially for its exceptionally low magnetic damping, YIG was the subject of many studies since it was first synthesized in the 1950s and it seems like the fundamentals are clear. One major review of its properties is the "Saga of YIG" by [45] in 1993. The review summarizes 40 years of research but also questions some of the results and provides new theoretical descriptions (cf. Chap. 3). Our systematic broadband FMR experiments described in Chap. 3 provide an important link between the recent broadband studies on YIG thin films and the mostly single-frequency studies from the 1960s. The extracted temperature dependence of the resonance linewidth, which is the focus of our study, provides information on the microscopic magnetization damping mechanisms in YIG. A quantitative model of these mechanisms requires detailed knowledge of the magnon spectrum of YIG. Just recently, a preprint for the article "The final chapter in the saga of YIG" by Princep et al. [170] appeared. In the manuscript, the authors present novel inelastic neutron scattering data of YIG. Using inelastic neutron scattering, the magnon spectrum of a material can be probed, which is essential to the fundamental understanding of the magnetism and, in particular, the magnetization damping of YIG. The title of the manuscript is, however, somewhat ambitious and it can be expected that there will be more research aimed at understanding the microscopic processes in YIG and that we have indeed not reached the last page of the saga of YIG. One further contribution may come from the recent advances in terahertz (THz) spectroscopy, in which spintronic emitters and detectors of THz radiation have been developed [171]. These novel sources are ideally suited to study the field dependence of the magnon spectra of YIG which is highly relevant for predicting the transport properties of pure spin currents in YIG [172]. On the other hand, using YIG (or any other insulating ferromagnet) as the ferromagnetic material in such spintronic emitters may provide more insight into the physics behind the generation of THz pulses as no charge current in the ferromagnet needs to be considered in the theoretical description. Lastly, our work on the strong coupling of a YIG|Pt bilayer to a microwave cavity aids to the understanding of the spin pumping effect in the strong coupling regime. Using spin pumping and its inverse effect (spin transfer torque), electrical manipulation and read-out of the magnetic

excitations is possible and, using the coupling to a microwave cavity, can even be performed non-locally. Since our publication on this topic, this has already been realized in parts [173]. If the generation, storage, transmission and retrieval of a quantum state is envisioned, millikelvin temperatures are finally required. For this temperature regime, a damping study of YIG which will also give further insight into the damping mechanisms of YIG is still missing.

GdIG has the same crystalline structure as YIG but hosts an additional magnetic Gd^{3+} ion that couples comparatively weakly to the Fe^{3+} ions. Hence, the magnon spectrum gets considerably more complex and holds features that give rise to quite peculiar signatures in spintronic effects that depend on the thermal occupancy of optical magnon modes [174]. As until recently for YIG, reliable inelastic neutron scattering data that allow to deduce the magnon spectrum of GdIG do not exist. In particular around the magnetic compensation point, knowledge of the magnetic phase diagram and the magnon spectrum is needed for reliable predictions of these effects. As one of the optical modes of GdIG exhibits a comparatively low excitation energy close to the magnetic compensation point, FMR already provides some insight. Using the technological improvements of broadband FMR spectroscopy presented in Chap. 2 and especially Sec. 2.2.4, we were since able to observe and study this exchange mode in a GdIG single crystal which is the topic of ongoing studies. Such data provides a link between the common broadband FMR data as in Chap. 4 and the ultimately needed inelastic neutron scattering or THz spectroscopy data. Our work on the temperature dependence of the magnetic anisotropy in a GdIG thin film (Chap. 4) is a first step towards optical or spin torque switching of the magnetization of an insulating ferrimagnetic garnet. The possibility to dope iron-garnets with different rare earth elements and thereby tuning their magnetic properties makes these finding even more interesting from an application point of view. For this, and also from a fundamental point of view, there are still many open questions and detailed studies of the magneto-optical properties of GdIG are required. Also, the microscopic mechanism causing the intrinsic damping of magnetic excitations and especially the increase in damping close to the compensation point reported in Chap. 4 has yet to be explained comprehensively on the basis of experimental data. Provided single crystalline samples of sufficient quality, magnetic resonance spectroscopy can be used to gain a better understanding of the relaxation processes and the interplay of ferromagnetic and antiferromagnetic magnons. For this task, the site-specific nuclear magnetic resonance method

may help to distinguish between different contributions to the relaxation, but also broadband FMR provides valuable information.

Finally, we would like to conclude that FMR is a very versatile and well suited tool for the study of magnetic properties and the magneto-dynamics of magnetically ordered materials. The improvements to the broadband FMR setup and data analysis achieved during this doctorate provide solid basis for future research. Furthermore, iron garnets such as YIG and GdIG are interesting model systems for ferrimagnetic order and provide a convenient platform to study magneto-dynamics in a variety of phases that span from strong ferrimagnetism to antiferromagnetism. On this account, we provide a detailed analysis of the magnetic properties and, in particular, the temperature-dependent damping of YIG and GdIG. The combination of the strong coupling of such insulating ferrimagnets to microwave resonators and spin pumping were investigated in detail in the course of this doctorate. The results help to understand the behavior of such a hybrid system and are a stepping stone on the way to a remote detection and manipulation of the magnets state via electrical currents.

APPENDIX A

APPENDIX

A.1 Analysis of 2D (FMR) data in python

In the last three decades the way solid state physics is performed changed—and is still in the process of changing—due to the increasing convenience to record measurement data easily using a computer. This change provides a challenge to uphold good scientific practices as selective data recording and analysis, for example, gets easier and more tempting when the setup is automated to the point where a measurement can be reproduced by the mere click of a button. It, however, also holds a big potential as it allows to make the sample fabrication, treatment, data recording and analysis much more transparent and reproducible. A open source database system that holds all samples and their respective preparation steps of a research institute and additionally provides an easy way of sharing this information with collaborators or accompanying a scientific publication is desirable.[1]

[1] Unfortunately, developing such a database was beyond the scope of this doctorate. This is usually the case and turns out to be a structural deficit that may be solved if institutions like

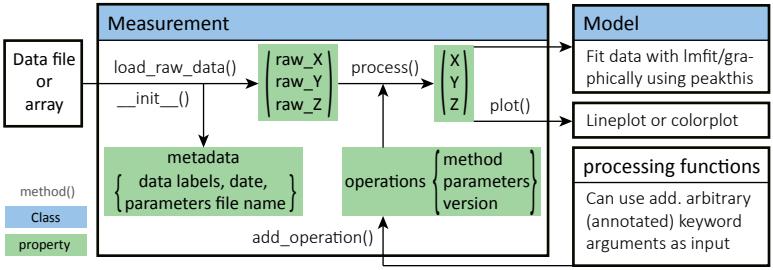

Figure A.1: Block diagram of the key components of the `bbfmr` package. The `measurement` objects manage loading and processing of the measurement data. The objects can additionally be (un)serialized and saved (loaded) as JSON data using `jsonpickle`.

This topic set aside, also the data analysis can be made transparent and reproducible by publishing the programs and the data sets used to reach the published conclusions. In the following we present a framework for the analysis of 2D measurements that allows to conveniently post-process and model data and is publicly available at `https://github.com/HaMF/bbFMR`.

The framework is designed to (but not limited to) processing magnet resonance spectroscopy data that are recorded as function of two variables like frequency and field. The challenges that are faced is that often, the data files are large ($> 500\,\mathrm{MB}$) and multiple processing steps are necessary to visualize or fit the data. As mentioned in Sec. 2.2.4, there are already various different methods of background removal. An easy way of applying these methods or implementing a new one is therefore of interest for a quick evaluation of the data. These methods are not implemented in the measurement software itself yet and should at least be provided in a separate (reusable) library (*separation of concerns*). The presented `bbfmr` package provides such a library.

`bbfmr` is structured as shown in Fig. A.1: The core component is the `Measurement` class that handles the raw data and contains metadata (such as the denomination of the X and Y axis as e.g. frequency and field, or the parameters needed to load the data). The actual loading of data files is im-

the *Deutsche Forschungsgemeinschaft* choose to support such open source endeavors on a long-term basis.

plemented in children of the base `Measurement` class that are adapted for different measurement protocols. One example is `bbfmr.measurement.vna.VNAMeasurement` which reads binary TDMS data files of typical frequency swept FMR experiments at several magnetic fields generated by the (non-public) "DR4ever" LabVIEW measurement program. Another example is `bbfmr.measurement.vna.VNAReferencedMeasurement` which reads the same kind of data file but performs the "moving field reference" background removal method described in Sec. 2.2.3 transparently. The various models, their parameters and quirks are listed in the documentation of the `measurement` module of `bbfmr` and its submodules. The second component of `bbfmr` are various processing operations (functions). They are contained in the `bbfmr.processing` module and need to have a signature as follows:

```
def processing_operation(X,Y,Z, *args, **kwargs):
        # Perform calculations
        return X, Y, Z
```

By calling `add_operation(processing_operation, args, kwargs)` of the `Measurement` object, the function `processing_operation` and the supplied arguments (`args`) and keyword arguments `kwargs` are appended to the operations stack. Upon adding an operation, it is automatically executed with the last calculated X, Y and Z arrays of the `Measurement` object as input. If `delay=True` is provided as an argument to `add_operation()`, the operation is not executed right away and the last processing result in the X, Y and Z properties are unchanged. Upon calling the `process()` method of the `Measurement` object, all operations contained in the stack are executed in the order in which they have been added. Note that the raw data is retained in the `raw_X, raw_Y` and `raw_Z` properties in order to allow recalculation of the processed data (and hence also removing or replacing operations in the stack using `remove_operation()` and `replace_operation()`) at any time. For very large data sets, this can be problematic. In this case, the raw data can be unset after loading which, of course, renders `process()` useless.

The processed data can be plotted conveniently using `matplotlib` (if available) using the `plot()` method of the `Measurement` object which will automatically produce either a line graph or a color plot of the data.

The physical core of `bbfmr` are the (ferromagnetic resonance) models contained in `bbfmr.models`. The models are `lmfit` [175] models which can be used to fit the processed data as described in the excellent `lmfit` documentation. Furthermore, `bbfmr` implements a `ComplexModel` which

takes complex-valued (e.g. `Complex128`) Z arrays as input and compares the real and imaginary part simultaneously with the real and imaginary part of the (also complex-valued) model result using `lmfit`. Currently, `bbfmr.models` contains models for the ferromagnetic dispersion considering various anisotropies, the Polder susceptibility in field and in frequency space and the ferromagnetic damping. We refer the reader to the documentation of the module and the Models for detailed information on the Models that includes references for the derivation of the model and advise on which units are used. Finally, most models contain relatively robust methods that guess initial fit parameters.

In the following code listing, the use of the library is demonstrated. First, the measurement is loaded with the `VNASeparateFieldsMeasurement` `Measurement` class that averages the magnetic field reading taken before and after the frequency swept measurement of the transmission S parameter. Using a series of processing operations, the background is removed using *derivative divide* (cf. Sec. 2.2.4) and the data is reduced to the region of interest. Finally, the data is cast to real values and the result is plotted. In a second step, a slice of the data at 2 T is extracted using the `cut` processing operation and the real and imaginary part of the processed data is plotted. This slice is fitted using the `VNAFMR_EllipsoidDifferenceQuotientSphereModel` model and the resulting best fit is displayed in the same graph as the data. The `recommend_roi()` method of the susceptibility models allows to fit only the data close to the automatically detected peak which allows to automatically fit many of these cuts. The resulting figure is, apart from minor formatting changes, identical to Fig. 2.8.

```
1  ## Load data from file, perform moving field background removal
2  from bbfmr.measurement.vna imort VNASeparateFieldsMeasurement
3  import bbfmr.processing as bp
4  m = VNASeparateFieldsMeasurement(fname="measurement_file.tdms"))
5  m.set_xlabel("$\mu_0␣H_0$␣(T)")
6  m.set_ylabel("$\omega/2\pi$␣(Hz)")
7  m.set_zlabel("Signal␣[a.u]")
8
9  ## Plot colormap
10 import matplotlib.pyplot as plt
11 ax_color = plt.subplot(211)
12 m.operations = []
13 m.add_operation(bp.derivative_divide, modulation_amp=4, delay=True)
14 m.add_operation(bp.real, delay=True)
15 m.add_operation(bp.limit, x_slc=slice(20, −400, 1))
16 mesh, cbar = m.plot(rasterized=True, cmap="Blues_r", ax=ax_color)
17
```

```
## Plot real and imaginary part for cut at constant field
ax_cut = plt.subplot(212)
for op in [bp.real, bp.imag]:
    m.operations = []
    m.add_operation(bp.derivative_divide, modulation_amp=4, delay=True)
    m.add_operation(bp.conjugate, delay=True)
    m.add_operation(bp.linear_moving_limit,
                    intercept=−2.9610e+10,
                    slope=2.8734e+10, span=500,
                    delay=True)
    m.add_operation(bp.limit, x_slc=slice(20, −400, 1), delay=True)
    m.add_operation(bp.cut, x_val=2, delay=True) # cut at H_0=2T
    m.add_operation(op)
    m.plot(ax=ax_cut, marker='s', markersize=3)

## Fit susceptibilit model to cut and plot best fit
m.operations.pop() # Remove last operation
m.process() # Recalculate m.X, m.Y, m.Z
B = np.squeeze(np.unique(m.X))
f = np.squeeze(m.Y)
S = np.squeeze(m.Z) # complex−valued

from bbfmr.models.susceptibility import VNAFMR_EllipsoidDifferenceQuotientSphereModel
model = VNAFMR_EllipsoidDifferenceQuotientSphereModel()
params = model.guess(x=f, data=S,
                     mod_f=2.4e−3∗28e9, # modulation amplitude in [Hz]
                     B=B, phi=−1.6)
params["phi"].vary = True
params["Z"].value = params["Z"].value/100
roi = model.recommended_roi(f, S, 3)
fit = model.fit(x=f[roi], data=S[roi], params=params)

ax_cut.plot(f[roi], np.real(fit.best_fit), '−')
ax_cut.plot(f[roi], np.imag(fit.best_fit), '−')
ax_cut.set_xlim([fit.params["f_r"].value−0.6e9, fit.params["f_r"].value+0.6e9])
```

A basic user interface (UI) that interactively plots `Measurement` objects, allows to graphically choose and load the data file is available in `bbfmr.gui`. In this interface, all available processing operations can easily be applied and modified which is aimed at a quick first evaluation of a field-frequency spectrum. Finally, a `Measurement` object, including all processing steps and metadata but excluding the actual data, can be serialized and stored as JSON file. On loading this JSON file with `jsonpickle`, the raw data is automatically retrieved from the original location and the original processing operations are performed. The following listing demonstrates saving and loading a `Measurement` object from file:

```
import jsonpickle
from bbfmr.measurement.vna imort VNASeparateFieldsMeasurement
import bbfmr.processing as bp

m = VNASeparateFieldsMeasurement(fname=path.join(data_dir, fname_tdms))
m.add_operation(bp.derivative_divide, modulation_amp=2)
m.save(fname="spectrum.measurement.json")
```

```
        # save() is a shortcut for calling jsonpickle.decode()
        # and saving the output to file

with f = open("spectrum.measurement.json"):
        m2 = jsonpickle.decode(f.read()) # identical to m
```

Even with rather robust initial parameter guessing and the automatic determination of the region-of-interest, manual intervention is often necessary for a successful fit. In the analysis of FMR data for example, this is the case when multiple resonance absorption lines (anti-)cross as observed in Chap. 3. Therefore, a graphical tool called `peakit` based on `pyqt` [2] was extended to allow for batch-fitting slices of 2D (complex-valued) data. The tool allows to fit the data to composite models, i.e. multiple peaks or background contributions. For every model the initial parameters and the region-of-interest can be automatically determined and manually adjusted. It allows for a quick overview over the fitted parameters and has the functionality to recall and perform fits of certain slices again, thereby providing and convenient way to spot and correct failed fits. This tool is freely available too at `https://github.com/HaMF/BatchPeakThis`.

A.2 Broadband FMR cryogenic dip stick

In this section, the broadband dip sticks that are used for temperature-dependent ferromagnetic resonance up to 40 GHz in a helium gas flow cryostat are described in detail. Two nominally identical dip sticks have been manufactured called *UHF1* and *UHF2* (ultra high frequency 1 and 2). The dip stick design is based on the practical experiences gained with the 4-port dip stick [71]. The major change to the previous designs was to avoid any magnetic materials near the AC signal lines, and to reduce the number of connectors in the microwave cabling. In this way, a sufficiently flat and magnetic field independent transmission (cf. Chap. 2) is achieved.

The dip stick features two microwave cables, and is therefore less versatile than the previous 4-port version but optimized for highly sensitive, high frequency broadband FMR measurements. It additionally features 24 DC measurement leads, a Cernox temperature sensor and a heater for temperature stabilization. The sample holder base (Fig. A.2) serves as a flexible platform for various experiments The default configuration for

[2] PeakThis/peakit was developed by Clemens Prescher and is available at `https://github.com/CPrescher/PeakThis` under the GPL license.

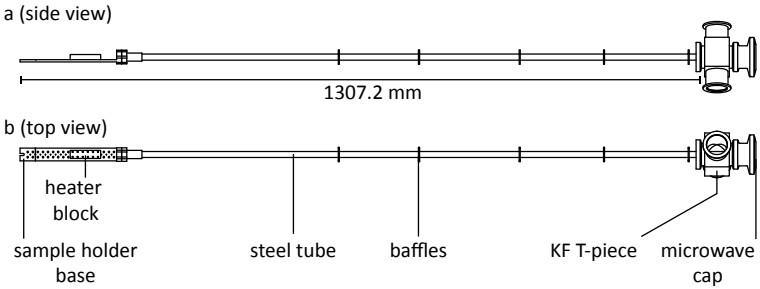

Figure A.2: Schematic view of the parts of the dip stick establishing the naming convention for this document. Not shown are the KF 40 blind flanges with Ø15 mm and Ø19 mm bores for the DC Fischer connectors.

broadband FMR containing a CPW with its plane parallel to the dip stick axis is shown in Fig. A.6.

The total distance from the lower end of the KF (*Klein* flange) T-piece at the top of the dip stick (excluding the final centering ring) to the marked sample placement (cf. Fig. A.6) is 1307.2 mm (design) . From the center of magnet, the sample holder base extends 30 mm towards the bottom of the variable temperature inset (VTI). Additionally to this distance, the microwave cabels extend 10 mm further.

The maximal diameter of the parts of the dip stick that enter the VTI of the cryostat is given by the baffles and is 28 mm.

DC cabling

Heater and temperature sensor

The Heater and temperature sensor are connected to the 10-pole connector (Fischer DBEE 1031 Z010-130) at the top end of the dip stick with the pin assignment as depicted in Fig. A.3 (a) and Tab. A.3 (b). The wires are routed in a common protective fabric hose as twisted pairs on the outside of the stainless steel tube. All three pairs are (non oxygen free high conductivity) copper wires with insulating varnish. Pair 1 connects the heater and has a diameter of 0.25 mm. Pairs 2 and 3 connect the temperature sensor and have a diameter of 0.1 mm. The heater cartridge is fitted into a copper block that is screwed onto the sample holder base of the dip stick as shown as a technical drawing in Fig. A.3 (c) and is directly soldered to cable

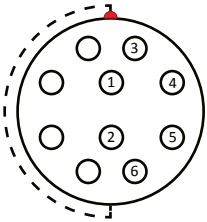

(a) Fischer 10-pole connector pin assignment (top view of the socket, solder joints on the back).

Pin	Pair	Function
1	1	Heater
2	1	Heater
3	2	Sensor I_+
4	2	Sensor I_-
5	3	Sensor V_+
6	3	Sensor V_-

(b) Assignment of the 10-pole connector pins (top view of receptacle, solder joints on the back).

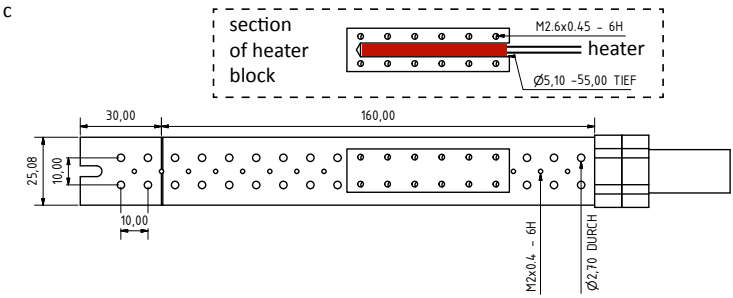

(c) Sample holder base showing the mounting of the heater.

Figure A.3: Heater and temperature sensor cabling.

pair 1. The temperature sensor is connected to pairs 2 and 3 by a 1.27 mm pitch pin strip and can be clamped on the sample holder base. The CPW holders (Fig. A.6) contain a hole designed to tightly hold a Cernox sensor in the AA package (8.5 mm long copper sleeve with an outer diameter of 3 mm). Using this mounting of the Cernox sensor promises a better temperature accuracy than clamping it on the sample hoder base as it is then placed closer to the sample and has a better thermal connection to the CPW holders.

DC measurement leads

There are 24 measurement leads in 12 twisted pairs available in the dip sticks. They are connected at to the 24-pole connector (Fischer DBEE 105

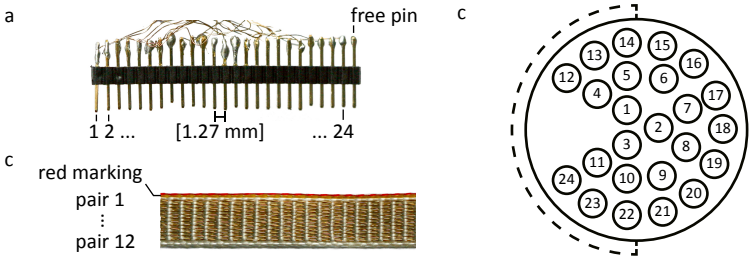

Figure A.4: (a) Pin strip at the lower end of the dip stick. **(b)** Manganin ribbon cable. Note the red color marking identifying pair 1. **(c)** Fischer 24-pole connector pin assignment (top view of the receptacle, solder joints on the back) (cmp. Tab. A.1).

Z093-80) at the top with a pin assignment as shown in Fig. A.4 (c) and Tab. A.1. The DC leads are twisted pair Manganin wires in a 24 wire ribbon that is routed through the stainless steel tube to provide some shielding from the environment. The Manganin ribbon is shown in Fig. A.4 (b). Note the red color marking which identifies pair 1. At the bottom end of the dip stick, a pin strip with pitch 1.27 mm is soldered to the Manganin wires with the wire numbers as indicated in Fig. A.4 (a). Note that the end of the pin strip which contains in an unconnected pin identifies the end with pin 24. The typical resistance of one Manganin wire is 100 Ω.

Table A.1: Assignment of 24-pole connector pin to Manganin twisted pair

Pin number	Pair number
1/2	1
3/4	2
5/6	3
7/8	4
9/10	5
11/12	6
13/14	7
15/16	8
17/18	9
19/20	10
21/22	11
23/24	12

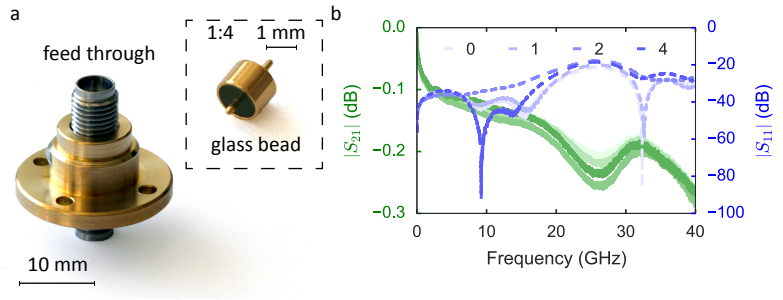

Figure A.5: (a) Fully assembled hermetic feed through and a single glass bead that is soldered into the brass part. **(b)** Magnitude of the *S* parameters of the assembled and used feed throughs. All four feed throughs show a very low insertion loss.

Temperature control

The temperature sensor used in UHF1 has the ID CX70062 and UFH2 has the ID CX73055. The sensor ID is noted at the top KF T-piece of each the dip stick.

Sensible PID parameters for the dip stick are $(P, I, D) = (200, 8, 20)$ at all temperatures below 300 K (tested on UHF1). The high value of D is required because the thermal mass of the lower cooper part is quite large and basically serves as an additional I parameter. Temperatures stabilities of 2 mK at 300 K and 10 mK at 10 K are easily achieved without further effort using a Lakeshore Model 370 AC resistance bridge. A second temperature sensor and heater can be connected using the DC measurement lines if necessary. Using a second temperature control loop (as offered by the Model 370 resistance bridge) with a sensor very close to—or even on—the sample may be helpful, when measurements are performed in which the temperature is continuously varied rather is stabilized at a certain value.

Microwave cabling

Commercially only very few hermetically sealed 2.92 mm connectors are available which additionally have either high lead times, high price or are only advertised as hermetically sealed but are not hermetically sealed after all. Therefore, in-house build hermetically sealed 2.92 mm connectors are mounted into the upper blind flange. They consist of a brass base that have Anritsu K100B glass beads soldered into the through hole (Fig. A.5 (a)).

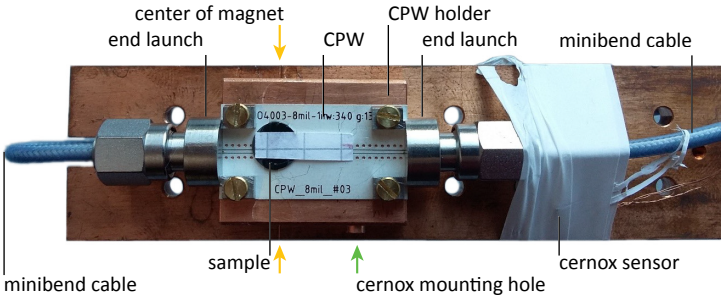

Figure A.6: Bottom end of the dip stick. The blue Minibend cables connect with SMK to the signal microwave end launches at two sides of a (in this example) 250 µm wide CPW. The CPW and end launch connectors are mounted on the CPW cooper holder that holds the (in the picture) empty shell of a Cernox temperature sensor (green arrow). (The temperature sensor in this image is hidden below the Teflon tape that is used to secure the microwave cables in place.) The center of magnet when inserting the dip stick into the cryostat is marked on the sample base (yellow arrow). Compare also to the side view in Fig. 2.3.

Note, the nominally hermetically sealed version of the glass beads is K100A. The K100B version was used because it was still on storage and for the application the leak rate is typically good enough (see below). K102F-R spark plug connectors are screwed into the brass base from both sides. Note that the glass beads are asymmetric as they are intended to launch onto a CPW on one side and be connected to a spark plug from the other side only. They have not been filed down to be symmetric, as the microwave characteristics (Fig. A.5 (b)) are already satisfactory. The dip in transmission and around 25 GHz, indicates that the impedance matching is still not perfect, however, only a minor improvement is expected from further optimization. The vacuum seal is provided by a (NBR-70 Shore A) O-ring with an inner diameter 10 mm and a thickness of 1 mm.

Two Minibend KR-1.675M cables (SMK (2.92 mm) connectors on both ends, ruggedized, 1.675 m long) assembled by Huber&Suhner are used to connect the feed throughs to two signal microwave or Southwest 292-04A-5 end launches. The Minibend cables have been chosen as the cables itself contain no magnetic materials near the center conductor (pure copper center conductor). However, the cables cannot be assembled with non-magnetic SMK connectors by Huber&Suhner. The experiences with

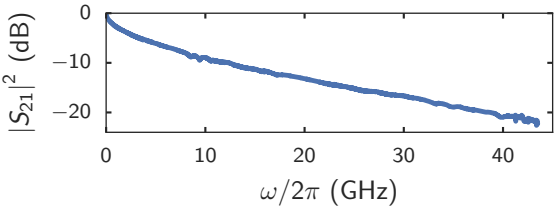

Figure A.7: Magnitude of the microwave transmission S_{21} of the UHF 1 dip stick with an empty 5 mil CPW. The attenuation of the cables connecting the dip stick to the VNA has been subtracted. S_{21} is free from resonant modes up to 40 GHz indicating an overall good impedance matching through the assembly.

the flexible cables that can be easily fitted to the dipstick and the factory assembly is entirely positive. The sample is typically fixed on the CPW with Fixogum or Sellotape (Fig. A.6). In contrast to the previous dip-sticks, there is no protective sleeve for the sample part of the dip stick. Practical experience shows that Fixogum is a very reliable way of fixing the sample. Furthermore, the sample can not be damaged during insertion of the dip stick into the cryostat due to the geometry of the end launches.

BIBLIOGRAPHY

List of author's publications

[MF1] S. Klingler, H. Maier-Flaig, R. Gross, C.-M. Hu, H. Huebl, S. T. B. Goennenwein, and M. Weiler, "Combined brillouin light scattering and microwave absorption study of magnon-photon coupling in a split-ring resonator/YIG film system", Applied Physics Letters **109**, 072402 (2016) (cit. on p. 4).

[MF2] H. Maier-Flaig, M. Harder, R. Gross, H. Huebl, and S. T. B. Goennenwein, "Spin pumping in strongly coupled magnon-photon systems", Physical Review B **94**, 054433 (2016) (cit. on pp. 5, 92, 102, 124, 130, 133, 135, 137, 139).

[MF3] H. Maier-Flaig, M. Harder, S. Klingler, Z. Qiu, E. Saitoh, M. Weiler, S. Geprägs, R. Gross, S. T. B. Goennenwein, and H. Huebl, "Tunable magnon-photon coupling in a compensating ferrimagnet—from weak to strong coupling", Applied Physics Letters **110**, 132401 (2017) (cit. on pp. 7, 102, 114, 116, 117, 119, 120).

[MF4] S. Klingler, H. Maier-Flaig, C. Dubs, O. Surzhenko, R. Gross, H. Huebl, S. T. B. Goennenwein, and M. Weiler, "Gilbert damping of magnetostatic modes in a yttrium iron garnet sphere", Applied Physics Letters **110**, 092409 (2017) (cit. on pp. 22, 56, 60, 62–65, 68).

[MF5] H. Maier-Flaig, S. T. B. Goennenwein, R. Ohshima, M. Shiraishi, R. Gross, H. Huebl, and M. Weiler, "Note: derivative divide, a method for the analysis of broadband ferromagnetic resonance in the frequency

domain", Review of Scientific Instruments **89**, 076101 (2018) (cit. on pp. 26, 34, 40, 42, 43, 52).

[MF6]H. Maier-Flaig, S. Klingler, C. Dubs, O. Surzhenko, R. Gross, M. Weiler, H. Huebl, and S. T. B. Goennenwein, "Temperature-dependent magnetic damping of yttrium iron garnet spheres", Physical Review B **95**, 214423 (2017) (cit. on pp. 32, 40, 65–67, 71).

[MF7]H. Maier-Flaig, S. Geprägs, Z. Qiu, E. Saitoh, R. Gross, M. Weiler, H. Huebl, and S. T. B. Goennenwein, "Perpendicular magnetic anisotropy in insulating ferrimagnetic gadolinium iron garnet thin films", arXiv:1706.08488 (2017) (cit. on pp. 73, 75, 77, 79, 80).

References to scientific publications

[8]J. Bardeen and W. H. Brattain, "The transistor, a semi-conductor triode", Physical Review **74**, 230–231 (1948) (cit. on p. 1).

[9]M. Sparks, "The junction transistor", Scientific American **187**, 28–32 (1952) (cit. on p. 1).

[10]M. Bohr, *14 nm technology announcement*, Technical report, Intel, available at `http://www.intel.com/content/dam/www/public/us/en/documents/presentation/`, accessed 2017-06-28 advancing-moores-law-in-2014-presentation.pdf, 2014 (cit. on p. 1).

[11]S. Zhang and D. Zhao, *Advances in magnetic materials: processing, properties, and performance*, Advances in Materials Science and Engineering (CRC Press, 2017) (cit. on p. 2).

[12]G. Binasch, P. Grünberg, F. Saurenbach, and W. Zinn, "Enhanced magnetoresistance in layered magnetic structures with antiferromagnetic interlayer exchange", Physical Review B **39**, 4828–4830 (1989) (cit. on p. 2).

[13]M. N. Baibich, J. M. Broto, A. Fert, F. N. Van Dau, F. Petroff, P. Etienne, G. Creuzet, A. Friederich, and J. Chazelas, "Giant magnetoresistance of (001)Fe/(001)Cr magnetic superlattices", Physical Review Letters **61**, 2472–2475 (1988) (cit. on p. 2).

[14]O. E. Buckley, "High-speed ocean cable telegraphy", Bell System Technical Journal **7**, 225–267 (1928) (cit. on p. 2).

[15]D. M. Pozar, *Microwave engineering, 4th edition* (Wiley, 2011) (cit. on pp. 2, 27, 91).

[16] Y.-T. Chen, S. Takahashi, H. Nakayama, M. Althammer, S. T. B. Goennenwein, E. Saitoh, and G. E. W. Bauer, "Theory of spin Hall magnetoresistance", Physical Review B **87**, 144411 (2013) (cit. on p. 3).

[17] H. Nakayama, M. Althammer, Y.-T. Chen, K. Uchida, Y. Kajiwara, D. Kikuchi, T. Ohtani, S. Geprägs, M. Opel, S. Takahashi, R. Gross, G. E. W. Bauer, S. T. B. Goennenwein, and E. Saitoh, "Spin Hall magnetoresistance induced by a nonequilibrium proximity effect", Physical Review Letters **110**, 206601 (2013) (cit. on p. 3).

[18] F. D. Czeschka, L. Dreher, M. S. Brandt, M. Weiler, M. Althammer, I.-M. Imort, G. Reiss, A. Thomas, W. Schoch, W. Limmer, H. Huebl, R. Gross, and S. T. B. Goennenwein, "Scaling behavior of the spin pumping effect in ferromagnet-platinum bilayers", Physical Review Letters **107**, 046601 (2011) (cit. on pp. 3, 105, 123, 125, 126).

[19] A. Brataas, A. D. Kent, and H. Ohno, "Current-induced torques in magnetic materials", Nature Materials **11**, 372–381 (2012) (cit. on p. 3).

[20] K. Uchida, S. Takahashi, K. Harii, J. Ieda, W. Koshibae, K. Ando, S. Maekawa, and E. Saitoh, "Observation of the spin Seebeck effect", Nature **455**, 778–781 (2008) (cit. on p. 3).

[21] M. Weiler, M. Althammer, F. D. Czeschka, H. Huebl, M. S. Wagner, M. Opel, I.-M. Imort, G. Reiss, A. Thomas, R. Gross, and S. T. B. Goennenwein, "Local charge and spin currents in magnetothermal landscapes", Physical Review Letters **108**, 106602 (2012) (cit. on p. 3).

[22] M. P. Kostylev, A. A. Serga, T. Schneider, B. Leven, and B. Hillebrands, "Spin-wave logical gates", Applied Physics Letters **87**, 153501 (2005) (cit. on p. 3).

[23] S. Murakami, N. Nagaosa, and S.-C. Zhang, "Dissipationless quantum spin current at room temperature", Science **301**, 5638 (2003) (cit. on p. 3).

[24] A. Kamra, F. P. Witek, S. Meyer, H. Huebl, S. Geprägs, R. Gross, G. E. W. Bauer, and S. T. B. Goennenwein, "Spin hall noise", Physical Review B **90**, 214419 (2014) (cit. on p. 3).

[25] T. Silva and W. Rippard, "Developments in nano-oscillators based upon spin-transfer point-contact devices", Journal of Magnetism and Magnetic Materials **320**, 1260–1271 (2008) (cit. on p. 3).

[26] K. Kurokawa, "Some basic characteristics of broadband negative resistance oscillator circuits", Bell System Technical Journal **48**, 1937–1955 (1969) (cit. on p. 3).

[27] M. F. Collins and O. A. Petrenko, "Triangular antiferromagnets", Canadian Journal of Physics **75**, 605–655 (1997) (cit. on p. 4).

[28] A. Aqeel, N. Vlietstra, J. A. Heuver, G. E. W. Bauer, B. Noheda, B. J. Van Wees, and T. T. M. Palstra, "Spin-Hall magnetoresistance and spin Seebeck effect in spin-spiral and paramagnetic phases of multiferroic $CoCr_2O_4$ films", Physical Review B **92**, 1–8 (2015) (cit. on p. 4).

[29] Y. Onose, Y. Okamura, S. Seki, S. Ishiwata, and Y. Tokura, "Observation of magnetic excitations of skyrmion crystal in a helimagnetic insulator Cu_2OSeO_3", Physical Review Letters **109**, 1–5 (2012) (cit. on p. 4).

[30] B. Calhoun, J. Overmeyer, and W. Smith, "Ferrimagnetic resonance in gadolinium iron garnet", Physical Review **107** (1957) (cit. on pp. 4, 73, 76, 82, 116).

[31] G. F. Dionne, "Molecular field and exchange constants of Gd^{3+} substituted ferrimagnetic garnets", Journal of Applied Physics **42**, 2142–2143 (1971) (cit. on pp. 4, 7, 8).

[32] J. Helszajn, *YIG resonators and filters.* (John Wiley & Sons, 1985) (cit. on p. 4).

[33] J. D. Adam, L. E. Davis, G. F. Dionne, E. F. Schloemann, and S. N. Stitzer, "Ferrite devices and materials", IEEE Transactions on Microwave Theory and Techniques **50**, 721–737 (2002) (cit. on p. 4).

[34] S. Viola Kusminskiy, H. X. Tang, and F. Marquardt, "Coupled spin-light dynamics in cavity optomagnonics", Physical Review A **94**, 033821 (2016) (cit. on p. 4).

[35] R. Hisatomi, A. Osada, Y. Tabuchi, T. Ishikawa, A. Noguchi, R. Yamazaki, K. Usami, and Y. Nakamura, "Bidirectional conversion between microwave and light via ferromagnetic magnons", Physical Review B **93**, 174427 (2016) (cit. on p. 4).

[36] X. Zhang, C.-l. Zou, L. Jiang, and H. X. Tang, "Strongly coupled magnons and cavity microwave photons", Physical Review Letters **113**, 156401 (2014) (cit. on pp. 4, 92, 107, 124).

[37] X. Zhang, C.-l. Zou, N. Zhu, F. Marquardt, L. Jiang, and H. X. Tang, "Magnon dark modes and gradient memory", Nature Communications **6**, 8914 (2015) (cit. on pp. 4, 5, 92).

[38] Y. Tabuchi, S. Ishino, T. Ishikawa, R. Yamazaki, K. Usami, and Y. Nakamura, "Hybridizing ferromagnetic magnons and microwave photons in the quantum limit", Physical Review Letters **113**, 083603 (2014) (cit. on pp. 4, 5, 92, 115).

[39] L. Bai, M. Harder, Y. P. Chen, X. Fan, J. Q. Xiao, and C.-M. Hu, "Spin pumping in electrodynamically coupled magnon-photon systems", Physical Review Letters **114**, 227201 (2015) (cit. on pp. 4, 91, 102, 123, 124, 134).

[40] N. J. Lambert, J. A. Haigh, S. Langenfeld, A. C. Doherty, and A. J. Ferguson, "Cavity-mediated coherent coupling of magnetic moments", Physical Review A **93**, 021803 (2016) (cit. on pp. 5, 92).

[41] Y. Tabuchi, S. Ishino, A. Noguchi, T. Ishikawa, R. Yamazaki, K. Usami, and Y. Nakamura, "Coherent coupling between a ferromagnetic magnon and a superconducting qubit", Science **349**, 405–408 (2015) (cit. on p. 5).

[42] Wikimedia Commons–User:Krizu, *Bild eines synthetischen Yttriumeisengranats Einkristall mit roten Resten des Lösemittels*, published as CC-BY at `https://commons.wikimedia.org/wiki/File:Wiki-YIG.jpg` accessed online 2017-09-01, 2012 (cit. on p. 5).

[43] S. Wittekoek, T. J. A. Popma, J. M. Robertson, and P. F. Bongers, "Magneto-optic spectra and the dielectric tensor elements of bismuth-substituted iron garnets at photon energies between 2.2-5.2 eV", Physical Review B **12**, 2777–2788 (1975) (cit. on p. 5).

[44] R. Metselaar and P. Larsen, "High-temperature electrical properties of yttrium iron garnet under varying oxygen pressures", Solid State Communications **15**, 291–294 (1974) (cit. on p. 5).

[45] V. Cherepanov, I. Kolokolov, and V. L'vov, "The saga of YIG: Spectra, thermodynamics, interaction and relaxation of magnons in a complex magnet", Physics Reports **229**, 81–144 (1993) (cit. on pp. 5, 57, 68, 71, 86, 144).

[46] P. Hansen, "Anisotropy and magnetostriction of gallium-substituted yttrium iron garnet", Journal of Applied Physics **45**, 3638–3642 (1974) (cit. on pp. 5, 63, 65, 131, 132, 138).

[47]G. Winkler, *Magnetic garnets*, Tracts in pure and applied physics; Vol. 5 (Vieweg, 1981) (cit. on pp. 5, 63).

[48]G. F. Dionne, *Magnetic oxides* (Springer US, 2009) (cit. on pp. 6, 8).

[49]G. P. Espinosa, "Crystal chemical study of the rare-earth iron garnets", The Journal of Chemical Physics **37**, 2344–2347 (1962) (cit. on p. 8).

[50]R. Pauthenet, "Spontaneous magnetization of some garnet ferrites and the aluminum substituted garnet ferrites", Journal of Applied Physics **29**, 253–255 (1958) (cit. on p. 8).

[51]E. Sawatzky and E. Kay, "Some magnetic and structural properties of epitaxial garnet films prepared by rf sputtering", Journal of Applied Physics **40**, 1460–1462 (1969) (cit. on p. 8).

[52]S. V. Vonsovskii, *Ferromagnetic resonance* (Elsevier, 1966) (cit. on pp. 8, 22).

[53]A. G. Gurevich and G. A. Melkov, *Magnetization oscillations and waves* (CRC Press, 1996), p. 445 (cit. on pp. 8–10, 78).

[54]L. Landau and E. Lifshits, "On the theory of the dispersion of magnetic permeability in ferromagnetic bodies", Physikalische Zeitschrift der Sowjetunion **169**, 14–22 (1935) (cit. on p. 8).

[55]T. Gilbert, "Classics in magnetics a phenomenological theory of damping in ferromagnetic materials", IEEE Transactions on Magnetics **40**, 3443–3449 (2004) (cit. on p. 8).

[56]T. D. Rossing, "Resonance linewidth and anisotropy variation in thin films", Journal of Applied Physics **34**, 995 (1963) (cit. on p. 9).

[57]M. L. Schneider, J. M. Shaw, A. B. Kos, T. Gerrits, T. J. Silva, and R. D. McMichael, "Spin dynamics and damping in nanomagnets measured directly by frequency-resolved magneto-optic kerr effect", Journal of Applied Physics **102**, 103909 (2007) (cit. on p. 10).

[58]S. S. Kalarickal, P. Krivosik, M. Wu, C. E. Patton, M. L. Schneider, P. Kabos, T. J. Silva, and J. P. Nibarger, "Ferromagnetic resonance linewidth in metallic thin films: Comparison of measurement methods", Journal of Applied Physics **99**, 093909 (2006) (cit. on p. 10).

[59]C. Kittel, "On the theory of ferromagnetic resonance absorption", Physical Review **73**, 155–161 (1948) (cit. on p. 11).

[60] S. Bornmann, A. Schönecker, and W. Haubenreisser, "Magnetostatic mode pattern and mode spectrum analysis in finite ferromagnetic circular disks", Physica Status Solidi (a) **11**, 207–217 (1972) (cit. on p. 12).

[61] W. Brodkorb, "Switching curves of stray-field-coupled ferro–ferromagnetic multi-layer films", Physica Status Solidi (a) **8**, 141–147 (1971) (cit. on p. 12).

[62] L. Baselgia, M. Warden, F. Waldner, S. L. Hutton, J. E. Drumheller, Y. Q. He, P. E. Wigen, and M. Maryko, "Derivation of the resonance frequency from the free energy of ferromagnets", Physical Review B **38**, 2237–2242 (1988) (cit. on p. 12).

[63] L. Dreher, M. Weiler, M. Pernpeintner, H. Huebl, R. Gross, M. Brandt, and S. Goennenwein, "Surface acoustic wave driven ferromagnetic resonance in nickel thin films: theory and experiment", Physical Review B **86**, 1–13 (2012) (cit. on p. 12).

[64] P. D. Louis, "Broadband-spectroscopy of magnetic materials at low temperatures", Master's thesis (Technische Universität München, 2016) (cit. on pp. 12, 27, 29, 34, 35, 48).

[65] H. T. Nembach, T. J. Silva, J. M. Shaw, M. L. Schneider, M. J. Carey, S. Maat, and J. R. Childress, "Perpendicular ferromagnetic resonance measurements of damping and Lande g-factor in sputtered $(Co_2Mn)_{1-x}Ge_x$", Physical Review B **84**, 054424 (2011) (cit. on pp. 13, 36, 37).

[66] Y. Tserkovnyak, A. Brataas, and G. E. W. Bauer, "Enhanced Gilbert damping in thin ferromagnetic films.", Physical Review Letters **88**, 117601 (2002) (cit. on pp. 22, 105, 123, 125).

[67] G. Ghione and C. Naldi, "Parameters of coplanar waveguides with lower ground plane", Electronics Letters **19**, 734 (1983) (cit. on p. 27).

[68] I. S. Maksymov and M. Kostylev, "Broadband stripline ferromagnetic resonance spectroscopy of ferromagnetic films, multilayers and nanostructures", Physica E: Low-Dimensional Systems and Nanostructures **69**, 253–293 (2015) (cit. on pp. 27, 92).

[69] B. Rosas, *Optimizing test boards for 50 GHz end launch connectors*, Technical report, Southwest Microwave Inc. Tempe, 2011 (cit. on p. 27).

[70]T. J. Silva, C. S. Lee, T. M. Crawford, and C. T. Rogers, "Inductive measurement of ultrafast magnetization dynamics in thin-film permalloy", Journal of Applied Physics **85**, 7849–7862 (1999) (cit. on pp. 28, 34, 91).

[71]F. Hartz, "Herstellung eines Breitband-Messstabs zur Untersuchung ferromagnetischer Resonanz", Bachelor's thesis (Technische Universität München, 2014) (cit. on pp. 31, VI).

[72]O. Karlqvist, "Calculation of the magnetic field in the ferromagnetic layer of a magnetic drum", Transactions of the Royal Institute of Technology Stockholm, Sweden (1954) (cit. on p. 33).

[73]J. M. Shaw, H. T. Nembach, and T. J. Silva, "Determination of spin pumping as a source of linewidth in sputtered $Co_{90}Fe_{10}$/Pd multilayers by use of broadband ferromagnetic resonance", Physical Review B **85**, 054412 (2012) (cit. on p. 35).

[74]A. J. Berger, E. R. J. Edwards, H. T. Nembach, J. M. Shaw, A. D. Karenowska, M. Weiler, and T. J. Silva, "Evidence for a common origin of spin-orbit torque and the dzyaloshinskii-moriya interaction at a $Ni_{80}Fe_{20}$/Pt interface", arXiv:1611.05798 (2016) (cit. on p. 44).

[75]M. A. W. Schoen, J. M. Shaw, H. T. Nembach, M. Weiler, and T. J. Silva, "Radiative damping in waveguide-based ferromagnetic resonance measured via analysis of perpendicular standing spin waves in sputtered permalloy films", Physical Review B **92**, 184417 (2015) (cit. on p. 44).

[76]H. Maier-Flaig, *Analysis of broadband FMR in the frequency domain - Dataset and reference implemenation of derivative divide*, Open Science Framework e-publication, `https://osf.io/u27sf/?view_only=bc9d8bd783324875960eab1e0286e77a`, 2017 (cit. on p. 44).

[77]M. Haertinger, C. H. Back, J. Lotze, M. Weiler, S. Geprägs, H. Huebl, S. T. B. Goennenwein, and G. Woltersdorf, "Spin pumping in YIG/Pt bilayers as a function of layer thickness", Physical Review B **92**, 1–6 (2015) (cit. on p. 47).

[78]M. Weiler, A. Aqeel, M. Mostovoy, A. Leonov, S. Geprägs, R. Gross, H. Huebl, T. T. M. Palstra, and S. T. B. Goennenwein, "Helimagnon resonances in an intrinsic chiral magnonic crystal", arXiv, 1705.02874 (2017) (cit. on p. 49).

[79]E. G. Spencer, R. C. Lecraw, and A. M. Clogston, "Low-temperature line-width maximum in yttrium iron garnet", Physical Review Letters **3**, 32–33 (1959) (cit. on pp. 51, 57).

[80]M. Sparks and C. Kittel, "Ferromagnetic relaxation mechanism for M_z in yttrium iron garnet", Physical Review Letters **4**, 232–234 (1960) (cit. on pp. 51, 57).

[81]K. P. Belov, L. A. Malevskaya, and V. I. Sokoldv, "Resonance and magnetic properties of yttrium iron garnet at low temperatures", Soviet Physics JETP **12**, 1074–1077 (1961) (cit. on pp. 51, 59, 64, 69).

[82]M. Haidar, M. Ranjbar, M. Balinsky, R. K. Dumas, S. Khartsev, and J. Åkerman, "Thickness- and temperature-dependent magnetodynamic properties of yttrium iron garnet thin films", Journal of Applied Physics **117**, 17D119 (2015) (cit. on pp. 52, 69).

[83]C. L. Jermain, S. V. Aradhya, N. D. Reynolds, R. A. Buhrman, J. T. Brangham, M. R. Page, P. C. Hammel, F. Y. Yang, and D. C. Ralph, "Increased low-temperature damping in yttrium iron garnet thin films", Physical Review B **95**, 174411 (2017) (cit. on pp. 52, 69).

[84]H. Maier-Flaig, *Temperature dependent damping of yttrium iron garnet spheres – Measurement data and analysis programs*, Open Science Framework e-publication, doi:10.17605/OSF.IO/7URPT, 2016 (cit. on p. 52).

[85]P. Röschmann and H. Dötsch, "Properties of magnetostatic modes in ferrimagnetic spheroids", physica status solidi (b) **82**, 11–57 (1977) (cit. on p. 54).

[86]L. R. Walker, "Magnetostatic modes in ferromagnetic resonance", Physical Review **105**, 390–399 (1957) (cit. on p. 54).

[87]P. C. Fletcher and R. O. Bell, "Ferrimagnetic resonance modes in spheres", Journal of Applied Physics **30**, 687–698 (1959) (cit. on p. 55).

[88]C. Kittel, "On the gyromagnetic ratio and spectroscopic splitting factor of ferromagnetic substances", Physical Review **76**, 743–748 (1949) (cit. on p. 55).

[89]P. Bruno, "Tight-binding approach to the orbital magnetic moment and magnetocrystalline anisotropy of transition-metal monolayers", Physical Review B **39**, 865–868 (1989) (cit. on p. 55).

[90] J. Nemarich, "Contribution of the two-magnon process to magnetostatic-mode relaxation", Physical Review **136**, A1657–A1664 (1964) (cit. on pp. 55, 57, 68).

[91] J. F. Dillon, "Ferrimagnetic resonance in yttrium iron garnet at liquid helium temperatures", Physical Review **111**, 1476–1478 (1958) (cit. on p. 57).

[92] T. Kasuya and R. C. LeCraw, "Relaxation mechanism in ferromagnetic resonance", Physical Review Letters **67**, 223–225 (1961) (cit. on pp. 57, 68, 71, 86).

[93] E. G. Spencer, R. C. Lecraw, and J. Linares, "Low-temperature ferromagnetic relaxation in yttrium iron garnet", Physical Review **123**, 1937–1938 (1961) (cit. on pp. 57, 69).

[94] M. Sparks, *Ferromagnetic-relaxation theory*, edited by W. A. Nierenberg (McGraw-Hill, 1964) (cit. on pp. 57–60, 69, 70, 144).

[95] B. H. Clarke, K. Tweedale, and R. W. Teale, "Rare-earth ion relaxation time and G tensor in rare-earth-doped yttrium iron garnet. I. Ytterbium", Physical Review **139**, A1933–A1943 (1965) (cit. on pp. 57, 59, 71, 72).

[96] B. H. Clarke, "Rare-earth ion relaxation time and G tensor in rare-earth-doped yttrium iron garnet. II. Neodymium", Physical Review **139**, A1944–A1948 (1965) (cit. on pp. 57, 70, 72).

[97] M. Sparks, "Effect of impurities on the microwave properties of yttrium iron garnet", Journal of Applied Physics **38**, 1031 (1967) (cit. on p. 57).

[98] J. Barker and G. E. W. Bauer, "Thermal spin dynamics of yttrium iron garnet", Physical Review Letters **117**, 217201 (2016) (cit. on p. 57).

[99] R. Orbach, "On the theory of spin-lattice relaxation in paramagnetic salts", Proceedings of the Physical Society **77**, 821–826 (1961) (cit. on p. 59).

[100] B. H. Clarke, "Ferrimagnetic resonance linewidth in rare-earth-doped YIG at low temperatures", Journal of Applied Physics **36**, 1211–1212 (1965) (cit. on p. 59).

[101] I. H. Solt, "Temperature dependence of YIG magnetization", Journal of Applied Physics **33**, 1189 (1962) (cit. on pp. 62, 63).

[102] W. Sucksmith, "The measurement of magnetic saturation intensities at different temperatures", Proceedings of the Royal Society A: Mathematical, Physical and Engineering Sciences **170**, 551–560 (1939) (cit. on p. 63).

[103]E. E. Anderson, "Molecular field model and the magnetization of YIG", Physical Review **134**, A1581–A1585 (1964) (cit. on pp. 63, 65).

[104]M. A. Gilleo and S. Geller, "Magnetic and crystallographic properties of substituted yttrium-iron garnet, $3Y_2O_3{\cdot}xM_2O_3{\cdot}(5-x)Fe_2O_3$", Physical Review **110**, 73–78 (1958) (cit. on pp. 63, 65, 128).

[105]G. R. Harrison and L. R. Hodges, "Temperature stable microwave hybrid garnets", Journal of Applied Physics **33**, 1375–1376 (1962) (cit. on pp. 63, 65).

[106]H. Pascard, "Relation between ionic structure and magnetic properties in spinels and garnets with large non magnetic ions", Journal of Magnetism and Magnetic Materials **15-18**, 1313–1314 (1980) (cit. on pp. 63, 65).

[107]P. Hansen, P. Röschmann, and W. Tolksdorf, "Saturation magnetization of gallium-substituted yttrium iron garnet", Journal of Applied Physics **45**, 2728–2732 (1974) (cit. on p. 63).

[108]R. L. White, "Use of magnetostatic modes as a research tool", Journal of Applied Physics **31**, S86–S94 (1960) (cit. on p. 63).

[109]P. Röschmann and W. Tolksdorf, "Epitaxial growth and annealing control of FMR properties of thick homogeneous Ga substituted yttrium iron garnet films", Materials Research Bulletin **18**, 449–459 (1983) (cit. on p. 68).

[110]Y. Sun, Y.-Y. Song, H. Chang, M. Kabatek, M. Jantz, W. Schneider, M. Wu, H. Schultheiss, and A. Hoffmann, "Growth and ferromagnetic resonance properties of nanometer-thick yttrium iron garnet films", Applied Physics Letters **101**, 152405 (2012) (cit. on p. 69).

[111]J. F. Dillon and J. W. Nielsen, "Effects of rare earth impurities on ferrimagnetic resonance in yttrium iron garnet", Physical Review Letters **3**, 30–31 (1959) (cit. on pp. 69, 72).

[112]S. A. Manuilov, S. I. Khartsev, and A. M. Grishin, "Pulsed laser deposited y3fe5o12 films: nature of magnetic anisotropy i", Journal of Applied Physics **106**, 123917 (2009) (cit. on p. 74).

[113]S. A. Manuilov and A. M. Grishin, "Pulsed laser deposited $Y_3Fe_5O_12$ films: Nature of magnetic anisotropy II", Journal of Applied Physics **108**, 013902 (2010) (cit. on p. 74).

[114]H. Maier-Flaig, *GdIG temperature dependent coupling - 2D fits of complex S_{11} parameter*, Open Science Framework e-publication, doi:10.17605/OSF.IO/D34DK, 2017 (cit. on pp. 74, 118).

[115]P. Landeros, R. E. Arias, and D. L. Mills, "Two magnon scattering in ultrathin ferromagnets: the case where the magnetization is out of plane", Physical Review B **77**, 214405 (2008) (cit. on p. 74).

[116]K. Zakeri, J. Lindner, I. Barsukov, R. Meckenstock, M. Farle, U. Von Hörsten, H. Wende, W. Keune, J. Rocker, S. S. Kalarickal, K. Lenz, W. Kuch, K. Baberschke, and Z. Frait, "Spin dynamics in ferromagnets: Gilbert damping and two-magnon scattering", Physical Review B **76**, 1–8 (2007) (cit. on p. 74).

[117]A. M. Clogston, "Inhomogeneous broadening of magnetic resonance lines", Journal of Applied Physics **29**, 334–336 (1958) (cit. on p. 76).

[118]S. Geschwind and A. M. Clogston, "Narrowing effect of dipole forces on inhomogeneously broadened lines", Physical Review **108**, 49–53 (1957) (cit. on pp. 76, 82).

[119]G. P. Rodrigue, H. Meyer, and R. V. Jones, "Resonance measurements in magnetic garnets", Journal of Applied Physics **31**, S376 (1960) (cit. on pp. 76, 78).

[120]R. K. Wangsness, "Ferrimagnetic resonance and some related effects", American Journal of Physics **24**, 60 (1956) (cit. on p. 78).

[121]R. Wangsness, "Sublattice effects in magnetic resonance", Physical Review **91**, 1085–1091 (1953) (cit. on p. 78).

[122]S. Geprägs, A. Kehlberger, F. D. Coletta, Z. Qiu, E.-J. Guo, T. Schulz, C. Mix, S. Meyer, A. Kamra, M. Althammer, H. Huebl, G. Jakob, Y. Ohnuma, H. Adachi, J. Barker, S. Maekawa, G. E. W. Bauer, E. Saitoh, R. Gross, S. T. B. Goennenwein, and M. Kläui, "Origin of the spin Seebeck effect in compensated ferrimagnets", Nature Communications **7**, 10452 (2016) (cit. on pp. 79, 115, 116).

[123]R. Urban, G. Woltersdorf, and B. Heinrich, "Gilbert damping in single and multilayer ultrathin films: role of interfaces in nonlocal spin dynamics.", Physical Review Letters **87**, 217204 (2001) (cit. on p. 91).

[124]I. Neudecker, G. Woltersdorf, B. Heinrich, T. Okuno, G. Gubbiotti, and C. Back, "Comparison of frequency, field, and time domain ferromagnetic resonance methods", Journal of Magnetism and Magnetic Materials **307**, 148–156 (2006) (cit. on p. 91).

[125]M. Bailleul, D. Olligs, and C. Fermon, "Micromagnetic phase transitions and spin wave excitations in a ferromagnetic stripe.", Physical review letters **91**, 137204 (2003) (cit. on p. 91).

[126]G. Counil, J. V. Kim, K. Shigeto, Y. Otani, T. Devolder, P. Crozat, H. Hurdequint, and C. Chappert, "Inductive measurement of the high frequency permeability of a permalloy thin film", Journal of Magnetism and Magnetic Materials **272-276**, 290–292 (2004) (cit. on p. 91).

[127]J. H. E. Griffiths, "Anomalous high-frequency resistance of ferromagnetic metals", Nature **158**, 670–671 (1946) (cit. on p. 91).

[128]B. Bleaney, "Jubilees of radio-frequency spectroscopy", Notes and Records of the Royal Society **51**, 317–326 (1997) (cit. on p. 91).

[129]S. Watanabe, "Circularly polarized microwaves for magnetic resonance experiments", Master's thesis (Technische Universität München, Aug. 2015) (cit. on p. 91).

[130]C. Braggio, G. Carugno, M. Guarise, A. Ortolan, and G. Ruoso, "Optical manipulation of a magnon-photon hybrid system", Physical Review Letters **118**, 107205 (2017) (cit. on p. 91).

[131]R. Barbieri, C. Braggio, G. Carugno, C. Gallo, A. Lombardi, A. Ortolan, R. Pengo, G. Ruoso, and C. Speake, "Searching for galactic axions through magnetized media: The QUAX proposal", Physics of the Dark Universe **15**, 135–141 (2017) (cit. on pp. 91, 92).

[132]I. Diniz, S. Portolan, R. Ferreira, J. M. Gérard, P. Bertet, and A. Auffèves, "Strongly coupling a cavity to inhomogeneous ensembles of emitters: potential for long-lived solid-state quantum memories", Physical Review A **84**, 063810 (2011) (cit. on p. 92).

[133]H. Paik, D. I. Schuster, L. S. Bishop, G. Kirchmair, G. Catelani, A. P. Sears, B. R. Johnson, M. J. Reagor, L. Frunzio, L. I. Glazman, S. M. Girvin, M. H. Devoret, and R. J. Schoelkopf, "Observation of high coherence in josephson junction qubits measured in a three-dimensional circuit QED architecture", Physical Review Letters **107**, 240501 (2011) (cit. on p. 92).

[134]S. Putz, D. O. Krimer, R. Amsüss, A. Valookaran, T. Nöbauer, J. Schmiedmayer, S. Rotter, and J. Majer, "Protecting a spin ensemble against decoherence in the strong-coupling regime of cavity QED", Nature Physics **10**, 720–724 (2014) (cit. on p. 92).

[135]D. I. Schuster, A. P. Sears, E. Ginossar, L. DiCarlo, L. Frunzio, J. J. L. Morton, H. Wu, G. A. D. Briggs, B. B. Buckley, D. D. Awschalom, and R. J. Schoelkopf, "High-cooperativity coupling of electron-spin ensembles to superconducting cavities", Physical Review Letters **105**, 140501 (2010) (cit. on pp. 92, 111, 113).

[136]Y. Kubo, F. R. Ong, P. Bertet, D. Vion, V. Jacques, D. Zheng, A. Dréau, J.-F. Roch, A. Auffeves, F. Jelezko, J. Wrachtrup, M. F. Barthe, P. Bergonzo, and D. Esteve, "Strong coupling of a spin ensemble to a superconducting resonator", Physical Review Letters **105**, 140502 (2010) (cit. on p. 92).

[137]A. Tkalčec, S. Probst, D. Rieger, H. Rotzinger, S. Wünsch, N. Kukharchyk, A. D. Wieck, M. Siegel, A. V. Ustinov, and P. Bushev, "Strong coupling of an Er^{3+}-doped $YAlO_3$ crystal to a superconducting resonator", Physical Review B **90**, 075112 (2014) (cit. on p. 92).

[138]C. W. Zollitsch, K. Mueller, D. P. Franke, S. T. B. Goennenwein, M. S. Brandt, R. Gross, and H. Huebl, "High cooperativity coupling between a phosphorus donor spin ensemble and a superconducting microwave resonator", Applied Physics Letters **107**, 142105 (2015) (cit. on pp. 92, 111, 113).

[139]R. Amsüss, C. Koller, T. Nöbauer, S. Putz, S. Rotter, K. Sandner, S. Schneider, M. Schramböck, G. Steinhauser, H. Ritsch, J. Schmiedmayer, and J. Majer, "Cavity QED with magnetically coupled collective spin states", Physical Review Letters **107**, 1–5 (2011) (cit. on p. 92).

[140]Ö. O. Soykal and M. E. Flatté, "Strong field interactions between a nanomagnet and a photonic cavity", Physical Review Letters **104**, 077202 (2010) (cit. on pp. 92, 102).

[141]H. Huebl, C. W. Zollitsch, J. Lotze, F. Hocke, M. Greifenstein, A. Marx, R. Gross, and S. T. B. Goennenwein, "High cooperativity in coupled microwave resonator ferrimagnetic insulator hybrids", Physical Review Letters **111**, 127003 (2013) (cit. on pp. 92, 102, 111, 113).

[142]N. Kostylev, M. Goryachev, and M. E. Tobar, "Superstrong coupling of a microwave cavity to yttrium iron garnet magnons", Applied Physics Letters **108**, 062402 (2016) (cit. on pp. 92, 119).

[143]B. M. Yao, Y. S. Gui, Y. Xiao, H. Guo, X. S. Chen, W. Lu, C. L. Chien, and C.-M. Hu, "Theory and experiment on cavity magnon-polariton in the one-dimensional configuration", Physical Review B **92**, 184407 (2015) (cit. on pp. 92, 102).

[144]G. R. Eaton, S. S. Eaton, D. P. Barr, and R. T. Weber, *Quantitative EPR* (Springer Vienna, 2010) (cit. on p. 96).

[145]Y. Cao, P. Yan, H. Huebl, S. T. B. Goennenwein, and G. E. W. Bauer, "Exchange magnon-polaritons in microwave cavities", Physical Review B **91**, 094423 (2015) (cit. on pp. 102, 105, 107, 114, 124, 132, 134, 140).

[146]P. F. Herskind, A. Dantan, J. P. Marler, M. Albert, and M. Drewsen, "Realization of collective strong coupling with ion coulomb crystals in an optical cavity", Nature Physics **5**, 494–498 (2009) (cit. on pp. 102, 106, 110–112, 132, 141).

[147]W. Nolting, *Theoretical physics 1* (Springer International Publishing, 2016) (cit. on p. 102).

[148]B. Heinrich, Y. Tserkovnyak, G. Woltersdorf, A. Brataas, R. Urban, and G. E. W. Bauer, "Dynamic exchange coupling in magnetic bilayers.", Physical Review Letters **90**, 187601 (2003) (cit. on p. 105).

[149]O. Mosendz, J. E. Pearson, F. Y. Fradin, G. E. W. Bauer, S. D. Bader, and A. Hoffmann, "Quantifying spin Hall angles from spin pumping: experiments and theory", Physical Review Letters **104**, 046601 (2010) (cit. on pp. 105, 123, 125).

[150]M. Tavis and F. W. Cummings, "Exact solution for an *N*-molecule–radiation-field hamiltonian", Physical Review **170**, 379–384 (1968) (cit. on pp. 105, 114).

[151]J. M. Fink, R. Bianchetti, M. Baur, M. Göppl, L. Steffen, S. Filipp, P. J. Leek, A. Blais, and A. Wallraff, "Dressed collective qubit states and the tavis-cummings model in circuit QED", Physical Review Letters **103**, 083601 (2009) (cit. on p. 105).

[152]D. F. Walls and G. J. Milburn, *Quantum optics* (Springer, 2008) Chap. 11 (cit. on p. 105).

[153]E. Abe, H. Wu, A. Ardavan, and J. J. L. Morton, "Electron spin ensemble strongly coupled to a three-dimensional microwave cavity", Applied Physics Letters **98**, 251108 (2011) (cit. on pp. 105, 111, 113, 119, 131).

[154]J. Lotze, "Spin pumping in ferrimagnet / normal metal bilayers", PhD thesis (Technische Universität München, 2015), pp. 1–134 (cit. on pp. 105, 124–127, 140).

[155]P. J. Petersan and S. M. Anlage, "Measurement of resonant frequency and quality factor of microwave resonators: comparison of methods", Journal of Applied Physics **84**, 3392–3402 (1998) (cit. on pp. 109, 129).

[156]B. A. Calhoun, W. V. Smith, and J. Overmeyer, "Ferrimagnetic resonance in gadolinium iron garnet", Journal of Applied Physics **29**, 427–428 (1958) (cit. on pp. 118, 119).

[157]R. Iguchi, K. Sato, D. Hirobe, S. Daimon, and E. Saitoh, "Effect of spin Hall magnetoresistance on spin pumping measurements in insulating magnet/metal systems", Applied Physics Express **7**, 013003 (2014) (cit. on pp. 123, 134).

[158]J. E. Hirsch, "Spin Hall Effect", Physical Review Letters **83**, 1834–1837 (1999) (cit. on p. 125).

[159]H. Jiao and G. E. W. Bauer, "Spin backflow and ac voltage generation by spin pumping and the inverse spin hall effect", Physical Review Letters **110**, 217602 (2013) (cit. on p. 125).

[160]S. Geprägs, S. Meyer, S. Altmannshofer, M. Opel, F. Wilhelm, A. Rogalev, R. Gross, and S. T. B. Goennenwein, "Investigation of induced Pt magnetic polarization in Pt/$Y_3Fe_5O_12$ bilayers", Applied Physics Letters **101**, 262407 (2012) (cit. on p. 126).

[161]M. B. Jungfleisch, V. Lauer, R. Neb, a. V. Chumak, and B. Hillebrands, "Improvement of the yttrium iron garnet/platinum interface for spin pumping-based applications", Applied Physics Letters **103**, 2011–2015 (2013) (cit. on p. 126).

[162]M. Althammer, S. Meyer, and H. Nakayama, "Quantitative study of the spin Hall magnetoresistance in ferromagnetic insulator/normal metal hybrids", Physical Review B **87** (2013) 10.1103/PhysRevB.87.224401 (cit. on p. 128).

[163]I. Chiorescu, N. Groll, S. Bertaina, T. Mori, and S. Miyashita, "Magnetic strong coupling in a spin-photon system and transition to classical regime", Physical Review B **82**, 024413 (2010) (cit. on p. 128).

[164]J. F. Dillon, "Ferrimagnetic resonance in yttrium iron garnet", Physical Review **105**, 759–760 (1957) (cit. on pp. 131, 132, 138).

[165] S. Klingler, a. V. Chumak, T. Mewes, B. Khodadadi, C. Mewes, C. Dubs, O. Surzhenko, B. Hillebrands, and A. Conca, "Measurements of the exchange stiffness of YIG films using broadband ferromagnetic resonance techniques", Journal of Physics D: Applied Physics **48**, 015001 (2015) (cit. on pp. 131, 132).

[166] C. Kittel, *Introduction to solid state physics* (John Wiley & Sons, 1995) (cit. on p. 131).

[167] B. Hoekstra, R. P. van Stapele, and J. M. Robertson, "Spin-wave resonance spectra of inhomogeneous bubble garnet films", Journal of Applied Physics **48**, 382 (1977) (cit. on p. 134).

[168] A. Tucciarone and P. De Gasperis, "Electrical properties of iron garnet films", Thin Solid Films **114**, 109–134 (1984) (cit. on p. 134).

[169] Y. Kajiwara, K. Harii, S. Takahashi, J. Ohe, K. Uchida, M. Mizuguchi, H. Umezawa, H. Kawai, K. Ando, K. Takanashi, S. Maekawa, and E. Saitoh, "Transmission of electrical signals by spin-wave interconversion in a magnetic insulator.", Nature **464**, 262–266 (2010) (cit. on p. 139).

[170] A. J. Princep, R. A. Ewings, S. Ward, S. Tóth, C. Dubs, D. Prabhakaran, and A. T. Boothroyd, "The final chapter in the saga of YIG", arXiv:1705.06594 (2017) (cit. on p. 144).

[171] T. Seifert, S. Jaiswal, U. Martens, J. Hannegan, L. Braun, P. Maldonado, F. Freimuth, A. Kronenberg, J. Henrizi, I. Radu, E. Beaurepaire, Y. Mokrousov, P. M. Oppeneer, M. Jourdan, G. Jakob, D. Turchinovich, L. M. Hayden, M. Wolf, M. Münzenberg, M. Kläui, and T. Kampfrath, "Efficient metallic spintronic emitters of ultrabroadband terahertz radiation", Nature Photonics **10**, 483–488 (2016) (cit. on p. 144).

[172] K. Ganzhorn, T. Wimmer, J. Cramer, S. Geprägs, R. Gross, M. Kläui, and S. T. B. Goennenwein, "Temperature dependence of the non-local spin Seebeck effect in YIG/Pt nanostructures", 2–5 (2017) (cit. on p. 144).

[173] L. Bai, M. Harder, P. Hyde, Z. Zhang, C.-M. Hu, Y. P. Chen, and J. Q. Xiao, "Cavity mediated manipulation of distant spin currents using a cavity-magnon-polariton", Physical Review Letters **118**, 217201 (2017) (cit. on p. 145).

[174] K. Ganzhorn, J. Barker, R. Schlitz, B. A. Piot, K. Ollefs, F. Guillou, F. Wilhelm, A. Rogalev, M. Opel, M. Althammer, S. Geprägs, H. Huebl, R. Gross, G. E. W. Bauer, and S. T. B. Goennenwein, "Spin Hall magnetoresistance in a canted ferrimagnet", Physical Review B **94**, 094401 (2016) (cit. on p. 145).

[175] M. Newville, T. Stensitzki, D. B. Allen, and A. Ingargiola, "Lmfit: non-linear least-square minimization and curve-fitting for python", (2014) 10.5281/ZENODO.11813 (cit. on p. III).

ACKNOWLEDGMENTS

"I think, if you're a physicist, the thing you have to enjoy is [...] being stuck. Because essentially you're always stuck, right? If you can do it, then you've done it and it's gone past and now you're at the next problem and [...] you're stuck again."

– Prof. Jonathan Home

Um, wie es in der Wissenschaft nötig ist, Schritt für Schritt weiter zu kommen und Probleme zu lösen ist es nicht immer genug (oder klug) nur alleine zu grübeln. In diesem letzten Kapitel möchte ich all den Personen danken die mir bei den wissenschaftlichen Problemen aber auch bei den Herausforderungen des Lebens geholfen haben, – denn zu guter Letzt ist es das Miteinander was die Arbeit leichter und das Leben lebenswert macht.

Im Speziellen möchte ich zuerst *Sebastian Gönnenwein* und *Rudolf Gross* erwähnen, die mir die Promotion am WMI ermöglicht haben: Meinem Doktorvater *Sebastian*, gebührt großer Dank für die vielen Stunden, die er mit mir in wissenschaftlichen Diskussionen und mit dem Korrigieren meiner Manuskripte, der Doktorarbeit, von Postern und Vorträgen verbracht hat. In der Forschung hat er mich immer wieder auf die richtige Spur gestoßen und mir dennoch gleichzeitig bei der Auswahl der Themen und der wissenschaftlichen Vorgehensweise sehr große Freiheiten gelassen: Eine, wie ich finde, gute Balance. *Prof. Groß* ermöglicht dieses freie Arbeiten am Institut durch seine Leitung und durch unzähligen Stunden, die er in Anträge und dergleichen steckt erst. Mit seinem breiten Wissen und seiner langjährigen Erfahrung in der Festkörperphysik hat er in meinen Manuskripten immer "natürlich doch noch etwas gefunden" und hat es nebenbei geschafft, mir die größeren Zusammenhänge in der Physik näher

zu bringen. Gemeinsam Sebastian Gönnenwein muss auch gleich *Hans Hübl* genannt werden. Nicht nur, weil die Beiden zu Beginn meiner Doktorarbeit immer als gemischtes Doppel aufgetreten sind, sondern weil ich in Hans doch immer meinen zweiten Betreuer gesehen habe. Mit vielen hilfreichen Diskussionen über Physik und Experiment hat er einen großen Beitrag am Gelingen der Arbeit.

Schon der Weg bis zur Promotion war nur durch den großartigen Rückhalt in meiner Familie möglich. Von Herzen danke ich meinen Eltern dafür wie sie mich stets im Leben und durch das Studium begleitet und unterstützt haben. Gleichzeitig haben mich meine Brüder *Florian und Sebastian* auf dem Boden gehalten. Obwohl (oder gerade) weil wir drei alle unsere eigene Art haben ist es immer schön und wertvoll ihre Meinung, ihre Geschichten und ihren Rat zu hören.

Zudem möchte ich auch meinen Kollegen und Freunden danken, insbesondere (aber nicht ausschließlich):

- *Mathias Weiler*, für sein großes Wissen und seine kritischen Kommentare mit denen er zum experimentellen Aufbau und zu den Publikationen maßgeblich beigetragen hat.

- *Stephan Geprägs*, dem Großmeister der Dünnfilmdeposition und der Festkörperphysikübung. Whatcha doing Steve?

- den Post-Docs mit denen ich zwar nicht gemeinsam an einem speziellen Projekt gearbeitet habe (*Matthias Althammer, Matthias Opel, Nynke Vlietstra*) aber die doch immer wieder mit Diskussionen, Büchern und Geräten geholfen haben.

- den Bachelor und Masterstudenten mit denen ich gearbeitet habe (*Sho, Felix, Philipp, Lukas und Kathrin*). Mir hat's Spaß gemacht, euch hoffentlich auch.

- meiner "ganz netten" Doktoranden-Kollegin *Kathrin Ganzhorn*. Danke für die schönen vier Jahre zusammen im Büro, die unzähligen Diskussionen die oft einfach mit "Du Kathrin, wie ist denn das ..." begannen, deine Geduld wenn mal wieder "mimimi" laufen musste oder wenn die Wissenschaft (oder der Computer) mich erfolgreich zum Schimpfen aufgefordert hat und für die vielen Gelegenheiten gemeinsam zu lachen.

- *Stefan Weichselbaumer,* vom dem ich dank seiner großen Begeisterungsfähigkeit für alles Technische und die Natur viel lernen und wie nebenbei noch einige Berge besteigen konnte.

- *Edwar Xie,* der mir des Öfteren bei Finite-Elemente-Simulationen auf die Sprünge geholfen hat.

- *Stefan Klingler* mit seiner pragmatischen Art und dem richtigen Spruch für jede Situation, für die viele Diskussionen (nicht nur im AC meeting) und die unkomplizierte Zusammenarbeit im Labor.

- *Johannes Lotze,* der mich ins Walther-Meißner-Institut und die FMR-Aufbauten im Saga im Speziellen eingeführt hat.

- den anderen (Magnetiker-)Doktoranden *Sybille Meyer, Matthias Pernpeintner, Philip Schmidt, Michael Schreier, Daniel Schwienbacher und Christoph Zollitsch* für das gute Umfeld in das ich am WMI starten konnte und die Hilfe bei Kleinigkeiten in und ums Labor, auch wenn wir nie länger gemeinsamen an einem Projekt gearbeitet haben.

- *Edwin Menzel,* der mich mit seiner genauen Art beeindruckt hat und von dem ich über Mikrowellenequipment alles erfahren konnte.

- meinem Mitdoktorand, Kletterpartner und Freund *Michael Fischer*.

- *Michael Harder* with his friendly nature which is possibly best expressed by citing his answer when we (again) literally translated some German words into English and asked: “Michael, is that a word?” – “Yes, it can be.”. It was great having you here and working with you!

- *Akashdeep Kamra:* He is (theoretically) a very good wing man and (factually) a very good theorist. Thanks for explaining your understanding of physics and life so well.

- *Martin Brandt,* für das unkompliziert Aushelfen mit Messequipment und Messzeit am Walter-Schottky-Insitut.

- *dem technischen Personal des WMI,* insbesondere den Mitarbeitern der Werkstatt die mich immer wieder mit ihren Fähigkeiten erstaunt haben und oft unkompliziert halfen. Außerdem *Karen und Astrid*,

für das Entwickeln und Ätzen von unzähligen koplanaren Strukturen für Sho und mich.

- *all referees* who provided a careful evaluation and constructive criticism in their reports in time. This is much neglected, but you keep science sane and going.

- den Freunden aus der Studienzeit in Karlsruhe und insbesondere *Moritz Haarig* mit seiner freundlichen und klugen Art. Danke für die vielen kleinen und großen Abenteuer die wir seit Beginn des Studiums gemeinsam erlebt haben und die die Zeit so bereichert haben.

Thank you
Mario!
The kingdom
is saved!
Now try
a more
difficult
quest!

— Princess Peach